CAMILA DOMINGUES MENDONÇA VERBINNEN

Development of semiconductor-based photoelectrochemical sensing strategies for phenolic compounds in natural and supply water

São Carlos

2022

CAMILA DOMINGUES MENDONÇA VERBINNEN

Development of semiconductor-based photoelectrochemical sensing strategies for phenolic compounds in natural and supply water

Original Version

Ph.D. Thesis presented to the Graduate Program in Chemistry at the São Carlos Chemical Institute, University of São Paulo, Brazil and University of Antwerp, Belgium to obtain the dual degree: Doctor of Sciences (concentration area: Analytical and Inorganic Chemistry) and Doctor of Bioscience Engineering.

Supervisor: Prof. Dr. Sergio Antonio Spinola Machado
Advisor: Prof. Dr. Karolien De Wael

São Carlos / Antwerp
2022

Ficha Catalográfica elaborada pela Seção de Referência e Atendimento ao Usuário do SBI/IQSC

Verbinnen, Camila Domingues Mendonça
Development of semiconductor-based photoelectrochemical sensing strategies for phenolic compounds in natural and supply water / Camila Domingues Mendonça Verbinnen. — São Carlos, 2022.
148 f.

Tese (Doutorado em Química Analítica e Inorgânica) — Instituto de Química de São Carlos / Universidade de São Paulo, 2022.

Orientador: Prof. Dr. Sergio Antonio Spinola Machado
Coorientadora: Profa. Dra. Karolien De Wael

1. Eletroquímica. 2. Química Analítica. 3. Fotoeletroanalítica. 4. Compostos fenólicos. I. Título.

Wilneide do Carmo Marchi Maiorano - CRB: 3978/8

This thesis is dedicated to my dear and beloved father, Aroldo Guedes Mendonça.

(*In memoriam*)

ACKNOWLEDGMENTS

My first thanks is to the greatest Master of all. To the One who teaches, guides and illuminates the paths; to the One who supports and loves unconditionally. I am immensely grateful to God for allowing me to conclude this stage of my life.

My sincere thanks to Prof. Dr. Sergio Machado for his supervision during my entire period at the GMEME research group; for has given me the opportunity to develop this challenging PhD project and for has assisted me during its development.

I would like to thank Prof. Dr. Karolien de Wael for opening the doors of the A-Sense Lab and for her valuable supervision during the joint PhD, encouraging my professional growth and giving me tools to expand my knowledge.

Thanks to the University of São Paulo and the University of Antwerp for the opportunity of professional growth. I would also like to thank FAPESP for all the financial support during the doctorate and for having opened the door to new opportunities on my academic career (Grant #2016/06139-9 and #2018/13724-0).

Special thanks to my parents, Goretti and Aroldo (*in memoriam*), for always believing in my potential and for their endless love. They are my foundation and the main responsible for my education. To them I owe all my success!

My sincere thanks to my husband Raphael Verbinnen, for his companionship and unconditional support during all these years, being always my calm in the midst of the storm.

Thanks to the Domingues and Guedes family who always support me in every decision and cheer for my success.

I would also like to thank my friends and colleagues who contributed during the development of this thesis, especially to my dear friend Vanoushe for guiding me during my arrival at the A-Sense Lab, for our talks that made me grow professionally, and for all the fun moments.

Thanks to the GMEME group for all the shared moments, especially to Naiza, my colleague and long time friend, who even from far away was always present. I would also like to thank the colleagues from A-Sense Lab for having received me so well during my doctorate. I would like to thank the technicians and staff from IQSC (USP), from the department of bioscience engineering and from the doctoral school of the University of Antwerp for their support, and for their essential and impeccable work.

My sincere thanks to those who contributed directly and indirectly to the completion of this thesis!

RESUMO

Uma grande variedade de compostos orgânicos e inorgânicos têm sido frequentemente descartados no meio ambiente sem controle por indústrias e atividades agrícolas. Isto tem causado impactos significativos no desenvolvimento e na saúde dos organismos vivos, e na biodiversidade. Portanto, o desafio do monitoramento e/ou remediação desses contaminantes permanece. Esta tese apresenta o desenvolvimento de três estratégias de sensoriamento baseadas em sensores fotoeletroquímicos para o monitoramento de contaminantes fenólicos. Os conhecidos semicondutores TiO_2 e ZnO foram utilizados para a construção de novas configurações para análise nM de compostos fenólicos na água. O TiO_2 comercial foi previamente calcinado para aumentar o tamanho de seus poros. As configurações empregando fotossensores baseados em TiO_2 foram integradas em uma célula de fluxo fotoeletroquímico. O sistema em fluxo favoreceu uma maior sensibilidade do método através de sequências periódicas de lavagem do eletrodo, reduzindo significativamente o envenenamento do eletrodo. Primeiramente, foi desenvolvido um método simples baseado na imobilização do TiO_2 em eletrodos de grafite impressos em tela. Sob luz UV, o fotossensor desenvolvido apresentou um alto desempenho para a detecção de 4-aminofenol. Um segundo estudo foi desenvolvido através da impregnação de nanopartículas de ouro na estrutura de TiO_2. A incorporação de nanopartículas de ouro pode ampliar a região de absorção de luz de TiO_2 e melhorar sua atividade fotocatalítica para a detecção de hidroquinona sob luz visível. Em ambos os sistemas, a detecção foi possível devido à presença de espécies reativas de oxigênio na superfície do TiO_2 sobre a luz, que participam do processo de oxidação do analito. Ao aplicar um potencial redutor, a forma oxidada do analito é reduzida e é registrada uma resposta amperométrica mensurável proporcional à concentração inicial do analito. A terceira configuração proposta é um fotossensor baseado em ZnO para a quantificação de 4-nitrofenol sob luz UV-A. O ZnO nanoestruturado foi sintetizado eletroquimicamente sobre o substrato de vidro FTO, sem o uso de catalisadores ou camada semente. Um tratamento de recozimento pós-crescimento melhorou significativamente as propriedades físico-químicas dos nanobastões de ZnO. A modificação posterior dos nanobastões de ZnO com um fotossensibilizador (ácido perileno) aumentou a resposta de fotocorrente e a sensibilidade. Neste sistema, o mecanismo de detecção é baseado na diminuição da resposta de fotocorrente na presença de uma molécula coletora de elétrons, como o 4-nitrofenol. A diminuição da fotocorrente é proporcional ao aumento da concentração de 4-nitrofenol na solução. A aplicabilidade das configurações fotoeletroquímicas de sensoriamento baseadas em semicondutores foi verificada para análise de compostos fenólicos em amostras de água natural e de abastecimento. As abordagens robustas e sensíveis propostas foram projetadas para o monitoramento *in loco* de compostos fenólicos. Os resultados encorajadores confirmam o potencial desses fotossensores como ferramentas promissoras para fins de sensoriamento a nível de traços.

Palavras-chave: Sensores baseados em semicondutores. Estratégias de sensoriamento fotoeletroquímico. Dióxido de titânio. Análise de injeção de fluxo (FIA). Óxido de zinco. Fotossensibilizador. Compostos fenólicos.

ABSTRACT

A wide variety of organic and inorganic compounds have been frequently released into the environment without control by industries and agricultural activities. This has caused significant impact on the development and health of living organisms, and biodiversity. Therefore, the challenge of monitoring and/or remediation of these contaminants remains. This thesis presents the development of three sensing strategies based on photoelectrochemical sensors to monitor phenolic contaminants. The well-known semiconductors TiO_2 and ZnO were used for building novel setups for nM analysis of phenolic compounds in water. Commercial TiO_2 was previously calcined to enlarge its pore size. The setups employing TiO_2-based photosensors were integrated into a photoelectrochemical flow cell. The flow system favored higher sensitivity of the method by periodic wash sequences of the electrode, significantly reducing the electrode fouling. Firstly, a straightforward method was developed based on the immobilization of TiO_2 on screen printed graphite electrodes. Under UV light, the developed photosensor presented high performance for the detection of 4-aminophenol. A second study was developed by impregnating gold nanoparticles into TiO_2 structure. The incorporation of gold nanoparticles can broaden the light absorption region of TiO_2 and improve its photocatalytic activity for the detection of hydroquinone under visible light. In both systems, the detection was possible due to the presence of reactive oxygen species at the surface of TiO_2 upon light, which participate in the oxidation process of the analyte. By applying a reductive potential, the oxidized form of the analyte gets reduced and a measurable amperometric response proportional to the initial analyte concentration is recorded. The third proposed setup is a ZnO-based photosensor for the quantification of 4-nitrophenol under UV-A light. Nanostructured ZnO was electrochemically synthesized on FTO glass without the use of catalysts or seed layer. A post-growth annealing treatment significantly improved ZnO nanorods physicochemical properties. Subsequent modification of ZnO nanorods with a photosensitizer (perylene acid) increased the photocurrent response and the sensitivity. In this system, the detection mechanism is based on the decrease of the photocurrent response at the presence of an electron harvesting molecule, such as 4-nitrophenol. The decrease in photocurrent is proportional to the increase of 4-nitrophenol concentration in the solution. The applicability of the photoelectrochemical semiconductor-based sensing setups was verified to analyze phenolic compounds in natural and supply water samples. The proposed robust and sensitive approaches were designed for the on-site monitoring of phenolic compounds. The encouraging results confirm the potential of these photosensors as promising tools for trace-level sensing purposes.

Keywords: Semiconductor-based sensors. Photoelectrochemical sensing strategies. Titanium dioxide. Flow injection analysis (FIA). Zinc oxide. Photosensitizer. Phenolic compounds.

SAMENVATTING

Een grote variëteit aan organische en anorganische stoffen wordt vaak zonder controle uitgestoten in het milieu zowel door de industrie als door landbouwactiviteiten. Dit heeft aanzienlijke gevolgen voor de ontwikkeling en de gezondheid van levende organismen en voor de biodiversiteit. Daarom blijft het een uitdaging om deze verontreinigende stoffen te monitoren en/of te saneren. Dit proefschrift presenteert de ontwikkeling van drie detectiestrategieën gebaseerd op foto-elektrochemische sensoren om fenolische verontreinigingen te monitoren. De bekende halfgeleiders TiO_2 en ZnO werden gebruikt voor het bouwen van nieuwe opstellingen voor de nM analyse van fenolische stoffen in water. Commercieel TiO_2 werd vooraf gecalcineerd om de poriegrootte te vergroten. De opstellingen met TiO_2 gebaseerde fotosensoren werden geïntegreerd in een foto-elektrochemische doorstroomcel. Het stromingssysteem bevoordeelde een hogere gevoeligheid van de methode door periodieke wasbeurten van de elektrode, waardoor de elektrodevervuiling aanzienlijk werd verminderd. Eerst werd een eenvoudige methode ontwikkeld op basis van de immobilisatie van TiO_2 op gezeefdrukte grafietelektroden. Onder UV-licht vertoonde de ontwikkelde fotosensor een hoge prestatie voor de detectie van 4-aminophenol. Een tweede studie werd ontwikkeld door goudnanopartikels in de TiO_2-structuur te impregneren. De integratie van gouden nanodeeltjes kan het lichtabsorptiegebied van TiO_2 verbreden en de fotokatalytische activiteit verbeteren voor de detectie van hydrochinon onder zichtbaar licht. In beide systemen was de detectie mogelijk door de aanwezigheid van reactieve zuurstofdeeltjes aan het oppervlak van TiO_2 bij licht, die deelnemen aan het oxidatieproces van het analiet. Door aanleggen van een reductieve potentiaal wordt de geoxideerde vorm van het analiet gereduceerd en wordt een meetbare amperometrische respons geregistreerd die proportioneel is met de oorspronkelijke analietconcentratie. De derde voorgestelde opstelling is een op ZnO gebaseerde fotosensor voor de kwantificering van 4-nitrofenol onder UV-A licht. Nanogestructureerd ZnO werd elektrochemisch gesynthetiseerd op FTO glas zonder gebruik van katalysatoren. Een gloeibehandeling na de groei verbeterde de fysisch-chemische eigenschappen van ZnO nanorods aanzienlijk. De daaropvolgende modificatie van ZnO nanorods met een fotosensibilisator (peryleenzuur) verhoogde de fotostroomrespons en de gevoeligheid. In dit systeem is het detectiemechanisme gebaseerd op de afname van de fotostroomrespons bij aanwezigheid van een molecuul dat elektronen opvangt, zoals 4-nitrofenol. De afname van de fotostroom is proportioneel met de toename van de 4-nitrofenolconcentratie in de oplossing. De toepasbaarheid van de foto-elektrochemische halfgeleider-gebaseerde detectieopstellingen werd geverifieerd voor de analyse van fenolische verbindingen in natuurlijke- en kraanwater stalen. De voorgestelde robuuste en gevoelige benaderingen werden ontworpen voor de on-site monitoring van fenolische stoffen. De bemoedigende resultaten bevestigen het potentieel van deze fotosensoren als veelbelovende instrumenten voor detectie op sporenniveau.

Trefwoorden: Halfgeleider-gebaseerde sensoren. Foto-elektrochemische detectie strategieën. Titaniumdioxide. Stroominjectie analyse (FIA). Zinkoxide. Fotosensibilisator. Fenolverbindingen.

LIST OF FIGURES

Figure 1.1 - Core chemical structure of phenolic compounds. 18

Figure 1.2 - Example of phenol effluents produced by major industries. 18

Figure 1.3 – (a) DPVs of HRP/CRG24H/GC electrode in phosphate buffer acquired during the successive addition of p-chlorophenol (b) DPVs of HRP/CRG24H/GC electrode in phosphate buffer acquired during the successive addition of phenol. 21

Figure 1.4 – Energy diagram for an n-type semiconductor under the incidence of a light source, resulting in the e^- promotion from the valence band (VB) to the conduction band (CB). 23

Figure 1.5 - (a) Schematic illustration of semiconductor-based photocurrent generation: (I) the formation of charge carriers under illumination; (II) the trapping of a CB electron and the formation of cathodic photocurrent; (III) the trapping of a VB hole and the formation of anodic photocurrent. (b) Doped semiconductor. (c) S-S heterojunction. (d) S-C heterojunction. (e) S-M heterojunction. (f) MC heterojunction. 26

Figure 2.1 - Calibration curve for 0.0125-25 µM HQ at SPE|TiO_2 under UV illumination in 10 mM KH_2PO_4 containing 0.1 M KCl (pH 7.0), applied potential -0.14 V vs Ag pseudo reference electrode (n = 4). Flow rate: 1 mL/min. Inset: Linear curve 0.0125 – 2.5 µM HQ under UV illumination (black) and in the absence of a light source (red). 39

Figure 2.2 - Effect of working potential on the amperometric response of 2.5 µM HQ in 10 mM KH_2PO_4 containing 0.1 M KCl (pH 7.0) (n = 4). Flow rate: 1 mL/min. Inset: Changes in the background current upon applying different potentials. 41

Figure 2.3 - Effect of pH on the amperometric response of 2.5 µM HQ in 10 mM KH_2PO_4 containing 0.1 M KCl, applied potential -0.14 V vs Ag pseudo reference electrode (n = 4). Flow rate: 1 mL/min. 41

Figure 2.4 - Calibration curve for 4-AP at SPE|TiO_2 under UV illumination in 10 mM KH_2PO_4 containing 0.1 M KCl (pH 7.0), applied potential -0.14 V vs Ag pseudo reference electrode (n = 4). Flow rate: 1 mL/min. Inset: Calibration curve for lower 4-AP concentration range 0.0125 – 1.0 µM. 42

Figure 3.1 - (a) XRD pattern of AuNPs@TiO_2 sample, anatase, rutile and Au references, (b) Raman spectra of AuNPs@TiO_2 sample and TiO_2 anatase reference. The AuNPs@TiO_2 sample is 3.0 wt.% of AuNPs loaded on TiO_2. 51

Figure 3.2 - (a) SEM image of AuNPs@TiO_2; (b) EDX patterns of AuNPs@TiO_2; TEM images of (c) AuNPs and (d) AuNPs@TiO_2. 52

Figure 3.3 - (a) UV-Vis absorbance spectra of AuNPs, TiO_2 and AuNPs@TiO_2, (b) Tauc plot for the band gap energy determination of AuNPs@TiO_2 sample. 54

Figure 3.4 - Linear sweep voltammogram for AuNPs@TiO_2 electrode under chopped light illumination, in presence (red) and absence (black) of 1.0 μM HQ in 10 mM PBS containing 0.1 M KCl (pH 7.0), using a step potential of 0.5 mV, scan rate of 0.25 mVs^{-1} and potential range of 0.4 V to -0.2 V. 55

Figure 3.5 - Expected photocatalytic reactions on AuNPs@TiO_2 surface under visible light (λ = 532 nm, green laser) and the photocurrent generation mechanism. 56

Figure 3.6 - (A) Amperometric response for SPE|AuNPs@TiO_2 in the presence of HQ (a) 0.0125, (b) 0.025, (c) 0.05, (d) 0.15, (e) 0.25, (f) 0.5, (g) 1.0, (h) 2.5, (i) 5.0, (j) 10 and (k) 25 μM, in 10 mM PBS containing 0.1 M KCl (pH 7.0) and applied potential of -0.14 V vs Ag quasi-reference electrode (n = 3). (B) Corresponding calibration curve (inset: linear curve in the concentration range from 0.0125 to 1.0 μM at SPE|AuNPs@TiO_2 (black) and at SPE|TiO_2 (red) under green light illumination). 56

Figure 3.7 - Influence of the working potential on the photocurrent response of 0.15 μM HQ at SPE|AuNPs@TiO_2 in 10 mM PBS containing 0.1 M KCl (pH 7.0) (n = 3), using a flow rate of 1 mL/min. 59

Figure 3.8 - Influence of pH on the photocurrent response of 0.15 μM HQ at SPE|AuNPs@TiO_2 in 10 mM PBS containing 0.1 M KCl, using a working potential of -0.14 V vs Ag quasi-reference electrode (n = 3) and flow rate of 1 mL/min. 59

Figure 3.9 - Calibration plot for 4-AP in 10 mM PBS containing 0.1 M KCl (pH 7.0), using SPE|AuNPs@TiO_2 under green light illumination and applied potential of -0.14 V vs Ag quasi-reference electrode (n = 3). Inset: Linear curve in the concentration range from 0.0125 to 0.5 μM. 60

Figure 4.1 - XRD patterns of ZnO nanorods as grown and annealed at 200 ºC, 300 ºC, 350 ºC, 400 ºC and 500 ºC plotted in the range of 2θ (a) from 15º to 75º and (b) from 30º to 37º (normalized according to the crystallographic plane (100)). 67

Figure 4.2 - (a) Raman spectra of FTO substrate, ZnO as grown and annealed at 200 ºC, 300 ºC, 350 ºC, 400 ºC and 500 ºC; (b) prominent Raman peaks (low-E_2 and high-E_2) magnified (normalized according to the band at 295 cm^{-1}). 69

Figure 4.3 - SEM images of ZnO nanorods (a) as grown and (b) annealed at 350 ºC. SEM magnification: 50,000x. 70

Figure 4.4 - XPS spectra of ZnO as grown and annealed at 350 ºC, synthesized on FTO substrate. 71

Figure 4.5 - O 1s XPS spectra of (a) ZnO as grown, (b) ZnO annealed at 350 ºC (peak finding method: local maximum) and (c) percentual area of the groups -O-Zn, -O-deficient and -O-surface at the related temperatures. ... 72

Figure 4.6 - a) Linear sweep voltammograms and (b) chronoamperometric responses for ZnO nanorod films as grown and annealed at 200 ºC, 300 ºC, 350 ºC, 400 ºC and 500 ºC, applied potential of 0.2 V under chopped light illumination in 0.01 M PBS (pH 7.0). ... 73

Figure 4.7 - a) UV-Vis absorbance spectra of the bare FTO substrate; of ZnO as grown and annealed at 350 ºC, both electrodeposited on the FTO substrate. b) Tauc plot for the band gap energy determination of ZnO nanorod films as grown and annealed at 350 ºC. ... 74

Figure 5.1 - Molecular structure of PTCA. ... 79

Figure 5.2 - Graphical representation of the theoretical energy level diagram of PTCA, ZnO, FTO, and 4-NP. ... 79

Figure 5.3 - FTIR spectra for (a) $ZnO_{350\ ^{\circ}C}$|PTCA, (b) $ZnO_{350\ ^{\circ}C}$, and (c) PTCA. ... 85

Figure 5.4 - XPS spectrum of $ZnO_{350\ ^{\circ}C}$|PTCA. ... 86

Figure 5.5 - XPS O 1s spectra of (a) $ZnO_{350\ ^{\circ}C}$|PTCA and (b) percentage area relative to the -O-Zn, -O-deficient, and -O-surface groups for each film. ... 87

Figure 5.6 - XPS C 1s spectra of the films (a) ZnO, (b) $ZnO_{350\ ^{\circ}C}$, and (c) $ZnO_{350\ ^{\circ}C}$|PTCA. ... 87

Figure 5.7 - (a) Absorbance spectra of the $ZnO_{350\ ^{\circ}C}$|PTCA (🟥), $ZnO_{350\ ^{\circ}C}$ (⬛) and PTCA (🟦); (b) Kubelka-Munk graph for $ZnO_{350\ ^{\circ}C}$ and $ZnO_{350\ ^{\circ}C}$|PTCA. ... 89

Figure 5.8 - Photocurrent transients for FTO-ZnO350$_{^{\circ}C}$|PTCA in the absence (⬛) and presence (🟥) of 8 nM 4-NP in 10 mM PBS buffer (pH 7.0) under UV-A illumination. ... 89

Figure 5.9 - Proposed schematic representation for the amperometric detection of 4-NP using the FTO-$ZnO_{350\ ^{\circ}C}$|PTCA photosensor. ... 90

Figure 5.10 - Influence of the applied potential on the PEC response of the FTO-$ZnO_{350\ ^{\circ}C}$|PTCA in the presence of 8.0 nM 4-NP in 10 mM PBS buffer (pH 7.0) under UV-A illumination. ... 91

Figure 5.11 - Influence of pH on the PEC response of the FTO-$ZnO_{350\ ^{\circ}C}$|PTCA in the presence of 8.0 nM 4-NP, applied potential of 0.2 V (*vs* Ag/AgCl) under UV-A illumination. Inset: Graph relating pH and photocurrent densities with their respective SD. ... 92

Figure 5.12 - Influence of the supporting electrolyte (pH 7.0) on the PEC response of the FTO-$ZnO_{350\ ^{\circ}C}$|PTCA in the presence of 8.0 nM 4-NP, applied potential 0.2 V (*vs* Ag/AgCl) under UV-A illumination. Inset: supporting electrolyte *vs* photocurrent densities. ... 92

Figure 5.13 - (A) Amperometric response for the FTO-ZnO$_{350\ °C}$|PTCA in the absence (a) and presence of 4-NP in the concentration range from 0.1 to 15.0 nM (b – k). (B) Calibration and linear curve. 93

Figure 5.14 - (a) Calibration curves for FTO-ZnO (●), FTO-ZnO|PTCA (▲), FTO-ZnO$_{350\ °C}$ (▼) and FTO-ZnO$_{350\ °C}$|PTCA (■) photosensors, concentration range from 0.1 to 15.0 nM 4-NP. (b) Amperometric responses for the photosensors in the presence of 8.0 nM 4-NP. 94

Figure 5.15 - Stability study of the photocurrent response using the FTO-ZnO$_{350\ °C}$|PTCA photosensor for the detection of 8.0 nM 4-NP in 10 mM PBS buffer (pH 7.0) and applied potential of 0.2 V (*vs* Ag/AgCl). 95

Figure 5.16 - (a) Repeatability and (b) reproducibility study of the FTO-ZnO$_{350\ °C}$|PTCA photosensor for the detection of 8.0 nM 4-NP in 10 mM PBS buffer (pH 7.0) and applied potential of 0.2 V (*vs* Ag/AgCl) (n = 3). 96

Figure 5.17 - Amperometric response of FTO-ZnO$_{350\ °C}$|PTCA photosensor in the presence of 8.0 nM 4-NP and interfering molecules, in a ratio of (a) 1:1 for HQ, 3-NP, Ph, 3-AP, and BPA, and in a ratio of (b) 1:100 for Fe^{3+}, Mg^{2+}, Zn^{2+}, Pb^{2+}, and Cd^{2+} (n = 3). 97

Figure 5.18 - Calibration curves obtained for the detection of 4-NP in the concentration range from 0.5 to 15.0 nM in PBS buffer (pH 7.0), in natural, and tap water. 98

Figure 5.19 - (a) Chromatogram of 10.0 μM 4-NP prepared in acetonitrile (ACN) and (b) calibration curve for 4-NP in the concentration range from 5.0 to 50.0 nM. 99

Figure 5.20 - Linear regression plots of the detection values for 4-NP obtained by photoelectrochemical (PEC) and chromatographic (HPLC) techniques in (a) tap and (b) natural water samples. 100

LIST OF TABLES

Table 2.1 - Comparison of the limit of detection for 4-aminophenol using flow injection analysis. 43

Table 3.1 - Recovery results of HQ and 4-AP quantification in effluent sample 61

Table 4.1 - Effect of annealing treatment on the structural parameters of ZnO 68

Table 5.1 - Analytical performance of the previously reported PEC and electrochemical sensors for 4-NP detection 93

LIST OF ABREVIATIONS AND SYMBOLS

α	absorption coefficient
ACN	acetonitrile
AP	aminophenol
AuNPs	gold nanoparticles
β	half-height width of the plane
BPA	bisphenol A
BQ	benzoquinone
CAQI	chemical analysis center
DRS	diffuse reflectance spectroscopy
DMF	N,N-dimethylformamide
e^-	electrons
EDX	energy dispersive X-ray spectroscopy
E_g	band gap
FEG	field emission guns
FIA	flow injection analysis
FTO	fluorine doped tin oxide
$F(R)$	Kulbeka-Munk function
FWHM	full width at half-maximum
h^+	holes
h	Plank’s constant
HPLC	high performance liquid chromatography
HQ	hydroquinone
IQSC	São Carlos institute of chemistry
L	crystallite size
LED	light-emitting diode
LOD	limit of detection
LSV	linear sweep voltammetry
NP	nitrophenol
PEC	photoelectrochemical
PTCA	perylene tetracarboxylic acid
R	absolute reflectance
RSD	relative standard deviation
ROS	reactive oxygen species
SD	standard deviation
SEM	scanning electron microscopy
SPE	screen printed electrode
SPR	surface plasmon resonance
TEM	transmission electron microscopy
TiO_2	titanium dioxide
UV	ultraviolet
UV-vis	ultraviolet and visible spectroscopy
XPS	X-ray photoelectron spectroscopy
XRD	X-ray diffraction
ZnO	zinc oxide
v	frequency
λ	wavelength

SUMMARY

LIST OF FIGURES 5

LIST OF TABLES 9

LIST OF ABREVIATIONS AND SYMBOLS 10

CHAPTER 1 15

- **1.1 THESIS OVERVIEW** 15
- **1.2 INTRODUCTION** 17
  - **1.2.1 Phenolic compounds** 17
  - **1.2.2 Electrochemical methods for phenolic compounds detection** 19
  - **1.2.3 PEC sensors** 22
    - 1.2.3.1 PEC-based sensing strategies 24
  - **1.2.4 New prospects: PEC sensing for phenolic compounds** 29
- **1.3 LINK BETWEEN ARTICLES PRESENT IN THE BODY OF THE THESIS AND THE PhD PROJECT** 32
- **1.4 OBJECTIVES** 32

CHAPTER 2 35

Photoelectrochemical sensing of the 4-aminophenol by using a TiO_2-based amperometric sensor integrated to a FIA system *35*

- **2.1 INTRODUCTION** 36
- **2.2 EXPERIMENTAL** 37
  - **2.2.1 Materials** 37
  - **2.2.2 Apparatus** 37
  - **2.2.3 Electrode modification** 38
  - **2.2.4 Analytical procedure** 38
- **2.3 RESULTS AND DISCUSSIONS** 39
  - **2.3.1 Electrochemical behavior of HQ at SPE|TiO_2 under UV illumination** 39
  - **2.3.2 Effect of flow rate** 40

2.3.3 Effect of working potential and pH on the photocurrent of HQ 40

2.3.4 Photoelectrochemical response of the sensor for 4-AP 42

2.3.5 Real sample analysis 43

2.4 CONCLUSIONS 43

CHAPTER 3 45

Photoelectrochemical monitoring of the hydroquinone by using an AuNPs@TiO$_2$-based amperometric sensor integrated to a FIA system 45

3.1 INTRODUCTION 46

3.2 EXPERIMENTAL 48

3.2.1 Materials 48

3.2.2 Apparatus 48

3.2.3 Synthesis of AuNPS@TiO$_2$ and electrode modification 48

3.2.4 Characterization 49

3.2.5 Analytical procedure 50

3.3 RESULTS AND DISCUSSIONS 50

3.3.1 Morphological study 50

3.3.2 Photocatalytic performance of SPE|AuNPs@TiO$_2$ for HQ sensing 55

3.3.3 Flow rate optimization 58

3.3.4 Working potential and pH optimization 58

3.3.5 Applicability of SPE|AuNPs@TiO$_2$ modified electrode 60

3.3.6 Interference study for HQ 60

3.3.7 Real sample analysis 61

3.4 CONCLUSIONS 61

CHAPTER 4 63

Influence of annealing treatment on the properties of electrochemically synthesized ZnO nanorods 63

4.1 INTRODUCTION 64

4.2 EXPERIMENTAL 65

4.2.1 Materials 65

4.2.2 Apparatus 65

4.2.3 Synthesis of ZnO on FTO glass 66

4.2.4 Characterization 66

4.3 RESULTS AND DISCUSSIONS 67

4.3.1 Morphological characterization 67

4.3.2 Electrochemical characterization 72

4.3.3 Optical characterization 74

4.4 CONCLUSIONS 75

CHAPTER 5 77

Photoelectrochemical monitoring of the 4-nitrophenol by using the amperometric sensor of ZnO nanorods electrodeposited on FTO substrate 77

5.1 INTRODUCTION 78

5.2 EXPERIMENTAL 81

5.2.1 Materials 81

5.2.2 Apparatus 81

5.2.3 Synthesis of ZnO nanorods and sensitization by PTCA 82

5.2.4 Characterization 82

5.2.5 Analytical procedure 83

5.2.6 Statistical study 84

5.3 RESULTS AND DISCUSSIONS 84

5.3.1 Influence of PTCA concentration 84

5.3.2 FTIR analysis 85

5.3.3 XPS analysis 85

5.3.4 Band gap calculation 88

5.3.5 PEC analysis 89

5.3.5.1 Dependency on FTO-ZnO$_{350^{\circ}C}$|PTCA and applied potentials 89

5.3.5.2 Working potential 90

5.3.5.3 pH effect and supporting electrolyte 91

5.3.5.4 Amperometric detection of 4-NP using $ZnO_{350°C}$|PTCA under UV-A illumination 92

5.3.5.5 Stability study 95

5.3.5.6 Repeatability and reproducibility 95

5.3.5.7 Interfering study 96

5.3.5.8 Applicability of FTO-$ZnO_{350\,°C}$|PTCA 97

5.3.6 Chromatographic detection of 4-NP 98

5.3.7 Statistical study 99

5.4 CONCLUSIONS 100

CONCLUSIONS AND OUTLOOK 103

BIBLIOGRAPHY 106

APPENDIX A – Supplementary Information (Chapter 2) 132

APPENDIX B – Supplementary Information (Chapter 3) 137

APPENDIX C – Supplementary Information (Chapter 4) 142

APPENDIX D – Supplementary Information (Chapter 5) 144

ANNEX I 146

ANNEX II 147

SCIENTIFIC CONTRIBUTIONS DURING PhD 148

CHAPTER 1

1.1 THESIS OVERVIEW

The increasing and often uncontrolled disposal of phenolic compounds into the environment by industrial, agricultural, and domestic activities has become a public health problem. Being aware of the toxicity of these compounds and the various harmful side effects to humans, aquatic organisms, and the environment, the development of strategies for accurate, rapid, and effective monitoring of the quality of natural and supply waters becomes necessary. Currently, the most common techniques used by control agencies to monitor phenols in aquatic environments are expensive and time-consuming analysis. Therefore, the objective of this thesis is to present novel semiconductor-based photoelectrochemical (PEC) platforms for the amperometric detection in the nM range of phenolic compounds usually found in aquatic matrices. The proposed setups were developed with high sensitivity, accuracy, and reproducibility for the detection of phenols, based on costless and environmental friendly materials, commercial pristine (TiO_2 P25) or synthesized in laboratory (AuNPs and ZnO nanorods). The challenging part of this thesis is the development of robust and reliable PEC setups for in situ monitoring of this group of hazardous compounds.

The thesis consists of a collection of articles and is divided into five chapters. **Chapter 1** provides a general introduction to the PEC sensing technique based on semiconductor materials and a comprehensive review of the major strategies recently developed for the accurate monitoring of concerned pollutants. This chapter also lists the general objective of the thesis, as well as the specific objectives of each developed PEC strategy used in this thesis.

Chapter 2 discusses the development of a flow injection-based amperometric photosensor for the quantification of 4-aminophenol (4-AP) under UV-light by using graphite screen printed electrodes (SPE) modified with commercial TiO_2. The flow injection analysis (FIA) system was used to improve the sensitivity of the method by periodic wash sequences of the electrode surface, preventing its poisoning. The optimization of experimental and operational parameters related to the developed analytical sensing configuration is described in detail. The introduction of the PEC detection based on the generation of reactive oxygen species (ROS) is also addressed.

Chapter 3 presents the study of impregnating size-controlled gold nanoparticles (AuNPs) into the structure of commercial TiO_2 by photo-assisted synthesis for the quantification of hydroquinone (HQ) under visible light illumination and integrated into a FIA setup. The boosting of the PEC signal of TiO_2 and the enhancement of its light absorption ability ascribed to the surface plasmon resonance (SPR) effect and to the charge transfer property of AuNPs. As described in Chapter 2, in this chapter the detection of HQ is also based on the generation of ROS on the surface of the plasmonic sensor under visible light illumination.

Chapter 4 is devoted to the synthesis and characterization of well-aligned ZnO nanorods electrodeposited on fluorine-doped tin oxide (FTO) coated glass substrate and to the study of the post-growth annealing effect on their crystallinity. The strong influence of the post-growth annealing treatment on the physicochemical properties of the synthesized ZnO nanorods is dully presented through results obtained by morphological, optical, and electrochemical characterization techniques. ZnO nanorods with enhanced photocatalytic activity can be as a promising material for PEC sensing applications.

Chapter 5 focuses on the application of nano-sized ZnO, after surface annealing treatment, for the amperometric detection of 4-nitrophenol (4-NP) under UV-light in natural and supply water samples. After synthesis optimization and annealing study (Chapter 4), the ZnO nanorods were modified with the photosensitizer 3,4,9,10-tetracarboxylic perylene acid (PTCA) for further enhancement of their photocatalytic properties. Under optimized experimental and operational conditions, the $FTO\text{-}ZnO_{350\ °C}|PTCA$ photosensor was produced. To evaluate the electrochemical developed sensor, the performance was compared to chromatography (HPLC) for detection of 4-NP in real samples.

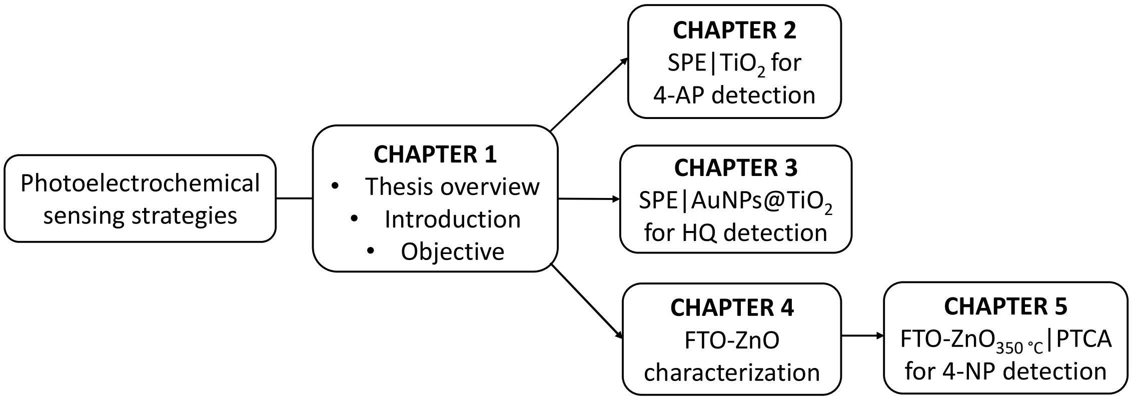

At last, the **Conclusions and outlook** chapter covers an overview of the remarkable points of the development of each proposed PEC sensing strategy for phenolic compounds discussed throughout chapters 2 to 5. Furthermore, the challenges regarding the future possibilities of designing such PEC sensing platforms for real monitoring applications are also discussed in this section.

The articles (Chapters 2 and 4) used to compose this thesis are of my authorship published in peer-reviewed journals, as shown in the Annex I and II. Chapters 4 and 5 are in the publishing process.

1.2 INTRODUCTION

1.2.1 Phenolic compounds

The pollution of water sources by industrial, agricultural, and domestic effluents has been discussed for years and the challenge of monitoring and/or remediation of organic and inorganic contaminants remains. A wide variety of contaminant compounds are frequently released without control into the environment and have been caused a significant impact on living organisms and biodiversity. The continued discharge of these contaminants without appropriate treatment into the environment can generate irreversible harmful effects to aquatic organisms and may pose a serious long-term risk to human health.[1] In addition, the conventional water and wastewater treatment methods used are not effective in completely removing these compounds.[2]

Among the organic contaminants commonly found in the environment are phenolic compounds, which are a class of compounds consisting of one or more benzene rings and hydroxyl groups (Fig. 1.1). Phenolic compounds are widely employed in industrial activities, such as in the production and processing stages of chemicals, due to their antioxidant, antibacterial, anti-inflammatory, and antimicrobial properties.[3] In a recent review on strategies for removing phenolic compounds from wastewater, Said *et al.* (2021) discussed the main industrial effluents containing phenol and their derivatives frequently detected in water (Fig. 1.2).[1] The major industries cited include petroleum refining[4], coal refining[5], pharmaceutical[6], petrochemical[7], and tannery[8] industries. Their presence in the environment originating from agricultural activities is due to the degradation of pesticides and insecticides and subsequent generation of phenolic sub-products, for instance, the generation of 4-nitrophenol (4-NP) from the hydrolysis reaction of the organophosphorus pesticides methyl-parathion and fenitrothion.[9, 10] Some pharmaceuticals and personal care products are manufactured using phenolic compounds, such as 4-aminophenol (4-AP) and hydroquinone (HQ).[11, 12]

Figure 1.1 - Core chemical structure of phenolic compounds.

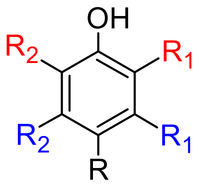

Source: Own authorship.

Figure 1.2 - Example of phenol effluents produced by major industries.

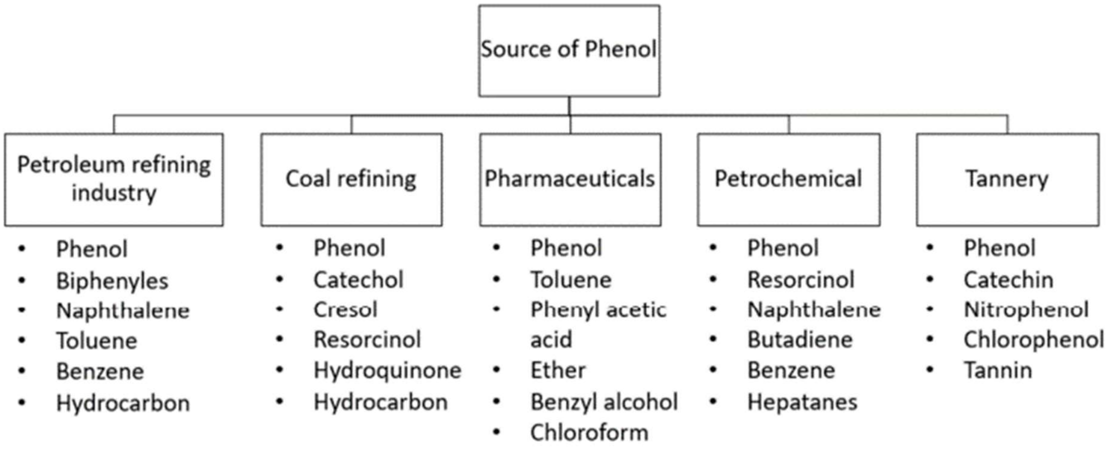

Source: Said *et al*., 2021.

Phenolic compounds are included in the list of priority pollutants designated by the European Union (EU) and by the United States Environmental Protection Agency (USEPA), due to their high toxicity and low degradability characteristics, posing a danger to aquatic life and human health even at small concentrations.[3] Moreover, they can also reach the drinking water source, through direct contamination or by dragging, washed from the ground or the air by rainwater, and generate a considerable risk for the population.[13] In this sense, the USEPA has defined the maximum permissible concentration of phenol and its derivatives as ranging from 60-400 mg L^{-1} concerning their respective toxicities.[14]

Due to their mobility, solubility in water, and bioaccumulation potential in organisms, phenolic compounds are a threat to human health, as exposure to small amounts of these compounds can cause instant poisoning and lead to death.[13, 15] Phenolic compounds are volatile and may generate toxic vapors.[13] When inhaled, they irritate the respiratory tract, leading to respiratory insufficiency.[13, 16] Phenolic vapors can also cause eye irritation, leading to serious damage to the visual system and possibly blindness.[13] Excessive exposure to phenol and its derivatives can lead to disruption of the central nervous system, causing muscle spasms, tremors, convulsions, and paralysis.[1, 16] The monitoring of phenolic compounds has been a major concern worldwide given the critical risks that these compounds can generate to the ecosystem. As a consequence, the development of reliable, reproducible, sensitive, rapid, and low-cost analytical sensing methodologies for the comprehensive and on-site monitoring of phenolic compounds in the natural environment is both necessary and of great interest.

Many efforts have been made to develop efficient methods for detecting trace levels of phenolic compounds in natural water. Currently, the most frequently used detection techniques for this purpose are the conventional chromatographic and spectrophotometric techniques, such as high-performance liquid chromatography[17] and gas chromatography[18], fluorescence spectroscopy[19], infrared spectroscopy[20], and mass spectroscopy.[21] These techniques have been widely used due to their accuracy and sensitivity. Nevertheless, it is a known fact that these conventional techniques have limitations including complex methods with extensive sample pre-treatment, need for laboratories with infrastructure and equipped with expensive instruments, besides qualified personnel.[22] In addition, the use of these techniques for routine and real-time applications becomes unfeasible. Therefore, this is the starting point for developing reliable electrochemical sensing strategies for phenolic compounds using inexpensive equipment and easy-to-use methods with the possibility of portability for on-site and real-time analysis.

1.2.2 Electrochemical methods for phenolic compounds detection

The development of electrochemical sensors and biosensors has been proposed as a promising alternative for monitoring phenolic compounds in natural water.[23] When associated with the electrochemical processes (oxidation/reduction), as well as with the use of novel nanomaterials[3], for instance, carbon nanotubes[24], graphene[25], molecularly imprinted polymers[26], and quantum dots[27], these devices became as sensitive and reliable as chromatographic ones, but with advantages of portability and easy-to-use, allowing in situ and real-time analysis.

Li *et al.* (2017) developed a novel composite based on cyclodextrin and chitosan-functionalized reduced graphene oxide on glassy carbon electrode (RGO-CD-CS/GCE) for simultaneous determination of 4-NP and 2-NP in water samples.[28] The enhancement of the signal detection and consequently an improved sensitivity were achieved due to the host-guest recognition sites on cyclodextrin. A second-order derivative deferential pulse voltammetry (2D-DPV) was performed, and the detection was possible based on the nitroaromatic/hydroxylamine redox reactions of 4-NP and 2-NP at RGO-CD-CS/GCE, reaching detection limits of 0.016 and 0.018 µM, respectively. Chen and co-workers (2019) developed another successful electrochemical strategy based on modified GCE with copper oxide-histidine functionalized graphene quantum dots (CuO-His-GQD) for the amperometric detection of HQ by using DPV.[27] In this study a limit of detection of 0.31 nM was achieved and the applicability of the proposed sensor was studied for the determination of HQ in natural water samples. Recently, Guo *et al.* (2019) designed an electrochemical sensor based on modified GCE with zeolitic imidazolate framework-67 and multiwalled carbon nanotubes (ZIF-67/MWCNTs-COOH/Nafion) composite for the simultaneous determination of Acetaminophen (AC) and 4-AP.[29] Limits of detection of 0.01 and 0.07 µM were obtained for 4-AP and AC, respectively. The recovery study was performed to demonstrate the successful applicability of the electrochemical composite sensor for AC detection in river water samples. Therefore, these are some examples that prove considerable efforts have been made to develop new and innovative electrochemical strategies based on the synthesis and integration of advanced and sustainable nanomaterials to improve the analytical signal for the quantification in the µM and nM range of phenolic compounds.

One of the most investigated electrochemical sensors for the analysis of phenols and their derivatives are enzyme-based biosensors.[30] Phenol oxidases such as laccase, tyrosinase, and horseradish peroxidase are a group of enzymes that have recently been widely used to design biosensors due to their ability to oxidize phenolic compounds in the presence of oxygen.[31] Thereby, studies have reported the successful use of these enzyme-based biosensors for the detection of phenolic compounds.

Fartas *et al.* (2017), developed an electrochemical biosensor based on the immobilization of tyrosinase on graphene-decorated gold nanoparticles/chitosan nanocomposite (Gr-AuNPs-Chit-Tyr-SPE) for amperometric detection of phenolic compounds.[32] Limits of detection of 0.016, 0.02, 0.031, 0.024, 0.041 µM were calculated for phenol (Ph), catechol (CT), 4-NP, 4-chlorophenol (4-ClP) and 2,4-dichlorophenol (2,4-DCP), respectively, and sensitivity ranging from 0.213 to 0.624 µA μM^{-1}. The proposed biosensor showed a decrease of 15% in its original amperometric response after one month of storage at 4 °C. Another study based on an amperometric biosensor using horseradish peroxidase was developed by Zhang and co-workers (2012) for the detection of Ph and 4-ClP.[33] The proposed biosensor is based on the modification of glassy carbon electrode by horseradish peroxidase immobilized on partially reduced graphene oxide (HRP-partially rGO/GCE). They attributed the improved electrochemical properties of the biosensor to the partially rGO which promotes the electron transfer between the enzyme HRP and the GCE. Limits of detection of 4.4 and 15.2 µM were achieved for Ph and 4-ClP, respectively. The stability and reusability of the biosensor were investigated after 7 days of storage at 4 °C and a decrease by 7.0% and 7.3% in the current response of Ph and 4-ClP were observed. Recently, a biosensor based on a polyaniline/magnetic graphene composite mediated by laccase (PANI/MG-Lac-GCE) was proposed by Lou and coauthors (2020) for the amperometric detection of HQ.[34] By using the biosensor, they achieved a limit of detection of 2.94 µM and sensitivity of 0.0364 $\mu A\ \mu M^{-1}\ cm^{-2}$. The authors also reported a decrease by 3.3% in the amperometric response of HQ after 2 weeks of storage at 4 °C. Although there are a large number of studies in this field reporting good results in terms of sensitivity and limits of detection in the µM range, there are always some disadvantages with electrochemical based biosensors. Interference from enzyme inhibitors or electroactive species in the electrochemical detection by the transducer, as well as enzyme denaturation and limitations related to stability and high cost may limit the feasibility of disposable enzyme-based biosensors for large-scale production and real monitoring application.[30]

Another issue commonly reported in the use of the (bio)sensors associated with conventional electrochemical techniques, such as cyclic voltammetry (CV), square wave voltammetry (SWV), differential pulse voltammetry (DPV), and linear sweep voltammetry (LSV) for analytical detection, is the instability of background current (Fig. 1.3), partly from the double-layer charging, which can influence the sensitivity of the method.[35] In this case, one of the possible solutions to overcome this problem is to resort to baseline correction. Although this is not always a reliable option.

Figure 1.3 – (a) DPVs of HRP/CRG24H/GC electrode in phosphate buffer acquired during the successive addition of p-chlorophenol (b) DPVs of HRP/CRG24H/GC electrode in phosphate buffer acquired during the successive addition of phenol.

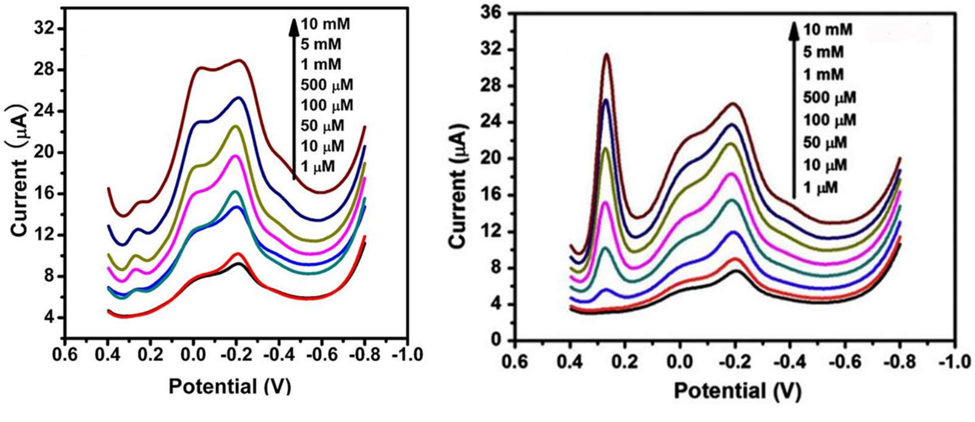

Source: Adapted from Zhang *et al.*, 2012.

While much work is still needed to overcome the disadvantages of using electrochemical (bio)sensors, this can still be considered a preferred option for monitoring phenolic compounds in terms of portability, fast screening results, and the possibility of development of eco-friendly platforms by using sustainable and biodegradable materials reducing the environmental impact.[36]

1.2.3 PEC sensors

The development of photoelectrochemistry has started in 1839 by Edmond Becquerel with the study of the conversion of electromagnetic radiation into electrical energy, resulting in the discovery of the photovoltaic effect.[37] Later, in the 1960s, Heinz Gerischer studied in detail the physicochemical interaction between the light source and the electrochemical processes on the surface of semiconductors, becoming one of the pioneers in the development of applied photoelectrochemistry.[38] Since then, the interest in the study of photoelectrochemistry has grown substantially, focusing primarily on the development of renewable energy conversion and storage. In this regard, photo-driven processes have been widely explored for photovoltaics, photocatalysis, and photosynthesis applications.[39] In parallel, the oxidation and reduction reactions that take place at the semiconductor/electrolyte interface have also gained attention over the years and the study of photoelectrochemistry for sensing applications has been widely developed.[37, 40]

Recently, the PEC sensing technique emerged as an attractive alternative for analytical chemistry which has been developed and applied for monitoring organic and inorganic pollutants. The interest in PEC sensing has increased exponentially over the years due to its superior properties for real application.[40] In this technique, a photoactive material, such as TiO_2 and ZnO, is used to collect the photon energy from a UV or visible light source and transform it into electron/hole (e^-/h^+) pairs. In a typical n-type semiconductor, the photogenerated hole may oxidize available molecules, while the photogenerated electron are promoted to the conduction band and generate a measurable anodic photocurrent. Alternatively, the cathodic photocurrent (or a reduction on anodic photocurrent) is expected when the photogenerated electron are transferred to available molecules (e^- acceptors) in the solution and at the same time undergo recombination with the photogenerated h^+ in the valence band.[41] In parallel, reactive oxygen species (ROS) like hydroxyl radicals ($^{\bullet}OH$) and superoxide ($^{\bullet}O_2^-$) are also generated at the surface of the semiconductor.[42] The generated photocurrent is recorded by a potentiostat and its magnitude depends on the electron flow in the semiconductor. The energy difference between the valence and conduction bands of semiconductor and insulator materials is called band gap, on the order of magnitude of electron volts (eV). Therefore, the band gap is the energy required to promote an electron from the valence band to the conduction band, where it can move freely through the crystal lattice and serve as a charge carrier for energy conduction.[43, 44] The electron promotion becomes possible due to a thermal excitation or through the incidence of light, as shown in Figure 1.4.

Figure 1.4 – Energy diagram for an n-type semiconductor under the incidence of a light source, resulting in the e^- promotion from the valence band (VB) to the conduction band (CB).

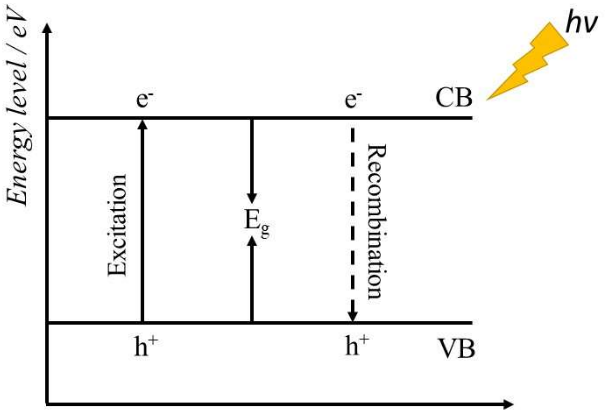

Source: Own authorship.

PEC sensing platforms contain three key components: light source, photoactive material, and signal recording setup. Specifically, photocurrent generation is only possible by a combination of factors, mainly the intensity and wavelength of the light source, the composition of the electrolyte solution, and the characteristics of the photoactive material, such as the type, size, and shape.[41] The generation of photocurrent signal involves foremost the photon absorption, charge generation, charge promotion/recombination, and charge destination that may directly assist the redox reactions in the electrode/electrolyte interface.[40] This new analytical approach has significant advantages compared to conventional electrochemical methods.[45] For instance, the complete separation between the electron excitation source and the analytical signal greatly reduces the background noise achieving higher sensitivity. Another notable advantage is that the PEC technique works without the dependence on an applied potential, considered one of the fundamental parameters used in conventional electrochemical methods (amperometric). These unique features are the main reasons why PEC sensing devices have become in recent years widely spread and studied in the scientific context.[40, 45, 46]

In PEC systems, the performance of the photoactive material and the efficiency of the photoconversion depends mainly on the strategies adopted for surface and/or structural modifications of these materials, hence improving their basic photocatalytic properties. In this regard, the photoactive material plays an important role in PEC sensing systems, since it acts as a transducer converting the electronic signal into a measurable photocurrent response.[47] Furthermore, an efficient signal transduction mechanism using suitable chemical or biological composites to achieve the improved design of the functional photoactive material with tailored characteristics enables its application in the most diverse PEC areas, as well as for the various sensing purpose.[46]

1.2.3.1 PEC-based sensing strategies

Currently, there are few studies dedicated to improve the physicochemical properties of photoactive materials, including organic polymers, metal oxides, and transition metal chalcogenides.[40, 41] Strategies to make a versatile and effective transducer for signal amplification always involve challenging tasks and therefore such studies have been seen as an innovative research topic.

Metal oxide photoactive materials

Among the different photoactive materials, metal oxides have attracted great interest in the construction of PEC sensors due to their functional properties, excellent biocompatibility, easy synthesis, eco-friendly, controllable size, and high crystallinity.[45] For instance, classical semiconductors ZnO and TiO_2 are considered promising photocatalysts and in recent years have been studied as catalyst support due to their stability and electron transfer ability.[42, 48] Even though these bare photoactive materials have great application in the PEC field, they have a fast electron/hole (e^-/h^+) recombination rate, large band gap, low absorption of the photons, and they are suitable only at the wavelength range of UV light.[49] Therefore, these characteristics limit the application of such materials for sensing purposes. To address the drawbacks of using the mentioned bare photoactive materials, different strategies such as doping and heterojunctions with equivalent or different bandgap materials, including dye sensitization and metal deposition, have been developed to improve optoelectronic conversion efficiency and to extend their application range.[45]

Heterojunctions

Since fast photogenerated charge recombination is a major problem of some photoactive materials and the separation/transfer of these charges is highly desired, heterojunctions are the most effective ways to suppress this drawback and influence the analytical performance of a photosensor. The separation of the photogenerated charges can happen more efficiently at the interface of different composites.[40] Heterojunctions are typically grouped as follow: semiconductor-semiconductor (S-S) heterojunction, semiconductor-carbon (S-C) heterojunction, semiconductor-metal (S-M) heterojunction, and multicomponent (MC) heterojunction.[40, 50]

In an S-S heterojunction, a specific semiconductor with a higher energy level injects photogenerated electron into the conduction band of a second semiconductor, increasing electron flow and consequently enhanced photocurrent response.[45] In addition, the spatial separation between semiconductors hinders the recombination of the photogenerated charges.[51] The junction between a p-type semiconductor and an n-type semiconductor is a well-established example of an S-S heterojunction, for instance, the heterojunction of the CuO/ZnO composite.[52] S-C heterojunction comprises carbon-based materials including single- and multi-walled carbon nanotubes, graphene (GR), and its derivatives, graphene oxide (GO) and reduced graphene oxide (rGO).[45] The intrinsic electronic properties of carbon-based materials, their high specific surface area, and superior flexibility ensure efficient charge separation and address the aggregation problems commonly observed in some semiconductors, as well as improve their photocatalytic activity.[53, 54] An rGO/ZnO/indium tin oxide coated glass (ITO)-based glucose photosensor developed by Zhou *et al*. (2020) is an example of S-C heterojunction.[55] The authors have found that the incorporation of rGO facilitates electron transfer between ZnO and ITO electrode, achieving an enhancement in sensor sensitivity by about 1.6-fold and decrease in the detection limit by 2.3-fold. S-M heterojunction involves the surface plasmon resonance (SPR) effect where metal nanostructures, for instance, Au, Pt, and Ag, improve light harvesting and photo-energy conversion ability of semiconductors.[40] Mendonça and coworkers (2021) have reported that the photocatalytic activity and light absorption of anatase-TiO_2 was greatly improved by the impregnation of size-controlled AuNPs for nM detection of HQ under visible light illumination.[56] On the other hand, MC heterojunction concerns the spatial integration of two or more photoactive materials to achieve both efficient electron photoconversion, and efficient photogenerated charge transfer.[50] In a typical MC heterojunction the photoactive material placed between two semiconductors acts as a charge recombination and electron storage center. For instance CdS/Au/TiO_2, the role of the metal is to contribute to the simultaneous interfacial vectorial electron transfer (CdS → Au → TiO_2) and effective charge separation in the respective semiconductors.[50, 57] The schematic illustration of the photocurrent generation and an overview of different examples of heterojunctions for a semiconductor material are displayed in Figure 1.5.[45]

Figure 1.5 - (a) Schematic illustration of semiconductor-based photocurrent generation: (I) the formation of charge carriers under illumination; (II) the trapping of a CB electron and the formation of cathodic photocurrent; (III) the trapping of a VB hole and the formation of anodic photocurrent. (b) Doped semiconductor. (c) S-S heterojunction. (d) S-C heterojunction. (e) S-M heterojunction. (f) MC heterojunction.

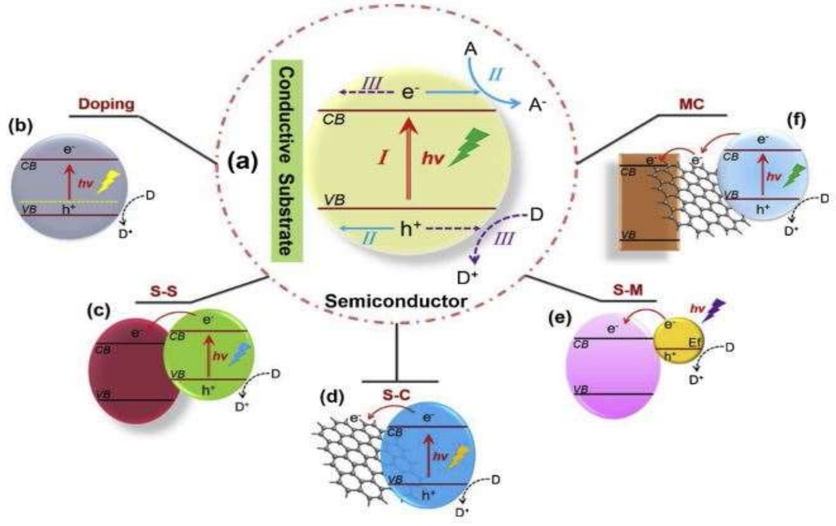

Source: Shi *et al*., 2019.

Moreover, element doping and surface sensitization have also been considered promising strategies for the development of photoactive materials with enhanced photocatalytic properties and improved visible light absorption.[40] For example, the synthesis of nitrogen-doped nanocrystalline TiO_2 (N-doped TiO_2) and the PEC device based on surface sensitization of TiO_2 using perylene-3,4,9,10-tetracarboxylic acid, showed high photocatalytic activity under visible light irradiation.[58, 59]

Photoelectroanalytical methods

PEC has become one of the most studied research topics in the analytical context owed to its authentic characteristics.[40] Associated to nanomaterials and/or integrated to other analytical techniques, PEC has been successfully applied for trace level detection of organic and inorganic pollutants in different matrices.[51] To improve the photocatalytic activity of photoactive materials, the fabrication of photosensors using novel materials and advanced architectures with unique characteristics has been reported in the literature. Therefore, given the fact that improved photocatalytic activity leads to increased sensitivity, the development of well-established photosensors opens up new opportunities for a wide range of analytical sensing domains.

Yan and coworkers (2018) developed an S-S heterojunctions PEC sensing platform based on carbon nitride and bismuth oxyhalide (CN/BiOBr) composite for the detection of an antibiotic drug, tetracycline (TC).[60] The intentional matching of the energy bands of the respective semiconductors (p-n heterojunction) reduced photogenerated charge recombination rates, leading to enhanced photocatalytic activity of BiOBr. Under visible light, the performance of the flower-like composite is drastically improved allowing the sensitive detection of TC and reaching a limit of detection of 8.5 nM. Another example of a p-n heterojunction PEC sensor was fabricated by Prado *et al*. (2020) based on the copper oxide-modified bismuth vanadate ($BiVO_4$/CuO) composite for naproxen (NPX) detection in sewage.[61] The authors found that the synergism between $BiVO_4$ and CuO prevented the charge recombination and the photocurrent generated was derived from the electrooxidation of NPX at the anodic bias of 0.9 V (*vs* Ag/AgCl). After optimization of experimental conditions the FTO/$BiVO_4$/CuO photosensor was able to detect NPX with a limit of detection of 4.9 nM. The real application was performed in sewage samples achieving a recovery percentage above 95%. Prado *et al*. (2019) also reported the determination of dopamine (DA) by using the same $BiVO_4$ photoactive material modified with graphene quantum dots (GQDs).[62] Under visible light irradiation, the efficiency of the charge transfer mechanism of FTO/$BiVO_4$/GQDs was confirmed enabling the oxidation of DA by using an applied positive potential (+0.4 V). The limit of detection for this method was estimated as 8.2 nM.

Wang *et al*. (2014) proposed a new PEC sensing mechanism for DA.[63] Interesting, the amperometric detection was based on the decreased photocurrent response. A photosensor based on ITO modified with CdS QDs was able to quantify the oxidized form of DA, i.e. benzoquinone (BQ), in the nM range reaching the limit of detection of 8.0 nM. The authors have found that BQ can act as an electron acceptor of the CdS QDs, blocking the electron transfer from the conduction band of CdS QDs to the ITO electrode. Also, another recent work investigated the decrease in photocurrent response of the photosensor for the sensitive determination of a known antibiotic, ciprofloxacin (CIP).[64] In this work, AuNPs of approximately 15 nm diameter were used to modify an ITO electrode acquiring the ITO/AuNPs photoelectrode. Increasing the concentration of CIP in solution resulted in a decrease in photocurrent intensity. According to the authors, the detection mechanism was based on the absorption of the CIP on the Au surface leading to a reduction of the electron transfer between AuNPs and ITO. A good linear correlation was observed and the limit of detection of 0.08 nM was achieved. A further example of a PEC sensing strategy based on decreasing of photocurrent response has been described by Sousa *et a*l. (2020). Based on the principle of MC heterojunction, the photosensor was constructed by modifying the FTO substrate with the CdS and TiO_2 composite sensitized with chloroprotoporphyrin IX iron(III) (CPPI). In addition to overcoming the charge recombination issues, the incorporation of the photosensitizer extended the response of TiO_2 into the visible range. The CPPI-TiO_2/CdS/FTO sensor was used to determine the flavanone naringin at zero bias potential. The authors achieved a limit of detection of 0.03 μM for naringin.

Photobioelectroanalytical methods

The introduction of bioinspired transducers in the PEC devices has been also widely reported as a novel strategy for sensing purposes. Interactions between semiconductor and analyte (targets) can be mediated by a biorecognition element such as enzymes[65, 66], aptamers[67, 68], and molecular imprinted polymers (MIP)[69, 70]. For instance, a successful PEC sensor based on the MIP-modified branched TiO_2 nanorods (B-TiO_2 NRs) was described by Sun and coauthors (2017) for the detection of the pesticide chlorpyrifos (CPF).[71] The MIP film was prepared by electro-polymerization of p-aminothiophenol (ATP) and CPF on the surface of the B-TiO_2 NRs. The interaction between MIP film and semiconductors was through hydrogen bonding. The MIP acts as an insulating layer hindering the harvesting photons and blocking the electron transfer. Therefore, the gradual decrease of photocurrent response was observed with increasing CPF concentration after removing the MIP template. The proposed photosensor showed excellent recognition capability specifically for the CPF molecule reaching a limit of detection of 21 pM.

A hybrid photolectrochemical biosensor based on the loading acetylcholinesterase (AChE) biomolecules onto 3D crossed bismuth oxyiodide nanoflake (BiOINFs) has been developed for the selective detection of organophosphate pesticides (OPs).[72] The hybrid sensing device provided greater mass transport and a higher visible light harvesting effect attributed to BiOI. Pesticide methyl parathion (MP) was used as a model molecule for experimental conditions optimization. Based on the enzyme-inhibition strategy, the AChE-BiOINFs/ITO was able to determine MP achieving a limit of detection of 0.15 nM. The applicability of the biosensor was evaluated in vegetable samples reaching recovery percentages above 96%.

Shang *et al*. (2019) proposed the construction of a high-performance aptamer-based photosensor with fast charge transport and efficient visible light absorption for the detection of the antibiotic tobramycin (TOB). The amorphous MoS_x (a-MoS_x) was electrodeposited on the surface of ZnO nanorods (ZnO NR) previously synthesized on ITO substrate for the enhancement of photocatalytic activity. A tobramycin-binding aptamer was employed as a recognition element. The detection mechanism was based on the capture of the TOB molecule by the aptamer resulting in decreased photocurrent response due to the suppression of interfacial charge transfer. Thereby, the bioinspired ITO/a-MoS_x@ZnO NR arrays/Apt photosensor was able to quantitatively determine TOB accomplishing a limit of detection of 12.2 pM.

A recent study was developed by employing light-responsive DNA probes for PEC detection of the DNA labeled chromophores erythrosine (DNA-EryB) and chlorin e6 (DNA-ChlE6) in the pM range.[73] Shanmugan *et al*. (2022) investigated the behavior of DNA probes linked photosensitizers responsible for singlet oxygen ($^1O_2$) generation upon visible light illumination. Using HQ as a redox reporter, the authors found the use of type II photosensitizers resulted in considerable photocurrent ranging 1-4 nA. In this study, the detectability of the chromophores-labeled DNA sequence was evaluated based on three different strategies. Capture of chromophores-linked DNA by hybridization to complementary DNA probes attached to the surface of magnetic beads was the selected strategy. Accordingly, the proportional increase of photocurrent with the concentration of labeled DNA was observed and the limits of detection were estimated as 10 pM and 17 pM and sensitivity of 213 A M^{-1} cm^{-2} and 116 A M^{-1} cm^{-2} for DNA-EryB and DNA-ChlE6, respectively.

Since chemical instability of biomolecules may be a disadvantage in bio-electrochemical systems, a similar situation may occur in bioinspired PEC systems, depending on the analytical conditions. On the other hand, a well-established methodology combined with optimized bioinspired photoactive materials has a significant gain in terms of sensitivity and selectivity owed to the specificity of the incorporated biorecognition materials.

1.2.4 New prospects: PEC sensing for phenolic compounds

Relevant studies on PEC sensors for the detection of phenolic compounds have been reported in the last few years. These works have been dedicated to the design of smart devices based on different electrochemical detection mechanisms. Herein, some examples will be further discussed.

A PEC sensing platform was developed based on the synthesis of vertically aligned TiO_2 nanorodarrays (NRAs) on the surface of FTO substrate and subsequently photosensitized with zinc phthalocyanine (ZnPc).[74] Surface sensitization of the NRAs allowed the amplification of TiO_2 light absorption in the visible region range. Furthermore, the efficient electron transfer from the excited state of ZnPc to the conduction band of TiO_2 occurs due to a longer lifetime of the dye in the excited state. The proposed ZnPc/TiO_2 NRAs/FTO sensor was used to quantify bisphenol A (BPA) through its oxidation by photogenerated hole (h^+) and consequent linear increase of the photocurrent response that was proportional to increasing concentration of the analyte in the solution. The limit of detection was estimated as 8.6 nM and the sensitivity of the method as 0.5764 $\mu A\ L\ \mu M^{-1}$.

In 2019 Yan *et al.* designed a novel heterojunction-based photosensor of bismuth-system oxides for 4-ClP assay.[75] The authors studied the construction of a binary heterojunction at the interface between the $BiPO_4$ nanocrystal and BiOCl nanosheets, allowing the amplification of the photoabsorption region of these semiconductors and the effective separation of the photogenerated charges to improve the performance of the PEC system. In this proposed PEC, 4-ClP was photoelectrochemically oxidized by photogenerated h^+ at the surface of the $BiPO_4$/BiOCl nanocomposite-modified ITO electrode allowing sensitive detection of 4-ClP. The limit of detection for this PEC system was calculated as 52.7 nM.

Based on another PEC detection mechanism, recent works have exploited the use of singlet oxygen as an intermediate to obtain oxidized phenolic compounds and subsequently generate a quantifiable amperometric photocurrent. Trashin *et al.* (2017) developed a biomimetic sensing strategy for amoxicillin by impregnating the photosensitizer perfluorinated ZnO phthalocyanine into TiO_2 (TiO_2-F_{64}PcZn).[76] Under visible light, the photosensitizer generates aerobically singlet-oxygen which is the responsible for the oxidation of analytes in solution, leading to electrochemically detectable products. The remarkable strategy resulted in improved sensitivity and a limit of detection of 20 nM for amoxicillin. Based on the same principle, Neven *et al.* (2019) studied the effects of varying electrochemical parameters, mainly pH and applied potential on the photocurrent cathodic response of cefadroxil (CFD), 4-AP, and doxycycline (DXC) by using the TiO_2-F_{64}PcZn under red-light for singlet oxygen generation.[77] Limits of detection of 20 nM, 0.2 μM, and 7 nM were calculated for CFD, DXC, and 4-AP, respectively.

Another PEC sensing proposal based on the generation and accumulation of ROS at the surface of HRP-impregnated TiO_2 under daylight, was described by Rahemi *et al.* (2020).[78] Photogenerated ROS potentiate the catalytic activity of the HRP enzyme toward phenols allowing the amperometric quantification of these compounds. The implementation of an FIA system to the PEC platform ensured good sensitivity (0.51 A M^{-1} cm^{-2}) and a limit of detection of 26 nM for 4-AP. In the same year, Mendonça *et al.* (2020) also reported the amperometric detection of 4-AP based on ROS generation at the surface of a commercial TiO_2 sensor integrated into an FIA system under UV light .[79] After an optimization study of the analytical parameters, the authors achieved a low limit of detection (18 nM) and sensitivity of 0.6 A M^{-1} cm^{-2}.

Using a molecularly imprinted polypyrrole (MIP), Wang and coauthors (2014) developed a bioinspired PEC sensor based on GR-modified CdS QD at the surface of the FTO electrode for the detection of 4-AP.[80] The authors found that a small amount of GR could facilitate the electron transfer of CdS, improving its PEC response under visible light illumination. MIP of 4-AP was electropolymerized on the surface of CdS GR by cyclic voltammetry. The specified binding of MIP from the assigned MIP/CdS-GR/FTO sensor was responsible for the selective detection of 4-AP with a limit of detection of 0.23 nM. Similarly, based on MIP as a recognition element, Yan *et al.* (2017) produce a self-powered sensing PEC platform, for the detection of 4-NP.[81] The proposed photosensor was designed based on the principles of the photocatalytic fuel cell, designating a PbS QDs-modified GCE as the cathode where 4-NP reduction takes place and a GR-modified GCE as the anode where acid ascorbic oxidation occurs. The oxidation of acid ascorbic at the photoanode provides the required power output for the system to achieve the self-powered sensing mechanism. The MIP was used as a recognition element to specifically bind 4-NP in the photocathode. The estimated limit of detection was 0.031 μM.

Many attempts have been made to make the PEC-based sensing even more well-structured and recognized as an analytical technique. Indeed, the PEC sensing technique is under constant development and advanced materials with significant results have been reported in the literature.[41, 45, 51, 82] Besides the efforts to transform PEC systems into a sustainable portable platform, improving the analytical performance, in terms of sensitivity, the limit of detection and selectivity, has been the main goal of PEC-based analytical methodologies, playing an important role in the prospects of environmental monitoring of organic pollutants.

1.3 LINK BETWEEN ARTICLES PRESENT IN THE BODY OF THE THESIS AND THE PhD PROJECT

The development of a nanometric photosensor for the quantification of 4-NP in supply water is the subject of the initial PhD research project. The results of the initial PhD project are presented in the chapters 4 and 5 of this thesis (data not yet published). To further explore the advantages of the PEC technique, as well as to develop other novel sensitive and efficient analytical strategies for the detection of phenolic compounds, the initial PhD project was extended giving rise to two more works (chapter 2 and 3 – published data). These works were developed in collaboration with the A-Sense Lab in Antwerp, Belgium, during the internship abroad. Therefore, the two self-authored published articles used to compose this thesis have a direct relation with the PhD project, since they present the development of PEC methodologies, using different photocatalyst materials, for the monitoring of the phenolic compounds in water samples.

1.4 OBJECTIVES

The overall objective of this thesis is to develop different photoelectroanalytical approaches for the effective detection of phenolic compounds (HQ, 4-AP, and 4-NP) in natural and supply water samples by using amperometric photosensors based on TiO_2 and ZnO semiconductors. Each chapter presents the development of a particular PEC sensing strategy and therefore has its respective specific objectives, as detailed below:

- Chapter 2:
    - Immobilization of commercial TiO_2 on graphite SPE to obtain the SPE|TiO_2 photosensor and integrate it into a PEC flow cell;
    - Optimize the experimental and operational conditions, such as flow rate, working potential, and pH, using HQ as a model molecule;
    - Apply the SPE|TiO_2 photosensor integrated into a FIA setup for the detection of HQ and 4-AP under UV illumination and estimate the LODs and sensitivities, as well as the repeatability, reproducibility, and stability of the SPE|TiO_2 amperometric sensor;
    - Evaluate the amperometric response of 4-AP in the presence of other phenolic compounds for the interference study;

- Use the proposed PEC setup for the detection of HQ and 4-AP in tap and river water samples to perform the recovery test.

➢ Chapter 3:

- Synthesize AuNPs to prepare the plasmonic catalyst (AuNPs@TiO_2) by impregnation into commercial TiO_2 via photo-assisted synthesis;
- Characterize the plasmonic catalyst by XRD, Raman, UV-vis spectroscopy, SEM-EDX, TEM, and LSV measurements;
- Modify graphite SPE with AuNPs@TiO_2 to obtain the SPE|AuNPs@TiO_2 photosensor and integrate it into a PEC flow cell;
- Study the effect of the amount of AuNPs loaded on TiO_2 on the PEC responses of HQ quantification under visible light (green laser source);
- Analyze the influence of flow rate, working potential, and pH on the photocurrent response in the presence of HQ at SPE|AuNPs@TiO_2;
- Evaluate the photocatalytic performance of SPE|AuNPs@TiO_2 integrated into a FIA setup for HQ and 4-AP sensing under the green laser illumination and the calculation of the LOD, sensitivity, repeatability, reproducibility, and stability of the proposed photosensor;
- Perform the interference study for HQ detection in the presence of other phenolic compounds;
- Apply the optimized AuNPs@TiO_2-based PEC sensing material for the detection of HQ and 4-AP in an effluent water sample to perform the recovery test.

➢ Chapter 4:

- Synthesize well-aligned ZnO nanorods to the FTO substrate by using a low-temperature electrodeposition method without the need to use a catalyst or seed layer;
- Study the effect of post-growth surface annealing treatment, in the range of 200 to 500 °C, on the crystallinity of ZnO nanorods, by morphological, electrochemical, and optical characterization;
- Evaluate the crystallographic planes for the synthesized ZnO nanorods and calculate the crystalline size for the nanorods as grown and annealed at 200 to 500 °C by using the XRD results;

- Investigate the behavior of diffraction and Raman peaks of ZnO nanorods with increasing temperature and evaluation of the surface of the synthesized nanostructures by SEM before and after annealing treatment, as well as their morphology and crystal structure;
- Verify by EDX and XPS measurements the presence of impurities in the ZnO films, studying the influence of the annealing treatment on the variation of the composition of O and C bonds present in the semiconductor material;
- Analyze the photocurrent transient behavior of ZnO nanorod films by LSV and chronoamperometric measurements under UV-light and evaluate their optical response before and after annealing treatment by UV-vis spectroscopy to calculate the band gap energy.

➢ Chapter 5:

- Modify ZnO nanorods surface annealed at 350 °C with the photosensitizer PTCA (FTO-$ZnO_{350\ °C}$|PTCA) for further enhancement of their photocatalytic activity;
- Characterize the FTO-$ZnO_{350\ °C}$|PTCA by chronoamperometry, UV-vis spectroscopy, XRD, FTIR, and XPS measurements;
- Study the electrochemical behavior of 4-NP using FTO-$ZnO_{350\ °C}$|PTCA under UV light and evaluate the effect of pH, support electrolyte, and applied potential on the amperometric response of 4-NP;
- Quantify the 4-NP by using FTO-$ZnO_{350\ °C}$|PTCA under UV light and determine the figures of merit of the methodology, such as stability, repeatability, reproducibility, and LOD;
- Perform the interference study on the PEC response of 4-NP;
- Apply the FTO-$ZnO_{350\ °C}$|PTCA photosensor for the detection of 4-NP in the river and tap water samples to perform the recovery test;
- Quantify the 4-NP by HPLC using an optimized method;
- Perform a statistical comparison study to assess the equivalence between the analytical results for 4-NP detection obtained by using the PEC and chromatographic methodologies.

CHAPTER 2

Photoelectrochemical sensing of the 4-aminophenol by using a TiO_2-based amperometric sensor integrated to a FIA system

This chapter describes the photoelectrochemical quantification of phenolic compounds such as hydroquinone (HQ) and 4-aminophenol (4-AP) accomplished by integrating the photoelectrochemical cell into flow injection analysis (FIA) setup. It is a well-known fact that during the electroanalysis of phenolic compounds, the electrode surface is susceptible to poisoning. However, the electrode fouling can be reduced significantly by using the FIA system with periodic wash sequences of the electrode. Reactive oxygen species (ROS), generated on the surface of TiO_2 under UV-light, can oxidize phenolic compounds, e.g. 4-AP. The oxidized form of 4-AP is reduced back at the electrode surface generating a measurable signal proportional to its concentration. The factors influencing the performance of the sensor such as flow rate, applied potential for back reduction and pH are investigated in detail. A straightforward analytical methodology for the on-site, highly sensitive and low-cost quantification of phenolic compounds is now presented based on using TiO_2 in a photoelectrochemical flow cell.

This chapter is reproduced from the article:

Integration of a photoelectrochemical cell in a flow system for quantification of 4-aminophenol with titanium dioxide, authored by ***Camila D. Mendonça et al.***, published in *Electrochemical Communications, v. 117, p. 106767, 2020*. https://doi.org/10.1016/j.elecom.2020.106767

2.1 INTRODUCTION

Flow injection analysis (FIA) is an approach for automated chemical analysis of organic contaminants.[83-87] This approach ensures a high mass transfer and provides clean electrode surfaces after periodic washing steps,[88] improving the method ruggedness and allowing a fast analysis.[89] In order to enhance the sensitivity of the detection, FIA has been combined with modified electrodes such as carbon nanotubes,[88] molecularly imprinted polymers,[90] graphene[91] and quantum dots.[92] This combination provides valuable setups with sensitivity and selectivity competitive to their chromatographic alternatives with the advantage of being portable, easy-to-use,[93, 94] enabling "in situ" and real-time analysis.

Another recent approach that has attracted considerable attention for the detection of organic compounds is photoelectrochemical analysis.[63, 95-98] Among different photoactive materials, titanium dioxide (TiO_2) is considered one of the most effective photocatalysts due to its high photo-activity and stability. It has been extensively used in water and wastewater treatment studies because it is chemically and biologically inert, cost-effective, non-toxic, and can promote the oxidation of organic compounds under UV illumination.[99-102] The band gap of TiO_2 is ~3.2 eV, depending on its crystalline form (anatase, rutile or brookite). Therefore, light with energy values greater than its band gap is required to excite electrons to the conduction band (CB) with the generation of holes in the valence band (VB).[99] The photogenerated electron-hole pairs may react with adsorbed species available on the surface of TiO_2, like OH^- and H_2O, producing reactive oxygen species (ROS) which may further oxidize phenolic compounds, allowing their quantification.[103]

Inspired by the advantages of FIA and TiO_2-based photoelectrochemical detections, we designed an analytical photosensing device for the amperometric quantification of 4-AP, an environmentally hazardous and toxic molecule. Commonly, 4-AP is used in the manufacture of pharmaceutical and cosmetic products; furthermore, it is used as plasticizer, petroleum additive or solvent.[104, 105] When it is discarded, this molecule reaches the environment, mainly via aqueous systems, generating a series of problems for living organisms such as genotoxic, hepatotoxic and mutagenic effects.[105] Therefore, the development of a sensitive, fast and reproducible method to quantify 4-AP is requested.

There are different analytical methods to determine 4-AP, including high performance chromatography,[106-108] capillary electrophoresis[109] and chemiluminescence.[87, 110] These methods are known to have a low limit of detection (LOD), high sensitivity and accuracy, but, compared to electrochemical methods, they have some disadvantages such as essential sample pre-treatment, time-consuming, and costly.

Although, various electrochemical sensors have been developed to detect 4-AP[111-116] but most of them have a long procedure for modification of the electrodes and they have quite a high LOD. In our work, commercial TiO_2, illuminated with UV light, combined with a FIA system is used for nM-range detection of phenols with a more straightforward and low-cost procedure. In addition, in comparison to a steady-state batch system, the integration of flow systems into a photoelectrochemical cell provides high sensitivity and, consequently low LOD and high reproducibility, due to periodic wash sequences preventing the electrode surface from poisoning.

2.2 EXPERIMENTAL

2.2.1 Materials

Nafion® 117 (5% in a mixture of lower aliphatic alcohols and water), potassium chloride (KCl), 2-aminophenol (2-AP), 3-aminophenol (3-AP), 4-aminophenol (4-AP), bisphenol A (BPA), 2-chlorophenol (2-ClP), 3-nitrophenol (3-NP), phenol, and potassium phosphate monobasic (KH_2PO_4) were purchased from Sigma-Aldrich. Hydroquinone (HQ) was obtained from Acros, TiO_2 (Millennium PC500, mesoporous) from Crystal Global (prior to use, the TiO_2 was calcined to 450 °C to enlarge its pore size) and 2-[4-(2-hydroxyethyl)-piperazinyl] ethane sulfonic acid (HEPES) was purchased from VWR®. The graphite screen printed electrode DS 110 was obtained from Metrohm DropSens. 10 mM KH_2PO_4 phosphate buffer and 0.1 M KCl solution (pH 7.0) was used as supporting electrolyte. The phosphate buffer solution was set to pH 7.0 using a NaOH solution. All reagents were used without further purification and all solutions were prepared with deionized water.

2.2.2 Apparatus

A homemade flow cell, made of poly(methyl methacrylate) (PMMA) with dimensions 22.75 x 8 mm (internal) and 36.75 x 25.55 mm (external) and with an internal volume of 0.15 mL, was used for the amperometric measurements of 4-AP and HQ (Fig. S2.1). A peristaltic pump (Perkin-Elmer, France) propelled the buffer into the flow line with a flow rate of 1 mL/min using Tygon tubing and omnifit labware (Diba). A manual sample injection valve was used to inject 50 μL of the sample solution into the carrier stream. Electrochemical measurements were carried out using a PalmSens (Utrecht, The Netherlands) controlled by PSTrace software (version 5.6).

A UV LED (blue light, $\lambda_{peak} = 400$ nm, 10 mW) was used for the excitation of the titania material (purchased from Kingbright, Germany). The distance between the LED and the surface of the electrode in the flow cell was 1.2 cm.

2.2.3 Electrode modification

The screen-printed graphite electrode (SPE) was modified with 10 g L^{-1} of TiO_2 dispersed in a solution of Nafion® (76:24, v/v HEPES 25 mM and Nafion®). Nafion® as an adhesive binder was used in order to provide better stability to TiO_2 at the surface of the electrode. A volume of 5 µL of the suspension was dropped on the surface of the electrode and dried at room temperature in the dark for approximately 2 h, obtaining the modified electrode described as SPE|TiO_2.

2.2.4 Analytical procedure

The flow rate, working potential, and pH were optimized in order to improve the amperometric response. All the electrochemical measurements were conducted using chronoamperometry and four measurements were performed per each experiment (n = 4), for the deviation studies.

The proposed photosensor and the optimized setup were used to detect HQ as a model molecule and 4-AP. The photocatalytic mechanism of 4-AP oxidation is expected to be the same as for HQ. Therefore, HQ was selected as a model molecule to optimize the experimental conditions. The LOD was calculated by the equation: LOD = $3s_b/a$, where s_b is the standard deviation of the blank and a is the slope of the calibration curve.

The river water was collected from Scheldt river at Lillo, Antwerp district, Belgium (Coordinates: 51° 18’ 8.0676”N 4° 17’ 11.3604”E). The river water sample was previously filtered using 0.2 µm polyethersulfone (PES) purchased from VWR®. The two stream flow tubes were separated and one of the tubes was used for Milli-Q water as a carrier solution of the sample and the other one was used for twice concentrated buffer solution (20 mM KH_2PO_4 containing 0.2 M KCl). Subsequently, the double concentrated buffer will get mix with MQ water (line E, Fig. S2.1) and the final concentration of buffer will be 10 mM KH_2PO_4 containing 0.1 M KCl.

2.3 RESULTS AND DISCUSSIONS

2.3.1 Electrochemical behavior of HQ at SPE|TiO_2 under UV illumination

The photocatalytic efficiency of TiO_2 under UV illumination in the presence of HQ using the FIA system is studied. Photocatalyzed reactions are facilitated through the presence of ROS on the surface of TiO_2.[78, 117] Authors in their previous publication[78] by using EPR method showed that TiO_2 can generate ROS under light illumination. These species with a free unpaired electron, are formed upon reaction of photo-generated electron-hole pairs with an adsorbed molecule (such as O_2 or H_2O) on the surface of TiO_2. The produced ROS may further oxidize phenolic compounds such as HQ. When a negative potential is applied the oxidized form of HQ, benzoquinone (BQ), reduces back to its original form and the reduction current is recorded. The SPE|TiO_2 electrode showed intense responses to HQ in the range of 0.0125 – 2.5 µM (Fig. 2.1, Fig. S2.2).

Figure 2.1 - Calibration curve for 0.0125-25 µM HQ at SPE|TiO_2 under UV illumination in 10 mM KH_2PO_4 containing 0.1 M KCl (pH 7.0), applied potential -0.14 V vs Ag pseudo reference electrode (n = 4). Flow rate: 1 mL/min. Inset: Linear curve 0.0125 – 2.5 µM HQ under UV illumination (black) and in the absence of a light source (red).

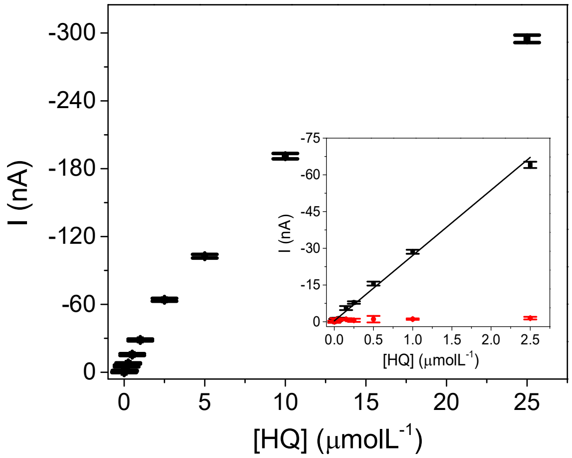

Source: Mendonça *et al.*, 2020.

As can be seen in the calibration curve (Fig. 2.1 inset red), the responses at SPE|TiO_2 in the dark are very low upon the addition of HQ (Fig. S2.3). A similar behaviour was observed when the bare graphite electrode was used instead of TiO_2 (Fig. S2.4). Indeed, in the absence of light source (Fig. 2.1 inset) and in the absence of TiO_2 (Fig. S2.4), ROS formation is not expected, meaning that the detection of HQ is only possible when TiO_2 is illuminated with UV.

The LOD and the sensitivity obtained for HQ on SPE|TiO_2 under UV light were 31.2 nM and 0.2 A M^{-1} cm^{-2}, respectively, with a repeatability of 4.5% RSD (n = 10 per electrode for five different electrodes in the presence of 2.5 µM HQ). The reproducibility was 8.5% RSD which is calculated from the sensitivity of an electrode during inter-days measurements (n = 5) in the concentration range of 0.0125 – 2.5 µM HQ (Fig. S2.5). The stability was evaluated by following the changes in the photocurrent of 2.5 µM HQ after 50 injections during 100 min of uninterrupted measurement. A decrease of only 5.4% in the amperometric response was observed. This exceptional stability can be explained by the chemical stability of TiO_2 and the properties of a typical FIA setup that allows accurate results even after a considerable measuring time.[118-120]

2.3.2 Effect of flow rate

One of the main advantages of FIA, improving the LOD, is higher mass transport to the working electrode surface in comparison to the stagnant electrochemical cell. This characteristic can be affected by the flow rate.[121] The latter is a crucial parameter to be optimized in FIA because it defines the contact time of the sample with the surface of the electrode. The flow rate optimization was conducted in a range between 0.25 – 1.5 mL min^{-1} (Fig. S2.6) by measuring the photocurrents of 2.5 µM HQ. According to the obtained photocurrents, there is no significant difference between different flow rates. Therefore, the flow of 1.0 mL min^{-1} was selected as it ensures a fast analysis and prevents wasting a large amount of buffer solution.

2.3.3 Effect of working potential and pH on the photocurrent of HQ

As the sensitivity of the electrode is influenced by the applied working potential, the effect of the working potential is investigated over a potential range from 0.1 to -0.3 V in a solution containing 2.5 µM HQ. The photocurrent and the background current (baseline) increase as the applied potential shifts towards more negative values (Fig. 2.2, Fig. S2.7), due to the presence of other reactions, such as the reduction of oxygen.[78, 122] To prevent the influence of other possible reactions and also to achieve a low background current, -0.14 V vs Ag pseudo reference electrode of the SPE was chosen as optimal working potential.

Figure 2.2 - Effect of working potential on the amperometric response of 2.5 μM HQ in 10 mM KH_2PO_4 containing 0.1 M KCl (pH 7.0) (n = 4). Flow rate: 1 mL/min. Inset: Changes in the background current upon applying different potentials.

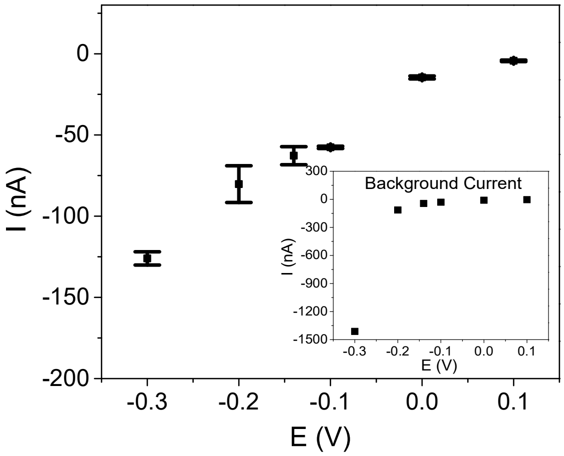

Source: Mendonça *et al.*, 2020.

The performance of SPE|TiO_2 in the presence of 2.5 μM HQ was evaluated in the pH range of 5.0 – 8.0 (Fig. 2.3). It is noticeable that the photocurrent increases with an increase in pH value until it reaches pH 7.0 and at pH > 7.0 the photocurrent response decreases. This trend is due to the fact that protons participate in the electrochemical reaction of HQ.[123]

Figure 2.3 - Effect of pH on the amperometric response of 2.5 μM HQ in 10 mM KH_2PO_4 containing 0.1 M KCl, applied potential -0.14 V vs Ag pseudo reference electrode (n = 4). Flow rate: 1 mL/min.

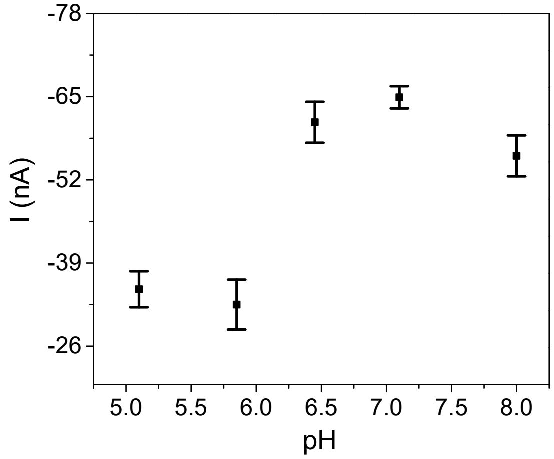

Source: Mendonça *et al.*, 2020.

At a low pH range (pH < 7.0), the hydroxyl group in the HQ structure can be protonated to R-OH_2^+.[124] While the pH is increasing from pH 5.1 until 7.0, the gradual deprotonation occurs and non-protonated hydroxyl groups at pH 7.0 contribute to the photocurrent response. HQ is a protic aromatic molecule and can easily get deprotonated at higher pH.[125] The shortage of protons at high pH (pH > 7.0) can be one of the reasons leading to a decrease in the photocurrent response.[123] Additionally, the isoelectric point of TiO_2 batch is ~6.8 and the surface of TiO_2 will be negative at basic pH. Therefore, the electrostatic repulsion between HQ and TiO_2 surface enhances with an increase of pH, which leads to lower photocurrents. In this sense, the reaction rate is favored at neutral pH. Thus, pH 7.0 was selected as an optimum pH for further experiments.

2.3.4 Photoelectrochemical response of the sensor for 4-AP

To explore the applicability of the electrode, 4-AP was measured at SPE|TiO_2 under UV light illumination. The calibration plot exhibits a typical current response of the electrode with increasing 4-AP concentrations (Fig. 2.4). The reduction peaks of 4-AP (Fig. S2.8) increased linearly with its concentration in the range from 0.0125 – 1.0 μM. The LOD and the sensitivity calculated for 4-AP were 18 nM and 0.6 A M^{-1} cm^{-2}, respectively.

Figure 2.4 - Calibration curve for 4-AP at SPE|TiO_2 under UV illumination in 10 mM KH_2PO_4 containing 0.1 M KCl (pH 7.0), applied potential -0.14 V vs Ag pseudo reference electrode (n = 4). Flow rate: 1 mL/min. Inset: Calibration curve for lower 4-AP concentration range 0.0125 – 1.0 μM.

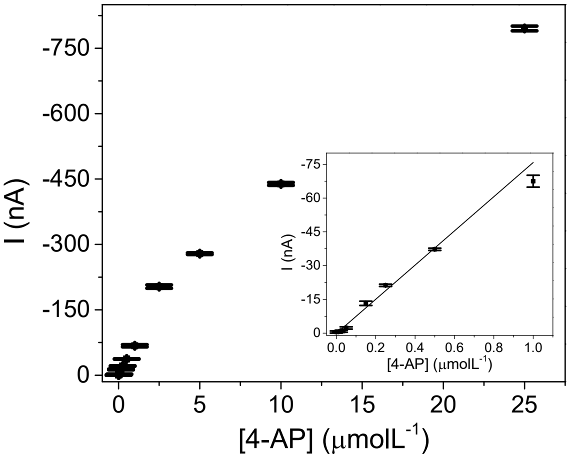

Source: Mendonça *et al.*, 2020.

The LOD for 4-AP in this work is at least five times lower than the reported LOD values in literature (Table 2.1) which demonstrates the favorable analytical performances of the proposed photosensor.

Table 2.1 - Comparison of the limit of detection for 4-aminophenol using flow injection analysis.

Method	Limit of detection (µM)	Reference
FIA combined with a glucose oxidase-mutarotase reactor	0.1 ± 0.01	[83]
FIA	0.39	[84]
FIA combined with MIP column	0.21	[90]
FIA with spectrophotometric detection	10.0	[126]
FIA with chemiluminescence detection	17.6	[127]
HPLC	3.00	[106]
FIA with PEC	0.018	This work

Key: FIA, flow injection analysis; PEC, photoelectrochemical; HPLC, high performance liquid chromatography.
Source: Mendonça *et al*., 2020.

The interference study is in the supplementary information and the results in Figure S2.9 show that there is no significant interference from other common phenolic compounds in the quantification of 4-AP.

2.3.5 Real sample analysis

The proposed setup was applied for the determination of HQ and 4-AP in tap water and river water. Standard addition was performed in three different fortification levels of HQ (0.75, 1.5 and 2.0 µM) and 4-AP (0.1, 0.4 and 0.74 µM) and the results were evaluated by the percentage of recovery as shown in Table S2.1. The average recovery values were found in a range of 90% to 108.9% for HQ and 93.5% to 106.9% for 4-AP, confirming the potential of the sensor for the determination of HQ and 4-AP in complex samples such as river water.

2.4 CONCLUSIONS

For the first time, we show that commercial TiO_2 without any modification under UV light illumination in combination with a flow system can be used to detect phenolic compounds at nM-level. The nanomolar detection capability of this sensor was illustrated by monitoring HQ and 4-AP in river water. The detection mechanism is related to the generation of ROS on TiO_2 under UV light illumination, evidenced by the control experiment in the dark. Overall, the results obtained with this photosensor confirm its usefulness and represents a valuable starting point to monitor the quality of water in situ and in real-time.

CHAPTER 3

Photoelectrochemical monitoring of the hydroquinone by using an AuNPs@TiO$_2$-based amperometric sensor integrated to a FIA system

In this chapter, the impregnation of size-controlled gold nanoparticles (AuNPs) on an anatase TiO$_2$ structure (AuNPs@TiO$_2$) was studied for the photoelectrochemical detection of hydroquinone (HQ) under visible light illumination integrated into a flow injection analysis (FIA) setup. The crystalline form of TiO$_2$ was preserved during synthesis and the homogeneous distribution of AuNPs over the TiO$_2$ structure was confirmed. Its photoelectrocatalytic activity was improved due to the presence of AuNPs, preventing charge recombination in TiO$_2$ and improving its light absorption ability by the surface plasmon resonance effect (SPR). The FIA system was used in order to significantly reduce the electrode fouling during electroanalysis through periodic washing steps of the electrode surface. During the amperometric detection process, reactive oxygen species (ROS), generated by visible light illumination of AuNPs@TiO$_2$, participate in the oxidation process of HQ. The reduction of the oxidized form of HQ, *i.e.* benzoquinone (BQ) occurs by applying a negative potential and the measurable amperometric response will be proportional to the initial HQ concentration. The influencing parameters on the response of the amperometric photocurrent such as applied potential, flow rate and pH were investigated. The linear correlation between the amperometric response and the concentration of HQ was recorded (range 0.0125 – 1.0 µM) with a limit of detection (LOD) of 33.8 nM and sensitivity of 0.22 A M^{-1} cm^{-2}. In this study, we illustrated for the first time that the impregnation of AuNPs in TiO$_2$ allows the sensitive detection of phenolic substances under green laser illumination by using a photoelectrochemical flow system.

This chapter is reproduced from the article:

Surface plasmon resonance-induced visible light photocatalytic TiO$_2$ modified with AuNPs for the quantification of hydroquinone, authored by ***Camila D. Mendonça et al.***, published in the *Electrochimica Acta, v. 389, p. 138734, 2021.* https://doi.org/10.1016/j.electacta.2021.138734

3.1 INTRODUCTION

Semiconductors-based photocatalysts have been widely used over the years in the fields of environmental applications and energy production.[101, 128, 129] Among a diversity of photocatalysts, titanium dioxide (TiO_2) is one of the best known and applied in several studies, such as in water and wastewater treatment, mainly due to its stability and cost effectiveness.[101, 130, 131] Furthermore, the numerous advantages of TiO_2 make it an attractive material for photocatalytic studies. Indeed, the material is biologically and chemically inert, non-toxic and commercially available, and it has excellent optical properties and efficient photocatalytic activity, being able to easily promote the oxidation of organic molecules.[99-101, 132, 133] However, the band gap of TiO_2 is approximately 3.2 eV (anatase, rutile or brookite crystalline form), allowing it to only absorb about 3 to 5% of the solar spectrum radiation on earth.[134] Therefore, in order to promote electrons from the valency band of TiO_2 to its conduction band and, consequently, generating holes in the valence band, it is required to employ a light source with an energy potential superior to TiO_2 band gap (*i.e.* $\lambda \leq 387$ nm).[99]

Photocatalyst-based photoelectrochemical platforms are promising sensing devices, because of their low cost, easy-to-use, portability potential, with low background signal, high sensitivity and stability.[133, 135] One of the most striking advantages of the photoelectrochemical analysis technique is related to the separation of excitation and detection sources, leading to a reduced background signal with a potentially greater sensitivity in comparison to the traditional electrochemical techniques.[40, 82, 136] However, the semiconductors-based photocatalysts, such as TiO_2, are affected by the high electrons/holes recombination rate, which may result in a low photocatalytic yield.[137, 138] Concerning about this, in an attempt to build an efficient, stable and powerful photocatalytic material, modifying the semiconductor-based photocatalyst with an appropriate material can be an effective way to overcome the above mentioned disadvantage. Over recent years, numerous studies have been carried out in order to enhance the photocatalytic activity of TiO_2 under the visible light spectrum by using various strategies such as surface modification with adsorbates[139, 140], semiconductor-metal heterojunction[141, 142], non-metal elements doping[143] and metal doping.[144, 145] Among those strategies, incorporation of plasmonic metal nanoparticles into TiO_2 nanostructures is a promising way because a specific light wavelength can excite plasmons in the metal nanoparticles. These plasmons give rise to energetic hot electrons that enhance the photocatalytic process.[146] When nanoparticles of noble metals, such as Au or Ag are incorporated into the TiO_2 matrix, the metal-semiconductor Schottky barrier facilitates the transfer of these hot electrons from the conduction band of metal nanoparticle to conduction band of TiO_2, through the interface.[145, 147] Furthermore, the plasmonic nanoparticles also concentrate light in their vicinity i.e. near-field, working as light harvesters enabling higher visible light absorption by TiO_2.[148] Therefore, TiO_2 photocatalytic activity and the sensitivity of the method can be significantly improved.[137, 149-153]

Among different plasmonic materials, Au nanoparticles (AuNPs) have the advantage of high stability, plasmonic activity and straightforward protocols for synthesis and impregnation into TiO_2.[137, 154] AuNPs-loaded TiO_2 (AuNPs@TiO_2) has been used in several fields, such as the photooxidation of organic molecules[155, 156], water and wastewater treatment[157, 158], photoelectrochemical cells[159] and dye-sensitized solar cells.[160] Since the plasmonic activity of AuNPs is size-dependent, the loading amount as well as the particle size of AuNPs play a crucial role in the improvement of the photocatalytic activity of TiO_2.[159, 161] The Au nanoparticles in TiO_2 facilitate absorption of visible light by the plasmonic excitation eventually resulting in hot electron injection and near-field enhancement.[148] According to an alternative hypothesis, the plasmonic Au nanoparticles can also be acting as an electron sink capturing the excited electrons from TiO_2 and reducing the electron-hole recombination.[137, 162] Thus, plasmonic Au nanoparticles can impart visible light activity to TiO_2 for numerous applications, including photoelectrochemical sensing.[163]

Photoelectrochemical TiO_2-based sensors have been widely explored for the quantification of organic compounds.[97, 135, 164, 165] Various studies have reported the application of photosensors for HQ detection, but most of them use UV as the light source[79, 166, 167] and/or have a high limit of detection (LOD).[166-168] Hence, in order to utilize visible light for the generation of photoelectrons and enhance the sensitivity of the photoelectrochemical sensing, the TiO_2 modified with AuNPs (AuNPs@TiO_2) was successfully integrated into a flow injection analysis (FIA) system for the nM-range detection of HQ in sewage samples. The AuNPs were impregnated into TiO_2 via a facile photo-assisted synthesis. The quantification mechanism is based on the production of reactive oxygen species (ROS) which can oxidize the target analyte. By applying a negative potential, the oxidized analyte is reduced back to its original form, generating a measurable photocurrent response proportional to its concentration in solution. The sensing platform was also used to detect 4-AP in the same matrix sample. According to the obtained results, the proposed photoelectrochemical sensor integrated into a FIA system represents a new perspective on the use of a portable and accurate setup for monitoring water quality.

3.2 EXPERIMENTAL

3.2.1 Materials

4-aminophenol (4-AP), 3-aminophenol (3-AP), 2-aminophenol (2-AP), bisphenol A (BPA), 4-nitrophenol (4-NP), 3-nitrophenol (3-NP), phenol (Ph), Nafion® 117 (5% in a mixture of water and lower aliphatic alcohols), gold (III) chloride trihydrate ($HAuCl_4.3H_2O$), potassium phosphate monobasic (KH_2PO_4) and potassium chloride (KCl) were purchased from Sigma-Aldrich. Mesoporous TiO_2 (Millennium PC500) was obtained from Crystal Global (previously calcined to 450 °C to enlarge its pore size), 2-[4-(2-hydroxyethyl)-piperazinyl] ethane sulfonic acid (HEPES) was purchased from VWR® and hydroquinone (HQ) from Acros. The graphite screen-printed electrode (SPE, DS 110) was purchased from Metrohm DropSens. A phosphate buffer solution (PBS) of 10 mM KH_2PO_4 containing 0.1 M KCl was used as the supporting electrolyte. A NaOH solution was used to set the pH of the buffer solution to pH 7.0. The deionized water was used to prepare all solutions and all reagents were used without purification.

3.2.2 Apparatus

Photoelectrochemical measurements were performed using a PalmSens4 potentiostat (Utrecht, The Netherlands) with PSTrace software (version 5.8). A photoelectrochemical flow cell made of poly(methyl methacrylate) (PMMA) with an internal volume of 0.15 mL and dimensions of 22.75 x 8 mm (internal) and 36.75 x 25.55 mm (external) was used during the amperometric analysis. A peristaltic pump (Perkin-Elmer, France) equipped with omnifit labware (Diba) and Tygon tubing was used to propel the buffer into the flow line system, at an optimized flow rate (1 mL/min) (Fig. S3.1). The flow system was equipped with a manual sample injection valve (volume of 50 μL).

A laser source (green laser, $\lambda = 532$ nm, 10 mW), model MGL-III-532 coupled to a power supply model PSU-III-LED, (purchased from Roithner LaserTechnik GmbH, Austria) was used for the initiation of the photocatalytic reaction. A distance of 1.2 cm was set between the surface of the electrode and the green laser.

3.2.3 Synthesis of AuNPS@TiO_2 and electrode modification

Prior to the preparation of the plasmonic catalyst (AuNPs@TiO_2), the AuNPs were synthesized using a modified Turkevich method.[169-172] Briefly, 1 mL of 0.01 M $HAuCl_4.3H_2O$

precursor solution was added in 98 mL of Milli-Q water (total concentration 0.1 mM) in a two-neck round-bottom flask and further heated up to 100 ºC. Under vigorous stirring, 1 mL of freshly prepared 1 wt.% sodium citrate solution was added and the reaction mixture was left at the boiling temperature for 30 min and cooled down to room temperature then stored in the refrigerator for further use. The colloidal AuNPs solution was stored in the refrigerator in order to avoid their aggregation at ambient conditions and preserve the long-term stability of nanoparticles. This phenomenon affects the photocatalytic properties of AuNPs.[173]

For the preparation of plasmonic catalyst, 10 mg of TiO_2 (Degussa P25) was photo-impregnated[174], with 10 mL of colloidal AuNPs solution (2.0 wt.%) under vigorous stirring and UVA irradiation (Philips Cleo UVA, 20 W, 365 nm) for 2 hours. The resulting solution was centrifuged and dried at room temperature. The procedure was repeated for higher amounts of Au loading on TiO_2 (15, 20 and 25 mL, means 3.0, 3.9 and 4.9 wt.%, respectively).

The SPE|AuNPs@TiO_2 sensor was obtained using the same modification procedure of graphite electrode described in our previous work.[79] Briefly, a suspension of 10 g L^{-1} AuNPs@TiO_2 dispersed in a solution of Nafion® containing 25 mM HEPES solution (76:24, v/v) was prepared and a volume of 5 µL from this suspension was used to modify the SPE graphite electrode. Subsequently, the electrode was dried in the dark at room temperature for approximately 2 h. Nafion® acts as an adhesive binder and ion conductor which ensures greater stability to the AuNPs@TiO_2 photocatalyst on the surface of the graphite electrode.

3.2.4 Characterization

The photometrics analyzes were performed to quantitatively determine the concentration of AuNPs loaded on TiO_2, by using a Spectroquant® photometer (NOVA 60 A) and a gold test kit purchased from MERCK.

The synthesized AuNPs@TiO_2 was characterized by scanning electron microscopy (SEM, model Zeiss EVO LS15) equipped with an energy dispersive X-ray detector (EDX, purchased from Bruker) to determine the elemental composition of nanoparticles. Data collection/processing was carried out using the AZtecEnergy software system, v. 2.1 (Oxford Instruments). The transmission electron microscopy (TEM) images were acquired by JEOL JEM-2100Plus operated at 200 kV.

In order to analyze the crystal structure of the AuNPs@TiO_2, X-ray diffraction (XRD) measurement was performed (Bruker, model D8 Advance). Raman studies were performed to evaluate the phases of AuNPs@TiO_2 sample, using Renishaw InVIA confocal scanning spectrometer, fitted with a 514 nm excitation source. The absorbance of AuNPs@TiO$_2$ was verified and its band gap energy was calculated from the results obtained by diffuse reflectance analysis, using a UV-DRS spectrophotometer (model V-630, Jasco).

The linear sweep voltammetry (LSV) was performed by a PalmSens4 potentiostat (Utrecht, The Netherlands) and PSTrace software (version 5.8) for the photocurrent transient study, using a step potential of 0.5 mV and scan rate of 0.25 mVs^{-1}, in the potential range between 0.4 V to -0.2 V.

3.2.5 Analytical procedure

The experimental and operational parameters referring to the proposed setup, such as the working potential, pH and flow rate were optimized in order to improve the photocurrent response. Chronoamperometry was used for all the electrochemical measurements. Deviation studies were performed based on three measurements made per each experiment (n = 3). The LOD was calculated by the equation LOD = $3s_b/a$ (s_b = standard deviation of the blank and a = slope from calibration curve).

The applicability of the proposed sensor was investigated by analyzing effluent water samples collected from the sewage treatment station Aquafin RWZI at Antwerpen-Noord, Belgium. The effluent water sample was filtered using a polyethersulfone membrane (PES) with a pore size of 0.2 μm, obtained from VWR®. The FIA system was equipped with two stream flow tubes and for the sample analysis one of the tubes was used for 20 mM PBS containing 0.2 M KCl and the other one for the carrier solution of the sample (Milli-Q water) (line A, Fig. S3.1). Thereafter, the buffer solution will be diluted by the carrier solution of the sample (E, Fig. S3.1), in order to obtain a final concentration of electrolyte of 10 mM PBS containing 0.1 M KCl (pH 7.0).

3.3 RESULTS AND DISCUSSIONS

3.3.1 Morphological study

The XRD diffraction pattern of synthesized AuNPs@TiO$_2$ is shown in Figure 3.1a. The results indicate that the AuNPs@TiO$_2$ sample is composed of an anatase (86%) and a rutile (14%) phase, which is in accordance with the reference patterns of JCPDS card number 83-2243 and 21-1276, respectively, depicted in Figure 3.1a. The diffraction peaks at 2θ values of 25.26°, 37.81°, 47.87°, 53.8°, 54.98°, 62.67° and 75° correspond to the crystallographic planes of (101), (004), (200), (105), (211), (213) and (215), respectively, related to anatase phase. Whereas, the peaks at 2θ values of 27.39°, 41.22°, 54.27°, 56.62° and 68.85° correspond to the rutile phase, and the crystallographic planes are (110), (111), (220), (002) and (301), respectively. The crystallographic peaks of metallic Au (JCPDS 04-0784) are not distinguishable in the diffraction pattern of AuNPs@TiO_2 sample due to its low concentration on the TiO_2 structure and a potential overlap between crystallographic peaks assigned to Au and anatase phase of TiO_2.[160, 175] The average crystallite size of AuNPs@TiO_2 was estimated from the average of full width at half-maximum (FWHM) at 25.26°, 47.87° and 62.67° corresponding to (101), (200) and (213) diffraction peaks of anatase phase, respectively, by using the Scherrer equation.[176] The calculated average crystallite size is 18.23 nm for AuNPs@TiO_2 sample. Figure 3.1b shows the Raman spectrum, in the range of 100-900 cm^{-1}. The Raman bands at 149.7, 195.4, 393.7, 511.1 and 634.4 cm^{-1} are related to the anatase phase. Increased intensity and a small shift of the Raman bands are observed. The red shift of the Raman band observed from 141.6 cm^{-1} to 150.1 cm^{-1} can be related to the surface enhancement by the impregnation of AuNPs, confirming the interaction between AuNPs and TiO_2 which implies an increasing of crystalline defects into TiO_2.[160, 175, 177] The crystalline defects can act as trapping sites for photogenerated electrons and then deliver them to a collecting electrode for the photocurrent generation.[175] The presence of metallic Au nanoparticles could not be distinguished in the Raman bands of AuNPs@TiO_2 because of the low concentration loaded into TiO_2 structure and the weak Raman sensitivity, as well as reported from XRD results.

Figure 3.1 - (a) XRD pattern of AuNPs@TiO_2 sample, anatase, rutile and Au references, (b) Raman spectra of AuNPs@TiO_2 sample and TiO_2 anatase reference. The AuNPs@TiO_2 sample is 3.0 wt.% of AuNPs loaded on TiO_2.

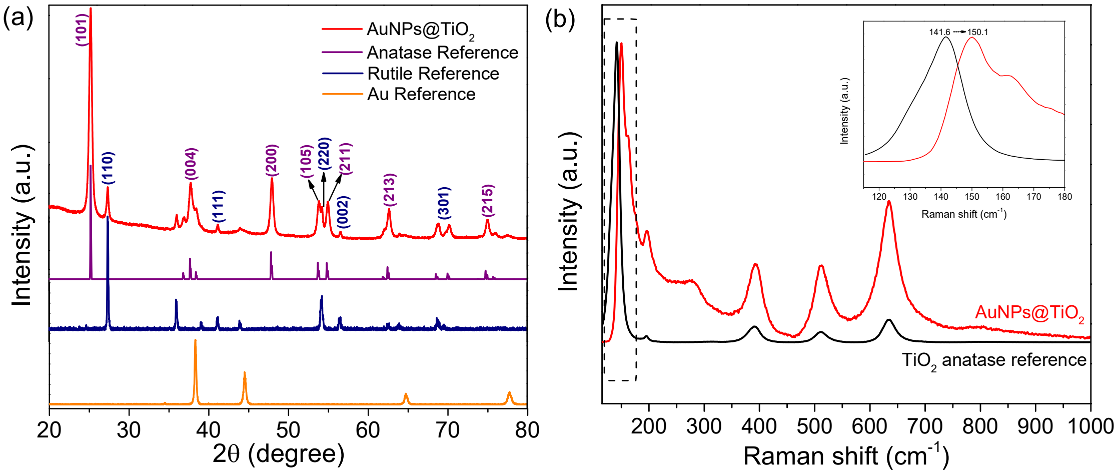

Source: Mendonça *et al*., 2021.

The morphology of AuNPs@TiO_2 (3.0 wt.% AuNPs loaded on TiO_2) and synthesized AuNPs is depicted in Figure 3.2. During the impregnation process, AuNPs and TiO_2 were assisted by UV irradiation in order to promote their interaction, through the use of photogenerated electrons from the TiO_2 surface reducing the Au source.[174] Figure 3.2a shows the SEM image of AuNPs@TiO_2 and Figure 3.2b highlights the EDX results, confirming the presence of metallic Au in the sample. The TEM images of AuNPs and AuNPs@TiO_2 are shown in Figure 3.2c and 3.2d, respectively. The average size of synthesized AuNPs is estimated to be around 18.7 ± 3.8 nm (Fig. 3.2c). The TEM analysis also illustrates that the AuNPs are loaded on TiO_2 and the structural features did not change during the photo-impregnation of AuNPs on TiO_2.

Figure 3.2 - (a) SEM image of AuNPs@TiO_2; (b) EDX patterns of AuNPs@TiO_2; TEM images of (c) AuNPs and (d) AuNPs@TiO_2.

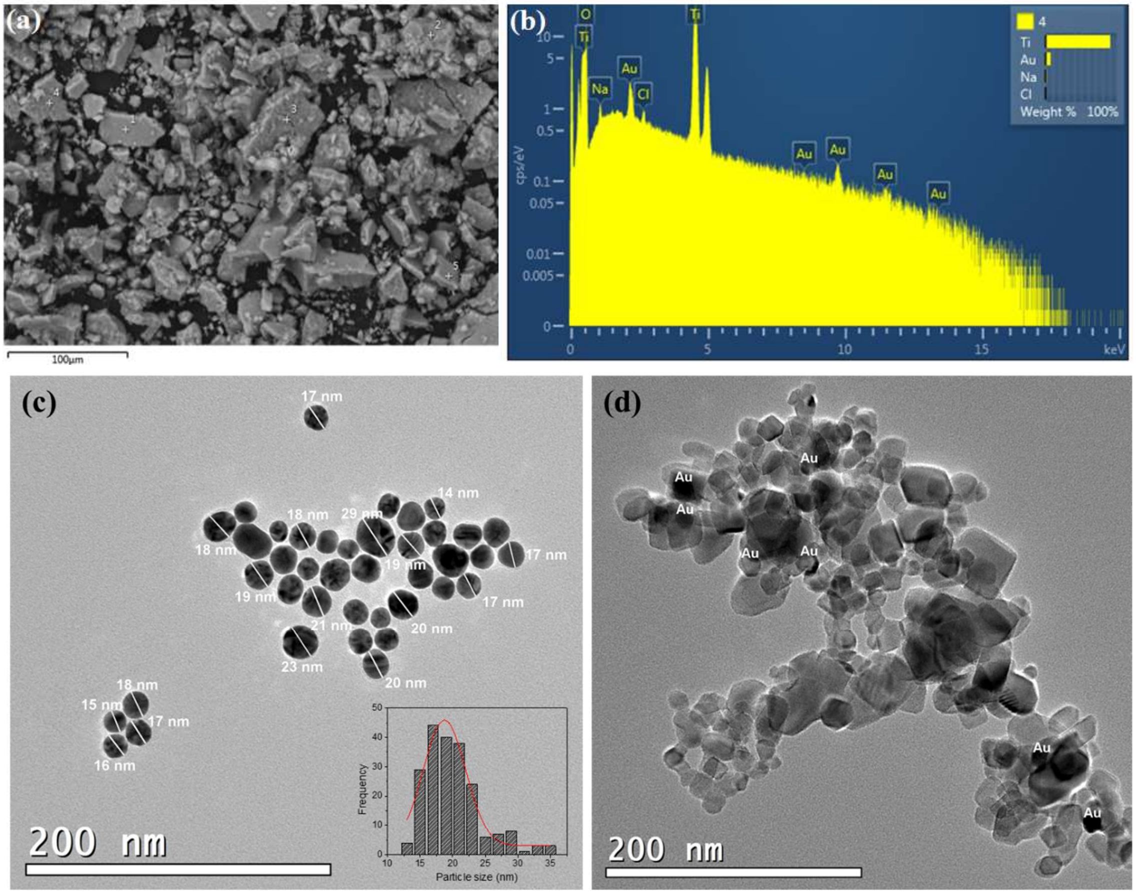

Source: Mendonça *et al*., 2021.

Since the amount of AuNPs loaded on TiO_2 might affect the photo-electrochemical responses, suspensions of AuNPs@TiO_2 with different concentrations of AuNPs were prepared

(2.0, 3.0, 3.9 and 4.9 wt.%) and their corresponding photocurrent responses towards benzoquinone (BQ) reduction recorded (Fig. S3.2). The highest response for the reduction of BQ to HQ (6.0 μM) was obtained for a 3.0 wt.% of AuNPs loaded on TiO_2. Therefore, 3.0 wt.% of AuNPs-loaded TiO_2 was selected as an optimal ratio to be used for the photosensor construction. The optimum amount of AuNPs loaded on TiO_2 (3.0 wt.%) was also quantitatively determined by using a Spectroquant® test kit for Au and the average of all measurements were found to be 2.98 ± 0.13 wt.% (n = 4).

Several parameters and phenomena are taking place, and will contribute to the final response. Firstly, by loading adequate amounts of AuNPs, a Schottky barrier is formed at the interface of Au and TiO_2[147], which significantly enhances the charge separation of holes and electrons and, thus, resulting in an increase of the photocurrent responses.[160, 174] On the other hand, by loading more AuNPs, they will occupy more active sites and extinguish a larger fraction of incoming light, inducing to a light screening effect. As a consequence, the light cannot reach the photocatalyst surface for efficient photogeneration of holes and electrons.[178] The photooxidation of Au by the photogenerated holes and OH radicals from the TiO_2 surface can also take place.[179]

UV-Vis absorbance spectra of AuNPs, TiO_2 and AuNPs@TiO_2 are shown in Figure 3.3a. The AuNPs and TiO_2 absorbance spectra exhibit a λ_{max} at 521 nm and 310 nm, respectively. The maximum absorption band for AuNPs@TiO_2 is at λ_{max} 554 nm, revealing the plasmonic resonance effect from AuNPs, indicating that metallic Au is presented in the sample, as already confirmed by the results of EDX and TEM analysis. The broad AuNPs@TiO_2 absorption response is related to the visible light absorption of AuNPs in the sample, which can be associated at least in part to its wide size distribution.[180] The band gap energy of AuNPs@TiO_2 was calculated using the Kubelka-Munk function (Fig. 3.3b).[181] The plot $(\alpha h\nu)^{1/2}$ *vs* $h\nu$ is used to determine the E_g by extrapolating the linear region of the curve to the point of intersection with the x axis, where the energy absorption of AuNPs@TiO_2 is observed. The band gap value was determined as 3.17 eV, which is very close to the theoretical band gap of 3.2 eV for anatase phase of TiO_2. This result demonstrates that the photocatalytic ability of TiO_2 can be significantly improved by incorporating gold nanoparticles on its structure.[137, 148, 149] In addition, the SPR properties of AuNPs in the visible range provide a broad spectrum of absorption for TiO_2.[182, 183] The UV-Vis absorbance spectra of colloidal AuNPs solution, AuNPs@TiO_2 suspension after impregnation and the supernatant of AuNPs@TiO_2 after centrifugation are presented in Figure S3.3. As expected, the absorbance spectrum of

AuNPs@TiO_2 suspension just after impregnation did not show the absorbance peak due to the light scattering by TiO_2 in solution. The results from Figure S3.3 confirm that there are no traces of AuNPs in the supernatant and corroborate to prove that AuNPs were successfully impregnated on TiO_2.

Figure 3.3 - (a) UV-Vis absorbance spectra of AuNPs, TiO_2 and AuNPs@TiO_2, (b) Tauc plot for the band gap energy determination of AuNPs@TiO_2 sample.

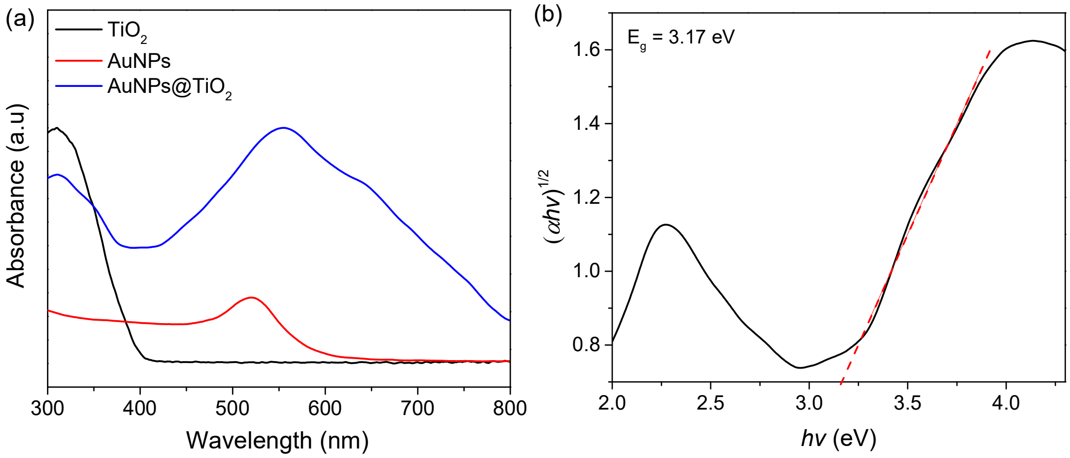

Source: Mendonça *et al.*, 2021.

Linear sweep voltammetry (LSV) was used to study the photocatalytic behavior of the material for HQ quantification. The linear sweep voltammograms of AuNPs@TiO_2 in the presence and absence of 1.0 µM HQ under chopped light illumination are shown in Figure 3.4. Reduction photocurrents are distinguishable in the presence of HQ. The recorded responses in the negative potential range are related to the reduction of BQ to its original form, *i.e.* hydroquinone (HQ), which was previously oxidized by ROS generated on AuNPs@TiO_2 surface under green laser illumination.

Figure 3.4 - Linear sweep voltammogram for AuNPs@TiO$_2$ electrode under chopped light illumination, in presence (red) and absence (black) of 1.0 μM HQ in 10 mM PBS containing 0.1 M KCl (pH 7.0), using a step potential of 0.5 mV, scan rate of 0.25 mVs^{-1} and potential range of 0.4 V to -0.2 V.

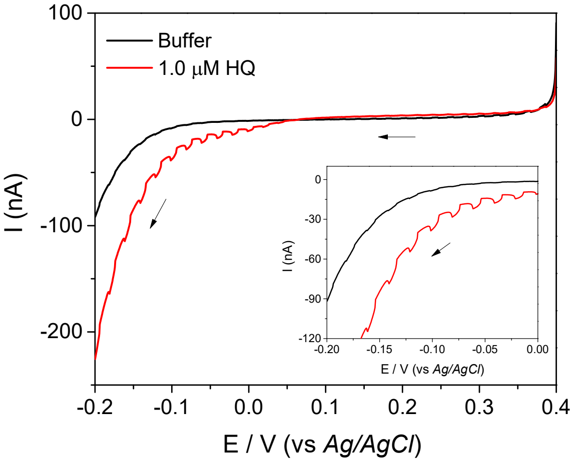

Source: Mendonça *et al*., 2021.

3.3.2 Photocatalytic performance of SPE|AuNPs@TiO$_2$ for HQ sensing

The photoelectrochemical behavior of HQ at the SPE|AuNPs@TiO$_2$ under green laser source and using a FIA system was evaluated. Typically, the band edges of a n-type semiconductor e.g. TiO$_2$, are affected by varying the applied potential.[184] At potentials more negative than the flat band potential of TiO$_2$, there is an excess of the majority charge carrier (electrons).[112] The cathodic current existent is potential-dependent because it corresponds to the flow of electrons from the conduction band (CB) of TiO$_2$ to the vacant states of the redox species in the electrolyte.[185] Because of the Schottky barrier on AuNPs/TiO$_2$ interface, the Au incorporated to TiO$_2$ acts as a co-catalyst and the photogenerated electrons induced by green light migrate from CB of AuNPs to TiO$_2$ CB, enabling the sequential oxidation of species on their surface.[147, 174, 186] Then the photoinduced electrons and holes in both TiO$_2$ and Au react with the molecules available at the surface to generate ROS (e.g. $^{\cdot}O_2^{-}$ and $^{\cdot}OH$).[78] Later, the generated ROS oxidize HQ in the electrolyte.[79] Thereby, the reduction of the oxidized form of HQ, *i.e*. benzoquinone (BQ) occurs by applying a negative potential and the measurable photocurrent response is proportional to the initial HQ concentration (Fig. 3.5).

Figure 3.5 - Expected photocatalytic reactions on AuNPs@TiO$_2$ surface under visible light (λ = 532 nm, green laser) and the photocurrent generation mechanism.

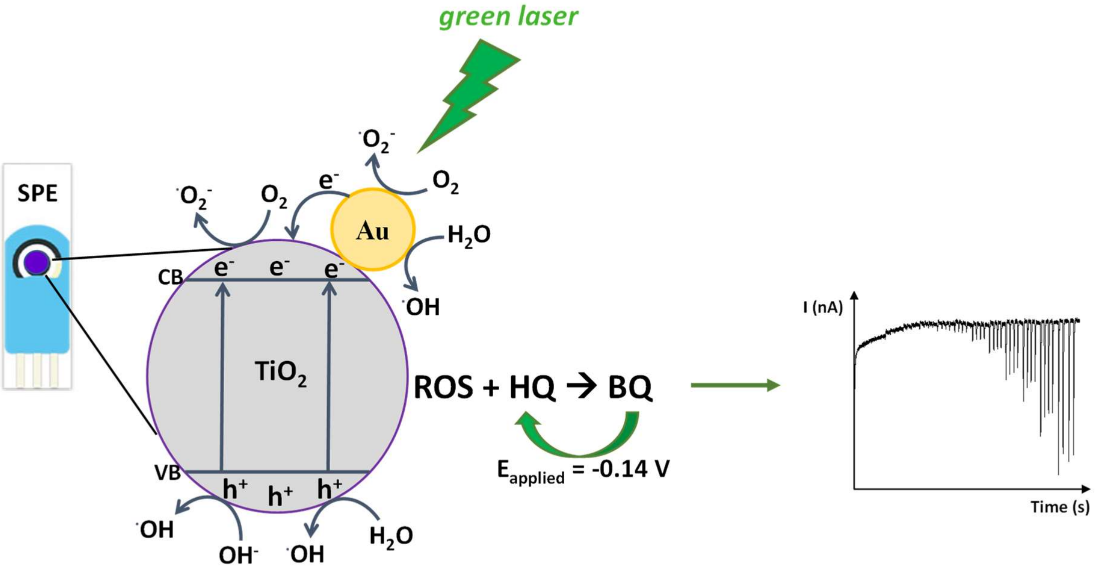

Source: Mendonça *et al*., 2021.

By analyzing the photocurrent response of the SPE|AuNPs@TiO$_2$ upon successive addition of different concentrations of HQ (Fig. 3.6A), a good linear correlation was recorded in the range of 0.0125 – 1.0 μM of HQ by applying a negative potential of -0.14 V versus Ag quasi-reference electrode (Fig. 3.6B).

Figure 3.6 - (A) Amperometric response for SPE|AuNPs@TiO$_2$ in the presence of HQ (a) 0.0125, (b) 0.025, (c) 0.05, (d) 0.15, (e) 0.25, (f) 0.5, (g) 1.0, (h) 2.5, (i) 5.0, (j) 10 and (k) 25 μM, in 10 mM PBS containing 0.1 M KCl (pH 7.0) and applied potential of -0.14 V vs Ag quasi-reference electrode (n = 3). (B) Corresponding calibration curve (inset: linear curve in the concentration range from 0.0125 to 1.0 μM at SPE|AuNPs@TiO$_2$ (black) and at SPE|TiO$_2$ (red) under green light illumination).

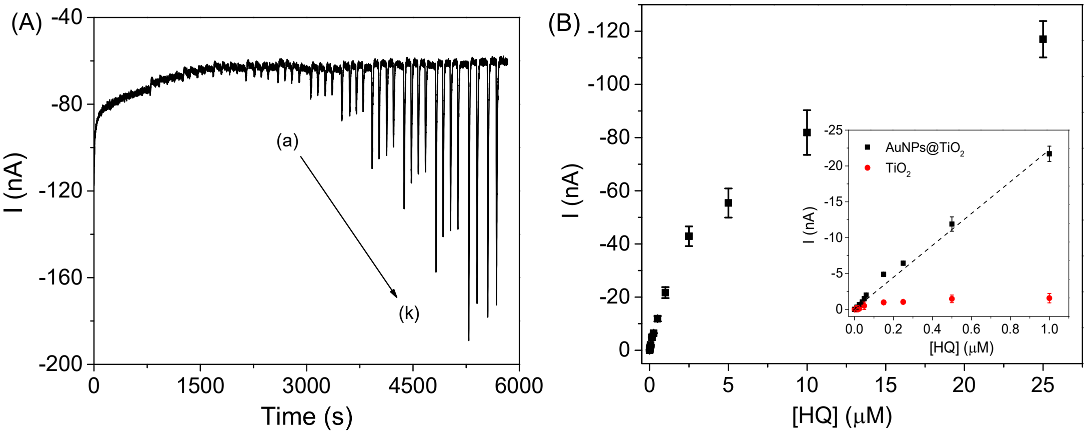

Source: Mendonça *et al*., 2021.

In order to confirm the AuNPs@TiO_2 photocatalytic activity under green light illumination for quantification of HQ, several control experiments were performed. The inset of Figure 3.6B shows a comparison between the photocatalytic activity of AuNPs@TiO_2 and TiO_2 under green light illumination. The photocurrent response using SPE|TiO_2 compared to SPE|AuNPs@TiO_2 for 1 μM HQ is about 14 times lower because TiO_2 has a very low photocatalytic activity under visible light illumination. Indeed, the impregnation of AuNPs can increase TiO_2 photocatalytic activity under visible light illumination (green laser, λ_{max} 532 nm).

The current responses for HQ detection were recorded using SPE|AuNPs@TiO_2 electrode in the absence of a light source. As it is shown in Figure S3.4, the amperometric responses at SPE|AuNPs@TiO_2 without the light illumination are very low. In the dark, the production of ROS is not expected or not sufficient to efficiently oxidize HQ in the electrolyte solution. The same happens when a bare graphite electrode is used under green laser illumination and by applying negative potential (Fig. S3.5). Switching the light source to UV LED, a low generation of ROS is observed and the photocatalytic activity of AuNPs@TiO_2 achieved is not optimal (Fig. S3.6).

The linear correlation between the amperometric response of SPE|AuNPs@TiO_2 under green laser illumination and the concentration of HQ was recorded with LOD of 33.8 nM and sensitivity of 0.22 A M^{-1} cm^{-2}. The repeatability study of the electrodes showed a variation of 7.7% RSD in the amperometric response of 1.0 μM HQ (n = 10 per electrode for five different electrodes). Reproducibility was achieved as 18.8% RSD, in the concentration range of 0.0125 – 1.0 μM HQ, confirmed by the sensitivities obtained during inter-days measurements (5 days) using the same electrode (Fig. S3.7). A decrease of 9.3% in the amperometric response of 1.0 μM HQ was observed, after 50 injections (approximately 100 min of measurement), using a single sensor.

The proposed photosensor presented a good performance and the analytical comparison with various previously reported sensors is shown in the Table S3.1. The LOD calculated for HQ using SPE|AuNPs@TiO_2 electrode is at least three times better or comparable to that reported in literature. In our previous work[79], we have demonstrated a successful integration of the TiO_2 sensor into a photoelectrochemical flow cell for HQ detection by using a UV (blue light) as illumination source, providing low LOD. In the present work, the improvement of the visible-light photocatalytic activity of commercial TiO_2 by the impregnation of AuNPs into its structure, as well as the integration of the photosensor into a FIA system, even allowed the nM-range detection of HQ. The impregnation of AuNPs into TiO_2 increased its photocatalytic power and in addition increased feasibility to work under visible light illumination (green laser), which composes approximately half of the solar spectrum.[148] In addition, the use of visible light illumination is less dangerous to human health than the UV[187] which makes it a safer system to the user.

3.3.3 Flow rate optimization

In electroanalysis, mass transport is one of the advantages of FIA systems as it improves the sensitivity of the method, although it can be affected by the flow rate.[121] Therefore, the flow rate was studied in a range from 0.25 to 1.5 mL/min by analyzing the photocurrent of 0.15 µM HQ (Fig. S3.8). The amperometric responses remained almost constant, with no significant difference between different values of flow rate. Thereby, to prevent wasting a large amount of sample and to secure a fast analysis time, a value of 1.0 mL min^{-1} was selected as the optimum flow rate.

3.3.4 Working potential and pH optimization

The influence of the working potential on the photocurrent response of a buffer solution containing 0.15 µM HQ was carried out in a potential range from 0.3 to -0.3 V (Fig. 3.7). Applying positive potentials, the observed photocurrent response is minimal when compared to the responses obtained for negative potentials. Another important observation is that the photocurrent and the baseline (background current), as well as the standard deviation of the responses increase when the working applied potential shifts in the cathodic direction (< -0.2 V) due to the influencing of competing reactions (*e.g.* oxygen reduction).[78, 122] Therefore, an optimal amperometric response, which combines a greater photocurrent response for HQ detection with low standard deviation, was obtained when a negative potential of -0.14 V vs Ag quasi-reference electrode of the SPE was applied. This potential was chosen as an optimal working potential.

Figure 3.7 - Influence of the working potential on the photocurrent response of 0.15 µM HQ at SPE|AuNPs@TiO$_2$ in 10 mM PBS containing 0.1 M KCl (pH 7.0) (n = 3), using a flow rate of 1 mL/min.

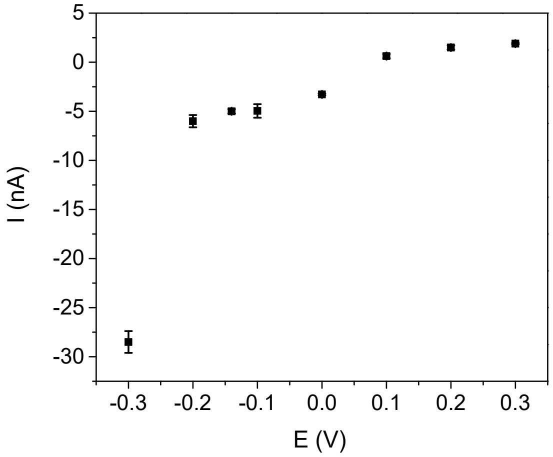

Source: Mendonça *et al.*, 2021.

The influence of pH on the amperometric response of 1.0 µM HQ at SPE|AuNPs@TiO$_2$ was studied in the pH range of 5.0 – 8.0 (Fig. 3.8). The increase in the photocurrent response is observed by increasing the pH value until it reaches neutral pH and then the photocurrent response decreases, at pH 8.0. This behavior is expected due to the protonation of HQ at a more acid pH range (pH < 7.0) and the gradual deprotonation while the pH is increasing from pH 5.1 until 7.1, where it reaches the maximum value of photocurrent response.[123, 124] At higher pH, there is a partial reduction of protons participation in the electrochemical reaction and then a reduction on amperometric response is observed.[123] Therefore, pH 7.0 was chosen as the optimal pH for further measurements.

Figure 3.8 - Influence of pH on the photocurrent response of 0.15 µM HQ at SPE|AuNPs@TiO$_2$ in 10 mM PBS containing 0.1 M KCl, using a working potential of -0.14 V vs Ag quasi-reference electrode (n = 3) and flow rate of 1 mL/min.

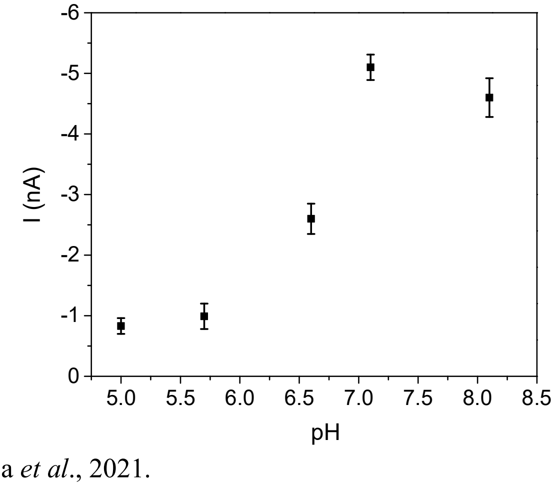

Source: Mendonça *et al.*, 2021.

3.3.5 Applicability of SPE|AuNPs@TiO2 modified electrode

The applicability of the SPE|AuNPs@TiO2 sensor under green laser illumination was evaluated for the quantification of 4-AP. The calibration curve from Figure 3.9 displays a characteristic behavior of photocurrent response with increasing 4-AP concentrations. The linear correlation between amperometric response and different concentrations of 4-AP in the range from 0.0125 – 0.5 μM is shown (Fig. 3.9 inset). The LOD calculated was 17 nM, confirming the applicability of the sensor for the detection of 4-AP.

Figure 3.9 - Calibration plot for 4-AP in 10 mM PBS containing 0.1 M KCl (pH 7.0), using SPE|AuNPs@TiO2 under green light illumination and applied potential of -0.14 V vs Ag quasi-reference electrode (n = 3). Inset: Linear curve in the concentration range from 0.0125 to 0.5 μM.

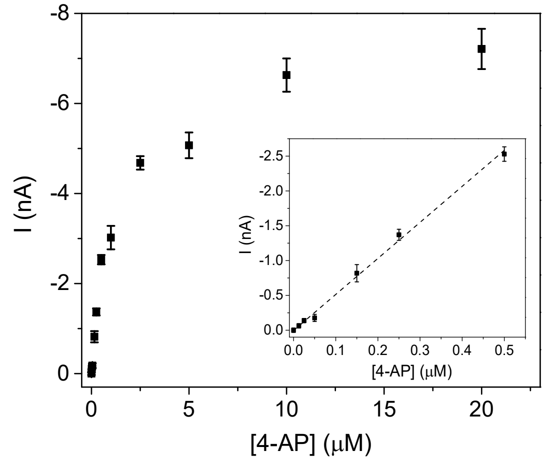

Source: Mendonça *et al.*, 2021.

3.3.6 Interference study for HQ

In order to validate the proposed photosensor with respect to selectivity, an interference study was conducted for 1.0 μM HQ detection at AuNPs@TiO2 photosensor in the presence of phenol (Ph), 4-nitrophenol (4-NP), bisphenol A (BPA), 3-nitrophenol (3-NP), 2-aminophenol (2-AP) and 3-aminophenol (3-AP), considering as possible interfering compounds, as they can coexist in the same environment as the HQ. An increase by 3.7%, 1.5%, 2.6%, 1.4%, 3.3% and 4.8% on the amperometric response of HQ in the presence of Ph, 4-NP, BPA, 3-NP, 2-AP and 3-AP, respectively, was observed (Fig. S3.9). The position of functional groups and the tendency of some substituents on the aromatic ring to form electron-donor conjugation can explain the predisposition of reactivity from some phenolic structures, such as HQ.[79, 188] Moreover, the presence of multiple hydroxyl groups provides a strong activating effect to the

HQ molecule, meaning higher interacting power with the electrode surface.[189] Therefore, the amperometric responses of 10-fold concentrations of the measured phenolic compounds showed no significant influence on the detection of 1.0 µM HQ, confirming the selectivity of the sensor for detecting HQ in the presence of such phenolic molecules.

3.3.7 Real sample analysis

The optimized photosensor was applied for the detection of HQ and 4-AP in an effluent water sample. The water sample from Aquafin RWZI was analyzed. The accuracy of the proposed method was reported as the percentage of recovery of a given known value of concentration added to the real sample to be analyzed (Table 3.1). In detail, standard additions to the water sample were performed in three different levels of fortifications (low, mid and high) for HQ (0.01, 0.08 and 0.12 µM) and 4-AP (0.1, 0.2 and 0.35 µM), each replicated 3 times (means n = 9 each organic molecule) and, subsequently, analyzing them by using the AuNPs@TiO_2-based photoelectrochemical sensing platform. The average recovery percentages were obtained in a range of 91.4% to 102.5% for 4-AP and 90.0% to 105.6% for HQ. The recovery acceptance criteria was set as 70 - 110%.[190, 191] Therefore, the results confirm the ability of the proposed sensor for the determination of such phenolic molecules in complex samples.

Table 3.1 - Recovery results of HQ and 4-AP quantification in effluent sample

Sample	**HQ**			**4-AP**		
	Spiked (µM)	**Detected (µM ± SD*)**	**Recovered (%)**	**Spiked (µM)**	**Detected (µM ± SD*)**	**Recovered (%)**
Effluent	0.01	0.009 ± 0.002	90.0	0.10	0.091 ± 0.012	91.4
	0.08	0.084 ± 0.003	105.6	0.20	0.189 ± 0.024	94.5
	0.12	0.109 ± 0.015	91.2	0.35	0.359 ± 0.026	102.5

* Triplicate determination per each concentration, n = 3.

Source: Mendonça *et al.*, 2021.

3.4 CONCLUSIONS

A novel photoelectrochemical sensing approach was successfully applied for the sensitive detection of HQ and 4-AP under visible light illumination based on the impregnation of size-controlled AuNPs on an anatase TiO_2 structure (AuNPs@TiO_2). The setup is integrated in a flow injection system to avoid the electrode poisoning during electroanalysis by means of periodic washing steps of the electrode surface. The AuNPs@TiO_2 photocatalyst was successfully obtained by a photo-assisted synthesis and later characterized by using XRD, Raman spectroscopy, SEM, EDX, TEM, UV-DR, EIS and LSV analysis. The homogeneous distribution of AuNPs over the TiO_2 structure was confirmed by the morphological characterization. An enhancement in the photocatalytic activity of TiO_2 was verified by using an AuNPs loading of 3.0 wt.%. The improved photocatalytic activity is ascribed to the SPR effect and charge transfer property of AuNPs. The FIA system played an important role on the sensitivity of the method to detect HQ and 4-AP at nM-level within minutes. In addition, the good repeatability and precision of the sensor is ascribed to the stability of the plasmonic catalyst (AuNPs@TiO_2) on the graphite SPE electrode surface. The efficiency and accuracy of the proposed photosensor were demonstrated by sensing HQ and 4-AP in effluent water collected from sewage treatment plant, suggesting a great potential of the photoelectrochemical-based flow injection strategy for monitoring water quality. Moreover, the application of the plasmonic photocatalyst can also be extended for photodegradation studies of organic molecules in several environmental remediation strategies.

CHAPTER 4

Influence of annealing treatment on the properties of electrochemically synthesized ZnO nanorods

In this chapter, the effect of the annealing temperature on the crystallinity of ZnO nanorods was investigated. Vertically aligned ZnO nanorods were successfully electrochemically synthesized on the fluorine-doped tin oxide (FTO) substrate without the presence of the seed layer. The post-growth surface annealing process of ZnO nanorods was performed at atmospheric pressure in the temperature range of 200 to 500 °C. The ZnO nanorods were characterized by UV-DR spectroscopy, X-ray diffraction (XRD), scanning electron microscope (SEM), X-ray photoelectron spectroscopy (XPS), Raman spectroscopy and electrochemical techniques (chronoamperometry and linear sweep voltammetry). In agreement with Raman and XPS results, the XRD data showed that by increasing the annealing temperature up to 350 ºC an increase in crystallite size and, consequently, in greater crystallinity, is observed. Increasing the annealing temperature up to 350 ºC resulted in a decrease of the band gap energy, showing excellent optical properties. The corresponding effect of the annealing temperature on the amperometric response of ZnO nanorods was also investigated. The strong influence of post-growth annealing treatment on the morphological, structural and optical properties of ZnO nanorods is duly shown. According to the presented results, the nano-sized ZnO showed suitable performance for future photovoltaic cells and PEC sensing applications.

This chapter is adapted from the article:

Study of the annealing effect on the crystallinity of ZnO nanorods synthesized by a straightforward electrodeposition method. Submitted.

4.1 INTRODUCTION

Semiconductor nanomaterials have attracted interest of the scientific community due to their properties and characteristics that allow the application of these materials in several fields. One of the most studied semiconductors is zinc oxide (ZnO) which is a promising candidate for the construction of accurate devices to quantify organic molecules[192-194] and for photocatalysis purposes.[195-197] Additionally, it is employed for the development of optoelectronics devices[198, 199], supercapacitors[200, 201] and photovoltaic cells.[202, 203] The wide application of ZnO photocatalysts is associated with its chemical and thermal stability, optical, electronic, magnetic and piezoelectric properties, as it is non-toxic, biocompatible, easily synthesized and cost-effective.[42, 204]

ZnO is an n-type semiconductor with a wide direct band gap energy (3.37 eV) and high exciton binding energy.[42] Depending on the method of synthesis used, it is possible to obtain crystalline ZnO structures with unique size-related optical, electrical and magnetic properties.[205] Several ZnO structures have been reported in the literature, such as nanohelices[206], spherical[207], lamellar[208], nanorods[209-211], nanowires[212, 213] and nanobelts.[214] The structure mainly depends on the synthesis protocol: sol-gel method[209, 215, 216], hydrothermal deposition[217-219], spray-pyrolysis[220] or electrodeposition.[221, 222] Among them, electrodeposition is one of the most attractive methods since it is a low cost, fast and efficient synthesis protocol operational at low temperature, ensuring an uniform deposition.[220, 222, 223] It is a known fact that the presence of oxygen vacancy defects in the ZnO structure are responsible for significantly improving its optical absorption and photogenerated charge separation, as well as reducing its band-gap.[204] This characteristic can be achieved by varying the electrodeposition synthesis parameters, such as precursor and its concentration, pH, electrodeposition time and applied potential.[205]

Several strategies have been developed to enhance the optical-electronic and conductive properties of these ZnO structures, associated to the changes originating from physical-chemical processes, such as annealing treatment of the ZnO surface[204, 220, 224, 225] and by doping or modification.[226, 227] Indeed, the temperature variation during annealing treatments can influence the presence of oxygen vacancies commonly found in ZnO structures and therefore its crystallinity, allowing their improved performances in many applications.[204]

In this work, the successful growth of ZnO nanorods vertically aligned to the fluorine-doped tin oxide (FTO) coated glass substrate was achieved by using a straightforward electrodeposition method at low temperature and without the use of catalysts or seed layer. The study of the annealing effect on the crystallinity and on photocatalytic activity of the synthesized ZnO nanorods, using the temperature range of 200 to 500 ºC, is also detailed. The synthesis combined with the optimized growth conditions, as well as the surface annealing procedure were fundamental steps to achieve better photocatalytic properties of the size-controlled ZnO nanostructures. The obtained ZnO nanorods presented good stability, as well as excellent physicochemical properties and characteristics, suggesting a promising candidate for sensing or photocatalysis applications.

4.2 EXPERIMENTAL

4.2.1 Materials

Zinc nitrate hexahydrate ($Zn(NO_3)_2 \cdot 6H_2O$), potassium dihydrogen phosphate (KH_2PO_4) and potassium chloride (KCl) were obtained from Sigma-Aldrich. Hydrogen peroxide (H_2O_2), potassium permanganate ($KMnO_4$) and ammonium hydroxide (NH_4OH) were purchased from Synth. Acetone was obtained from Panreac and isopropyl alcohol from Qhemis. A phosphate buffer solution (PBS) prepared using 10 mM KH_2PO_4 containing 0.1 M KCl was used as the supporting electrolyte for amperometric measurements. Concentrated NaOH solution was used to adjust the pH of the buffer solution to 7.0. The deionized water with resistivity of 18.2 MΩ cm^2, purified by Barnstead Nanopure System (Thermo Scientific, USA), was used to prepare the solutions. FTO glass with 0.5 cm^2 of geometric area and surface resistivity of 7 Ω/sq, was purchased from Sigma-Aldrich®. All analytical grade reagents were used without further purification.

4.2.2 Apparatus

The electrodeposition and amperometric measurements were carried out using a Potentiostat/Galvanostat Autolab®/PGSTAT128N, controlled by NOVA software (version 2.1.4). A home-made thermostatic electrochemical cell with a volume of 10 mL and cover made of polytetrafluoroethylene (PTFE) was used for the ZnO electrodeposition (Fig. S4.1). During the synthesis step, the electrodes of Ag/AgCl (3 M KCl), platinum wire and FTO substrate were used as the reference, counter and working electrodes, respectively. A thermostatic bath controlled by a microprocessor (model MPC-208B) purchased from Huber was used to keep the temperature solution at 80 ºC during the ZnO synthesis.

PEC measurements were carried out using a home-made quartz window electrochemical cell with a single compartment with capacity of 7.0 mL and three electrodes inputs (Fig. S4.1).

A black UV light ($\lambda \leq 400$ nm) with 20 W of power was used as a source of electron generation from ZnO. The synthesis and all electrochemical measurements were performed in a Faraday cage.

4.2.3 Synthesis of ZnO on FTO glass

The FTO glass was previously subjected to a cleaning step to remove organic impurities and possible metallic contaminants coming from its industrial synthesis, as follow[228]: the plates were rinsed with water and then taken to an ultrasonic bath first using water, followed by ethanol, acetone and then isopropyl alcohol, for 5 min in each solvent. After that, the plates were immersed in a solution containing 0.5 M $KMnO_4$ for 1 h and, then, washed with H_2O_2 (v/v, 30%) and deionized water. In order to ensure the adhesion of ZnO nanorods film to FTO surface, a hydrophilization treatment was carried out by immersing the FTO plates in a solution containing H_2O_2:NH_4OH:H_2O (ratio 1:1:5) during 1 hour, at 70 ºC. Finally, they were rinsed with deionized water and dried under the N_2 stream. The cleaned and hydrophilized FTO plates were ready for the ZnO synthesis step.

The electrodeposition synthesis of ZnO nanorods on FTO substrate was carried out using a solution of 0.0025 M $Zn(NO_3)_2 \cdot 6H_2O$, at 80 ºC and applying a cathodic potential of -1.0 V (*vs* Ag/AgCl) for 30 minutes, using the chronoamperometric technique.[229] After obtaining a homogeneous and uniform film of ZnO nanorods, its surface received the annealing treatment at temperatures of 200 ºC, 250 ºC, 300 ºC, 350 ºC, 400 ºC and 500 ºC for 1 h in an oven and at atmospheric pressure, in order to study the effect of annealing treatment on the crystallinity of ZnO nanostructures.

4.2.4 Characterization

The surface morphology of ZnO nanorods electrodeposited on FTO were characterized by scanning electron microscopy (SEM, model LEO-440 - Leica-Zeiss) equipped with an energy-dispersive X-ray spectroscopy (EDX, model 7060 - OXFORD). In order to analyze the crystallinity of ZnO nanorods, X-ray diffraction (XRD) measurements were performed using a X-ray diffractometer purchased from Bruker (model D8 Advance), with Cu K_α radiation source (λ = 1.5418 Å). Raman measurements were performed using Renishaw InVIA confocal scanning spectrometer and LabRam HR UV-Visible-NIR (200-2100 nm). Raman spectra were acquired during 15 seconds and with 2 accumulations, in the range of 50 to 1400 wavenumbers (cm^{-1}) and using an excitation source of 532 nm.

The band gap energy of ZnO was calculated from the results obtained by diffuse reflectance analysis and its optical absorbance was verified, using a UV-DRS spectrophotometer (model V-630, Jasco). Chronoamperometric and linear sweep voltammetry (LSV) measurements, with a potential step of 0.5 mV, scan rate of 5 mVs^{-1} and a potential range from 0.6 to -0.4 V, were performed in order to evaluate the photocurrent transient behavior.

In order to quantitatively identify the chemical composition of the ZnO nanostructures, the film electrodeposited on FTO surface were analyzed by X-ray photoelectron spectroscopy (XPS) using a spectrophotometer Scientia Omicron ESCA+ equipped with monochromatic Al Kα X-ray source (hν = 1486.6 eV).

4.3 RESULTS AND DISCUSSIONS

4.3.1 Morphological characterization

The effect of annealing treatment on the crystallinity of ZnO nanorods was studied in order to investigate the structural, morphological, optical and electrical behavior of the synthesized material. The annealing treatment was carried out at 200 ºC, 300 ºC, 350 ºC, 400 ºC and 500 ºC, for 1 hour in an oven at atmospheric pressure, later the nanorod films were analyzed by XRD and Raman (Fig. 4.1 and Fig. 4.2).

Figure 4.1 - XRD patterns of ZnO nanorods as grown and annealed at 200 ºC, 300 ºC, 350 ºC, 400 ºC and 500 ºC plotted in the range of 2θ (a) from 15º to 75º and (b) from 30º to 37º (normalized according to the crystallographic plane (100)).

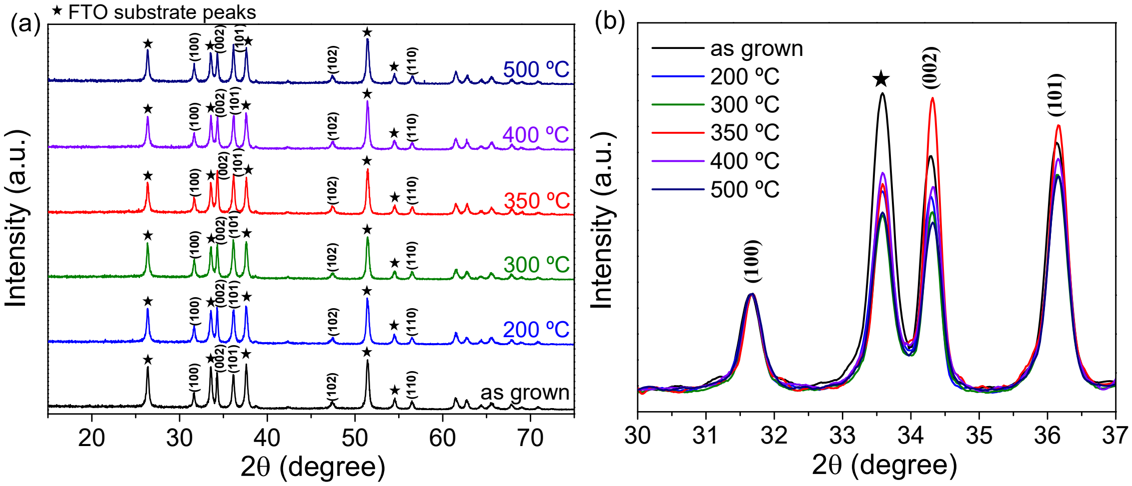

Source: Own authorship.

The XRD patterns from Figure 4.1a show characteristic diffraction peaks of ZnO, which correspond to its standard crystallographic primer (JCPDS Card nº 067454). The crystallographic planes of ZnO and their respective positions are detailed in Table S4.1. The remaining peaks are assigned to the FTO substrate. The prominent peaks at 31.66, 34.28 and 36.13 assigned to the crystallographic planes (100), (002) and (101), respectively, are attributed to the hexagonal wurtzite structure of ZnO crystals (Fig. 4.1b). The crystallographic plane (002) is characteristic of nanorods growth preferably along the c-axis orientation perpendicular to the substrate. The increase in the intensity of the diffraction peak with the increasing temperature for the crystallographic plane (002) is remarkable until reaching the annealed temperature at 350 ºC. This characteristic also leads to an increase of crystallite size and hence an increase of crystallinity.[230]

The crystallite size was calculated from the full width at half maximum (FWHM) of the most intense plane corresponding to ZnO from each diffractogram by using the Scherrer equation.[231] Therefore, the (002) plane was selected to calculate the structural parameters of the ZnO annealed at different temperatures and the results are shown in Table 4.1. The crystallite size ranged from 28.34 to 32.76 nm and the ZnO annealed at 350 ºC showed lower FMHM and larger crystallite size indicating, in this sense, greater crystallinity. The values of the lattice parameters remained constant and are in good agreement with the JCPDS data for the wurtzite structure.

Table 4.1 - Effect of annealing treatment on the structural parameters of ZnO

Annealing temperature (ºC)	**FWHM (º)**	**Peak intensity (a.u)**	**2θ**	**Crystallite size (nm)**	**Lattice parameters**	
					a (Å)	**c (Å)**
as grown	0.31	370.37	34.29	30.09	3.02	5.23
200	0.30	368.17	34.28	30.69	3.02	5.23
300	0.29	386.80	34.31	31.21	3.02	5.22
350	0.28	513.48	34.32	32.76	3.01	5.22
400	0.32	348.36	34.34	28.78	3.01	5.22
500	0.33	288.92	34.31	28.34	3.02	5.22

Source: Own authorship.

Figure 4.2 shows the Raman spectra of ZnO nanorod films before and after annealing treatment at different temperatures and the FTO spectrum as a reference. The broad spectrum peaks present in all samples at 120, 242, 295, 556, 631 and 1097 cm^{-1} refer to the FTO substrate

(Fig. 4.2a). The dominant peaks at 99 cm^{-1} (low-E$_2$) and 434 cm^{-1} (high-E$_2$) are assigned to the ZnO wurtzite structures (Fig. 4.2b), which is also confirmed by XRD results. As observed for the ZnO diffraction peaks from the XRD patterns (Fig. 4.1b), the intensity of the E$_2$ (high) peak from the normalized Raman spectra of ZnO significantly increases with the increasing of the annealing temperature (Fig. 4.2b), which again indicates that the crystallinity is improved with annealing temperature until it reaches 350 ºC. XRD and Raman plots are represented using the same criteria (Fig. 4.1b and Fig. 4.2b). Since the ZnO annealed at 350 ºC demonstrated higher crystallinity, only the mentioned film and the ZnO as grown were conducted to the subsequent surface characterization analyses.

Figure 4.2 - (a) Raman spectra of FTO substrate, ZnO as grown and annealed at 200 ºC, 300 ºC, 350 ºC, 400 ºC and 500 ºC; (b) prominent Raman peaks (low-E$_2$ and high-E$_2$) magnified (normalized according to the band at 295 cm^{-1}).

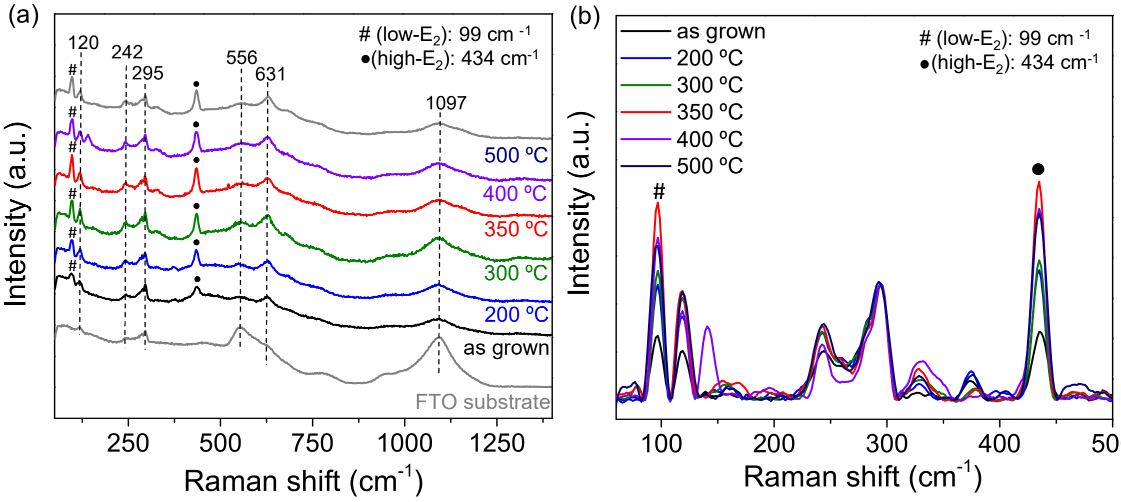

Source: Own authorship.

Figure 4.3 presents the SEM micrographs of ZnO as grown and annealed at 350 ºC. The formation of nanometric structures is observed and the typical morphology suggests these structures with a hexagonal shape are preferably perpendicular to the substrate (Fig. 4.3a). After being exposed to an annealing treatment at 350 ºC, the ZnO nanostructures were preserved, although the crystallite size increased (Fig. 4.3b).[232] Excellent coverage and adhesion to the FTO substrate by the ZnO nanostructures can also be verified from the corresponding micrographs.

Figure 4.3 - SEM images of ZnO nanorods (a) as grown and (b) annealed at 350 ºC. SEM magnification: 50,000x.

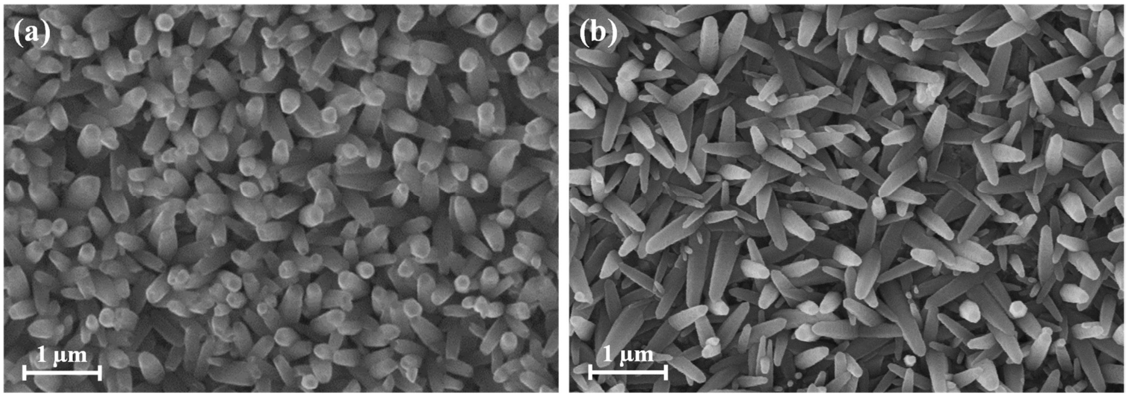

Source: Own authorship.

In order to semi-quantitatively characterize the nanostructures, EDX analyses of the top surface of ZnO were performed. Figure S4.2 shows the EDX spectrum of ZnO as grown and the peaks of Zn and O are distinguishable, as well as the Sn and Si signal from the FTO substrate. The analysis of the top surface of ZnO electrodeposited on the FTO substrate showed an average atomic percentage of 51% of Zn and 49% of O (analyzed area: 0.26 mm^2), suggesting an approximate 1:1 stoichiometric ratio between atoms.

The chemical state of the elements and the presence of possible impurities in the ZnO nanorods as grown and annealed at 350 ºC films were verified by XPS measurements. From the XPS survey spectra (Fig. 4.4), the presence of Zn (Zn 3d at 9.3 eV; Zn 3p at 87.4 eV; Zn 3s at 138.6 eV and Zn 2p at 1020.5 and 1043.4 eV), C (C 1s at 283.2 eV) and O (O 1s at 530.3 eV) elements is confirmed in both ZnO nanorod films. The appearance of the C element-related signal originates from a small contribution of atmospheric CO_2 (C adventium), which usually occurs in samples when exposed to the air.[213, 233] The presence of oxygen corresponds mainly to the signal coming from ZnO and a minor part coming from atmospheric oxygen.[234] Therefore, no impurities were found in the ZnO nanorod films as grown and annealed at 350 ºC.

Figure 4.4 - XPS spectra of ZnO as grown and annealed at 350 ºC, synthesized on FTO substrate.

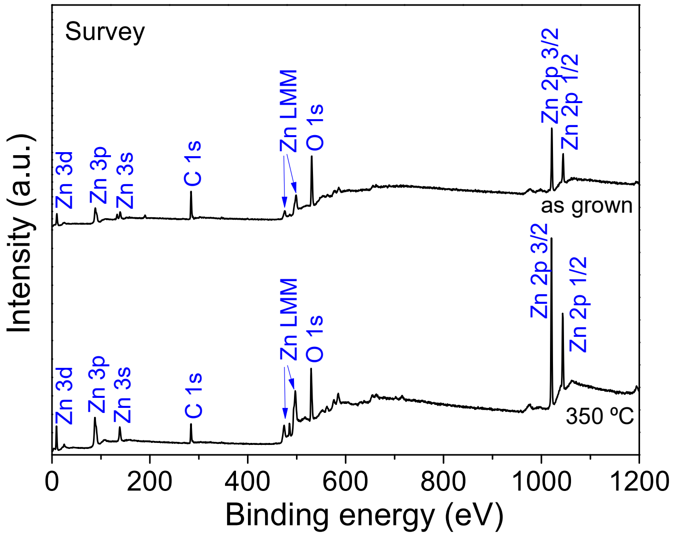

Source: Own authorship.

The XPS technique was also used in order to evaluate the variation in the composition of O (O 1s) bonds present in the ZnO nanorod films before (as grown) and after annealing treatment at 350 ºC (Fig. 4.5). The O 1s peaks (in red) shown in Figure 4.5a,b were separated into Gaussian components that represent the presence of three different oxygen states, namely: oxygen attributed to -O-Zn bonds (in blue); oxygen associated to O^{2-} (-O-deficient) ions in the oxygen vacancy regions of the ZnO crystal structure (in green); and chemically adsorbed oxygen or hydroxyl groups present on the surface of ZnO (-O-surface) (in violet).[235] After annealing treatment, a significant decrease in the proportion of -O-Zn groups and an increase of -O-deficient and -O-surface groups is observed (Fig. 4.5b). An increase of oxygen vacancies (-O-deficient groups) promotes an increase in the concentration of electron carriers and a consequent decrease in the Fermi level of the ZnO towards its valence band.[234] As a result, the electrical properties of ZnO can be greatly improved[225], which will be discussed in the electrochemical characterization section. The percentage variation composition of oxygen for both films can be checked in Figure 4.5c.

Figure 4.5 - O 1s XPS spectra of (a) ZnO as grown, (b) ZnO annealed at 350 ºC (peak finding method: local maximum) and (c) percentual area of the groups -O-Zn, -O-deficient and -O-surface at the related temperatures.

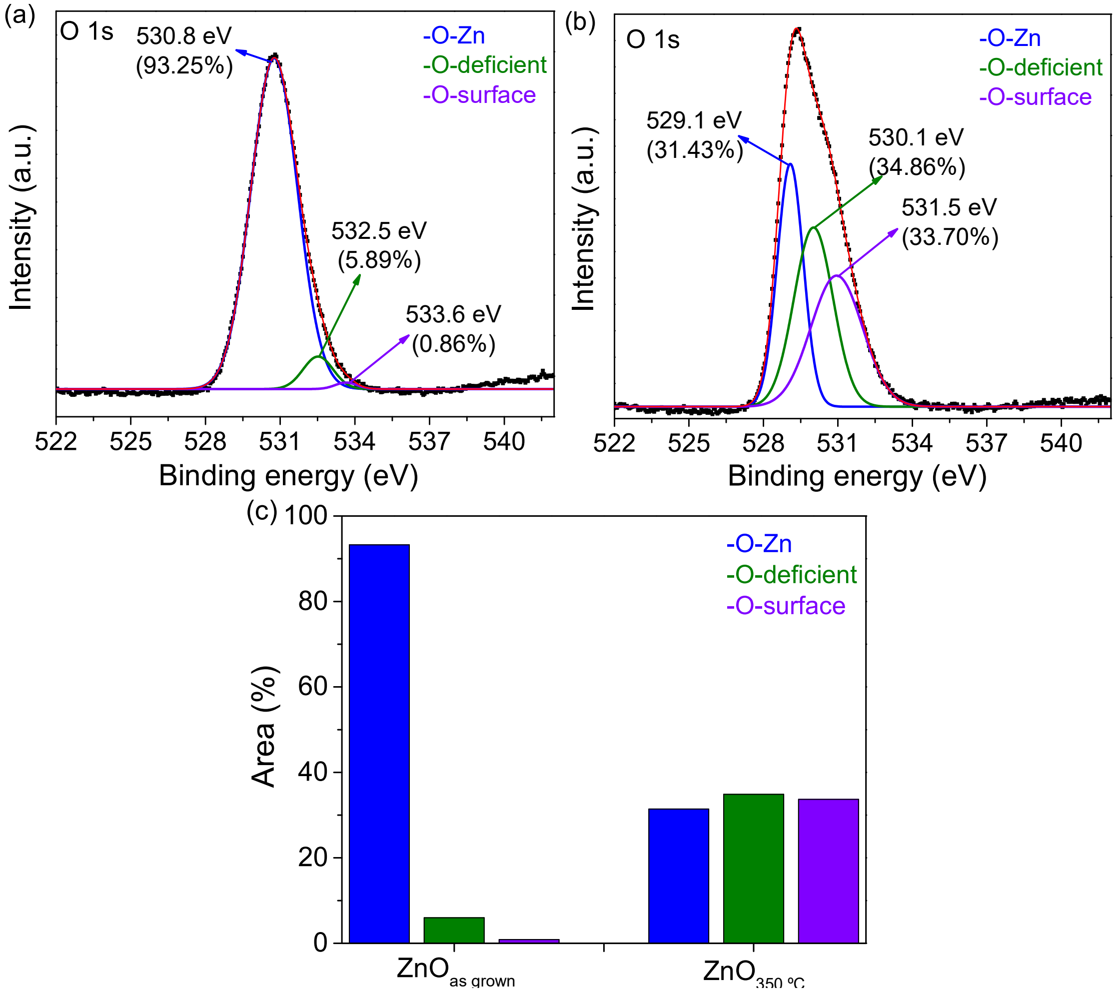

Source: Own authorship.

4.3.2 Electrochemical characterization

The photocurrent transient behavior of ZnO nanorod films as grown and annealed over the temperature range of 200 to 500 ºC was evaluated by linear sweep voltammetry (LSV) and chronoamperometric measurements under chopped-light illumination (Fig. 4.6). Linear sweep voltammograms were collected over a potential range from 0.6 to -0.4 V in a PBS buffer solution. The photocurrent response for each ZnO nanorod film varied with respect to the annealing temperature and the applied potential. When the applied potential moves towards more negative values, the photocurrent response decreases dramatically (Fig. 4.6a). Minimal or no photocurrent response is observed at potentials below -0.2 V. At more positive potentials, the contribution from water-splitting in the photocurrent response of ZnO is observed, suggesting the potential use of the synthesized material as a photoanode in PEC applications.[236] Additionally, the ZnO nanorod film annealed at 350 ºC exhibited high photocurrent response and outperformed the other films.

Figure 4.6 - a) Linear sweep voltammograms and (b) chronoamperometric responses for ZnO nanorod films as grown and annealed at 200 ºC, 300 ºC, 350 ºC, 400 ºC and 500 ºC, applied potential of 0.2 V under chopped light illumination in 0.01 M PBS (pH 7.0).

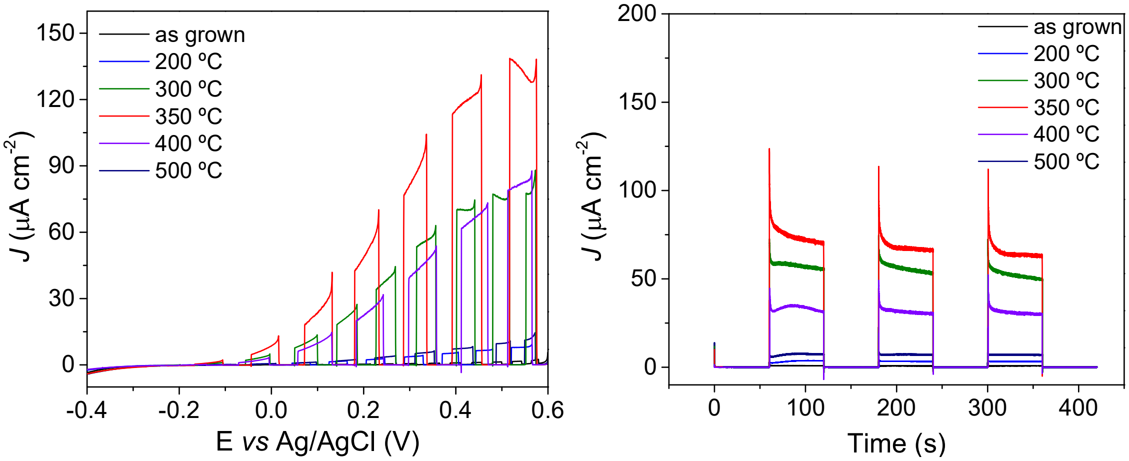

Note: The light incidence and non-incidence interval was 60 s and the applied potential of 0.2 V was used during the chronoamperometric measurements. Source: Own authorship.

Similarly as observed from the LSV results, there is a significant variation on the amperometric response with increasing annealing temperature performed on the films and a short stabilization time of the photocurrent is verified. This phenomenon is due to the fact that the electron-hole recombination is suppressed in the dark and under the incidence of light, demonstrating the good electronic performance of the synthesized film.[43, 237] The average amperometric response and the standard deviation results for each film are shown in Table S4.2. A 94-fold increase in the average photocurrent intensity (67×10^{-6} A cm^{-2}) is observed for the ZnO nanorod film that received the annealing treatment at 350 ºC compared to the as grown film, which had the lowest average photocurrent response recorded (0.71×10^{-6} A cm^{-2}). From 350 °C to 500 ºC the photocurrent response begins to decrease, and for the ZnO nanorod film annealed at 400 °C it decreases to approximately half of the value (Fig. 4.6b). The expressive variation on the photocurrent response with increasing annealing temperature is associated with the structural modifications occurring in the crystal of ZnO nanorods, which significantly change the optical and electronic properties of the film as a result.[224] Hence, the photocurrent results are consistent with the morphological characterization results obtained by DRX and Raman, confirming that, besides presenting greater crystallinity, the ZnO nanorod film annealed at 350 ºC also exhibits the highest amperometric performance compared to the other films studied.

4.3.3 Optical characterization

The improvement of optical properties of the ZnO nanorod film annealed at 350 ºC was verified by UV-VIS spectroscopy and compared to the optical response of the ZnO nanorod film as grown. The absorbance spectra and the plot obtained from the diffuse reflectance results are shown in Figgure 4.7. The absorbance of ZnO was slightly shifted to a higher wavelength region after annealing treatment (Fig. 4.7a). The band gap energy (E_g) of the films before and after annealing treatment was estimated using the Kubelka-Munk function and the Tauc plot.[238, 239] By extrapolating the linear portion of the curve from the $(\alpha h\upsilon)^2$ vs $h\upsilon$ plot to the point of intersection with the x-axis, where the energy absorption of ZnO is observed, the E_g was determined (Fig. 4.7b). The values of the obtained band gap energy was found to be 3.23 eV and 2.96 eV for the ZnO nanorod films as grown and annealed at 350 ºC, respectively. Therefore, the annealing treatment of the ZnO nanorods also provided a decrease in the band gap energy, which is associated with improved crystallinity and increased crystallite size, that result in a reduction of crystalline defects.[240] A lower E_g gives the material a rapid decrease in reflectance, since ZnO quickly absorbs energy if the incident photon has equal or higher energy than its E_g. As a result, an electron-hole pair is readily generated and a superior ZnO performance can be observed.[241]

Figure 4.7 - a) UV-Vis absorbance spectra of the bare FTO substrate; of ZnO as grown and annealed at 350 ºC, both electrodeposited on the FTO substrate. b) Tauc plot for the band gap energy determination of ZnO nanorod films as grown and annealed at 350 ºC.

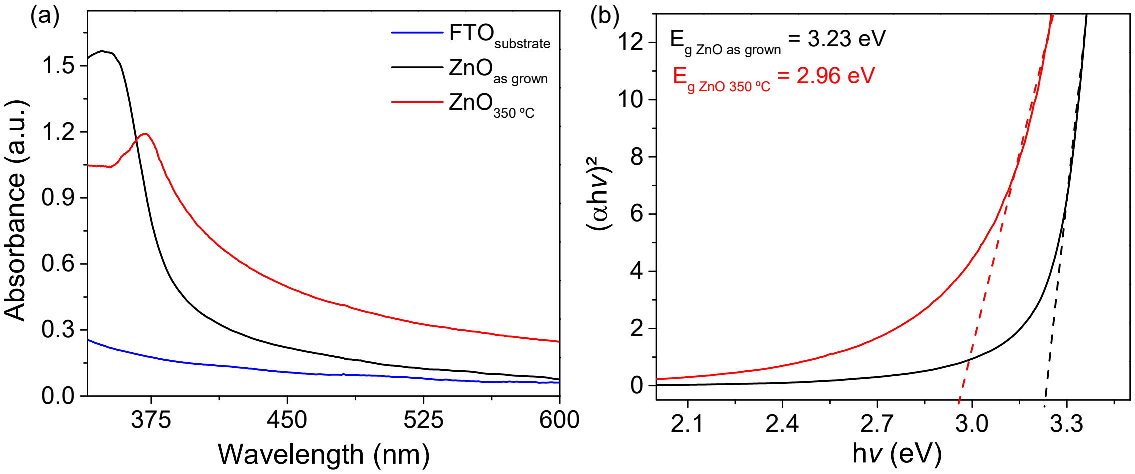

Source: Own authorship.

4.4 CONCLUSIONS

Well-aligned ZnO nanorods were successfully synthesized on the FTO substrate by using a facile electrodeposition method and without the need of the seed layer. The effect of the annealing treatment at 200 ºC, 300 ºC, 350 ºC, 400 ºC and 500 ºC on the crystallinity of the ZnO nanorods were investigated. The morphological, electrochemical and optical properties of the synthesized ZnO varied with increasing annealing temperature. The XRD spectra showed that the ZnO nanorods have hexagonal wurtzite structure and the film annealed at 350 ºC presented a maximum increase on its crystallinity, as well as a larger crystallite size. The enhanced crystallinity of the synthesized ZnO nanorods annealed at 350 ºC was also confirmed by the Raman spectra. The increase in the percentage of oxygen vacancies was verified from the XPS spectra that can be indirectly linked to the improved electrical properties of ZnO nanorod film annealed at 350 ºC. The improvement of electrical properties was confirmed later by amperometric measurements through the significant 94-fold increase in its average photocurrent response. The study of the optical characteristics of the ZnO nanorod films as grown and annealed at 350 ºC was carried out and a reduction from 3.23 eV to 2.96 eV on the band gap energy was observed. Therefore, 350 ºC was found to be the optimal annealing temperature due to better performance of ZnO. The synthesis of a homogeneous, uniform and nano-sized film combined to the annealing step proved to be a new insight for the improvement of the physicochemical properties of ZnO, which makes its use even more attractive in future applications, such as photovoltaic cells and PEC sensors.

CHAPTER 5

Photoelectrochemical monitoring of the 4-nitrophenol by using the amperometric sensor of ZnO nanorods electrodeposited on FTO substrate

This chapter describes the amperometric quantification of 4-nitrophenol (4-NP) by using nanostructured zinc oxide (ZnO) photosensor sensitized by perylene-3,4,9,10-tetracarboxylic acid (PTCA), under UV-A light illumination. The synthesized and annealed $ZnO_{350\,°C}$ nanorods from the previous chapter are modified with the photosensitizer PTCA. The PTCA is synthesized by hydrolysis/neutralization steps and is drop-casted onto $ZnO_{350\,°C}$ nanorods surface. The surface of $ZnO_{350°C}$ modified with PTCA ($ZnO_{350\,°C}$|PTCA) by Fourier transform infrared spectroscopy (FTIR), X-ray photoelectron spectroscopy (XPS), and UV-vis spectroscopy techniques are characterized to evaluate the interaction between the photosensitizer and the surface of the semiconductor-based material. The effect of the working potential, pH, and supporting electrolyte on the photocurrent response of the FTO-$ZnO_{350\,°C}$|PTCA photosensor in the presence of 4-NP is investigated. Under optimum conditions, the photosensor was used to quantify 4-NP, achieving a good linear correlation (0.993), with a detection limit of 0.09 nM and sensitivity of 0.51 A M^{-1} cm^{-2}. To validate the novel sensitive and low-cost photosensor for the detection of phenolic compounds, the traditional chromatographic detection of 4-NP is also performed in our study.

This chapter is adapted from:

Photoelectrochemical sensing of 4-NP based on nanostructured ZnO sensitized by carboxylated perylene. In preparation.

5.1 INTRODUCTION

The monitoring of toxic organic compounds in the environment is the main objective of many works that involve the development of analytical detection devices.[242, 243] The search for materials and methods that combine high selectivity and sensitivity, low cost, and portability, allowing in situ and real-time analysis is in constant development.[242, 244, 245] The development of semiconductors-based nanomaterials such as zinc oxide (ZnO) has been reported and has shown promising results as a photosensor.[193, 194, 246]

Several methods have been described in the literature for the synthesis of ZnO nanostructures.[215, 217, 220, 221] One of the most widely used methods is electrodeposition, which has a simple and fast synthesis protocol and provides a thin and uniform film.[229] The reactions that take place during obtaining nanostructured ZnO using electrodeposition synthesis and $Zn(NO_3)_2$ as a precursor are explained by the chemical equations below[247]:

$$Zn(NO_3)_2 \rightarrow Zn^{2+} + 2NO_3^- \qquad (1)$$

$$NO_3^- + H_2O + 2e^- \rightarrow NO_2^- + 2OH^- \qquad (2)$$

$$Zn^{2+} + 2OH^- \rightarrow Zn(OH)_2 \qquad (3)$$

$$Zn(OH)_2 \rightarrow ZnO + H_2O \qquad (4)$$

In an aqueous solution, the $Zn(NO_3)_2$ dissociates and generates Zn^{2+} and NO^{-3} ions (Reaction 1). Under negative potential, the nitrate ions are reduced generating nitrite and hydroxide ions (Reaction 2). Subsequently, Zn^{2+} ions react with the available hydroxide ions, generating $Zn(OH)_2$ (Reaction 3). Finally, the ZnO is precipitated at the surface of a substrate (Reaction 4).

The wide band gap of ZnO limits its absorption in the UV region and consequently influences its photoelectronic response. The low conductivity observed for the semiconductors also influences the low electronic transfer. To overcome these disadvantages and to enlarge its photoabsorption in the near-visible range, some strategies have been studied aiming to improve the optical and electronic properties of ZnO, such as the use of photosensitizers.[248-251] Photosensitizers act as an electron injector into the conduction band of the semiconductor-based material, contributing to its photoelectronic response. Under illumination, the photosensitizer absorbs enough energy to promote electrons from its high-occupied molecular orbital (HOMO) to the lowest unoccupied molecular orbital (LUMO). Subsequently, these electrons are readily transferred to the conduction band of the semiconductor.[59, 252] One of the known photosensitizers is 3,4,9,10-perylenetetracarboxylic acid (PTCA, Fig. 5.1). PTCA is a carboxylated organic molecule with a conjugated polyaromatic nucleus. Heterojunction of this molecule with the semiconductor-based material surface occurs by hydrogen bonds through active carboxyl groups.[59] PTCA can absorb over a wide range of the visible region, presenting advantages as a photosensitizer.[253] Moreover, this organic photosensitizer has high chemical stability on the surface of semiconductor materials.[254]

Figure 5.1 - Molecular structure of PTCA.

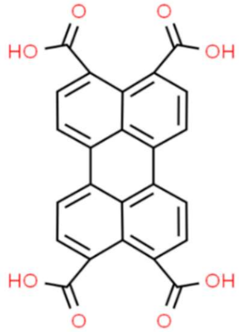

Source: ChemSpider.[255]

During the photoelectrochemical (PEC) process, the presence of organic electron receptor molecules can inhibit the photocurrent response. The reason is related to the difference in the energy level, through the transfer of electrons from the conduction band of the semiconductor to the LUMO orbital of the molecule. Therefore, the quantification of electron receptor molecules can be evaluated through the decrease of the photocurrent response.[63, 256, 257] Reversal electron flow occurs when the organic molecule in solution, e.g. 4-NP, has a higher energy level than the semiconductor material (Fig. 5.2) [258, 259].

Figure 5.2 - Graphical representation of the theoretical energy level diagram of PTCA, ZnO, FTO, and 4-NP.

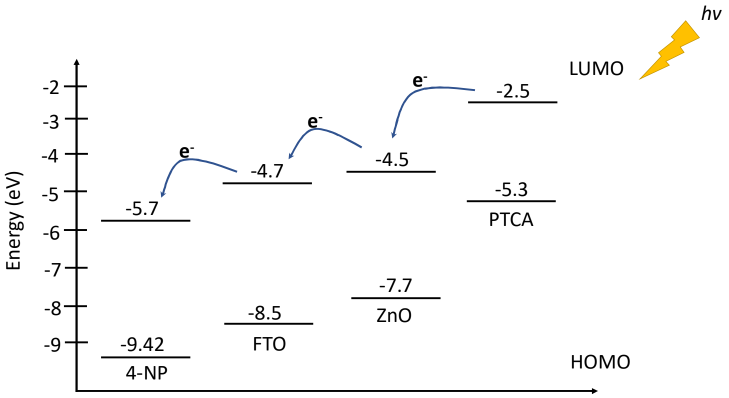

Source: Own authorship.

The compound 4-nitrophenol (4-NP), which is a phenolic compound widely used to manufacture dyes, drugs, and insecticides, has been analyzed via PEC processes.[260] 4-NP is the main degradation product of pesticides ethyl and methyl-parathion, being also classified as a toxic compound according to U.S. Environmental Protection Agency (U.S. EPA).[9] Based on the hazardous nature of 4-NP, public health concerns require accurate, real-time knowledge of 4-NP level in waters, soil, and food. One of the most widely used techniques to control and monitor toxic organic compounds is chromatographic technique. These techniques have high sensitivity, selectivity, and accuracy.[261]

In this chapter, a validation methodology is proposed to identify the influence of possible systematic and random errors assigned to the detection system.[262-264] According to Miller and Miller (2005), this comparison can be adequately conducted by plotting a graph where the detection results by a method to be validated, e.g. PEC, are set in the y-axis and the results obtained by the standard detection method of the compound analyzed, e.g. liquid chromatography, are added to the x-axis.[262] The product–moment correlation coefficient (R), the slope (b), and the intercept (a) of the regression line should be close to the ideal ($a = 0$, $b = R^2 = 1$) so that the obtained detection results by the two methods are considered analogous.[262] The paired *t*-test can also be used as a complementary tool to this comparative study and define whether the difference between the detection results is small enough to be explained by random errors or whether the values are completely different.[262, 265, 266] The calculated result is then compared to the critical *t* value, at 95% of confidence interval and $(n - 1)$ degrees of freedom, according to the number of concentrations (n) analyzed by each technique and for each sample.[262]

In this work, a novel photosensor is proposed based on the surface modification of the synthesized and annealed $ZnO_{350\ °C}$ nanorods with the photosensitizer PTCA (FTO-$ZnO_{350\ °C}$|PTCA) for the detection of 4-NP. The characterization study of the surface of $ZnO_{350\ °C}$|PTCA and the optimization of the experimental parameters, as well as the application of the proposed photosensor in natural and tap water are investigated. An optimized chromatographic method was used for the detection of 4-NP and the detection results were statistically compared with those obtained by PEC. Herein, the results show that the developed photosensor represents a breakthrough in the use of accurate PEC systems applicable to monitor 4-NP trace level in complex samples.

5.2 EXPERIMENTAL

5.2.1 Materials

4-nitrophenol (4-NP), zinc nitrate hexahydrate ($Zn(NO_3)_2 \cdot 6H_2O$), perylene-3,4,9,10-tetracarboxylic dianhydride (PTCDA), N,N-dimethylformamide (C_3H_7NO), potassium chloride (KCl), potassium hydroxide (KOH), and potassium dihydrogen phosphate (KH_2PO_4) were obtained from Sigma-Aldrich®. Ammonium hydroxide (NH_4OH), boric acid (H_3BO_3), phosphoric acid (H_3PO_4), and hydrogen peroxide (H_2O_2) were purchased from Synth. Isopropyl alcohol (C_3H_8O) and acetic acid (CH_3COOH) were obtained from Qhemis, and acetone from Panreac. Sodium hydroxide (NaOH) was purchased from Merck, sodium sulfate (Na_2SO_4) from J. T. Baker, and hydrochloric acid (HCl) from NEON. Deionized water with a resistivity of 18.2 MΩ cm^2 and purified by Barnstead Nanopure System (Thermo Scientific - USA) was used to prepare the solutions. Fluorine doped tin oxide coated glass (FTO) with surface resistivity of 7 Ω/sq and geometric area of 0.5 cm^2 was purchased from Sigma-Aldrich®.

Three supporting electrolytes were evaluated for amperometric measurements: Na_2SO_4 solution 0.2 M; phosphate buffer solution (PBS), prepared from KH_2PO_4 10 mM and KCl 0.1 mol L^{-1}; and the Britton-Robinson buffer solution (BR), prepared from the mixture of solutions of acetic acid, phosphoric acid and boric acid, which final concentration was 0.1 M. The pH of the supporting electrolyte solutions was adjusted with concentrated HCl and NaOH solutions.

5.2.2 Apparatus

An Autolab® (PGSTAT128N) potentiostat controlled by NOVA software (version 2.1.4) was used for electrochemical deposition of ZnO nanorods. PEC measurements were carried out using a PalmSens4 potentiostat (Utrecht, The Netherlands) with PSTrace software (version 5.8). A jacketed electrochemical cell made of borosilicate glass with a volume of 10 mL and with a cover made of polytetrafluoroethylene (PTFE) was used for the ZnO nanorods electrodeposition (Fig. S4.1a). During the synthesis, a platinum wire was used as a counter electrode, an Ag/AgCl (3 M KCl) electrode as a reference electrode, and the FTO substrate as a working electrode. A thermostatic bath purchased from Huber and controlled by a microprocessor (MPC-208B) was used to keep the temperature of the ZnO precursor solution at 80 ºC during the synthesis.

Amperometric measurements were carried out using a single-compartment quartz window PEC cell with a 7.0 mL capacity and three electrodes inputs (Fig. S4.1b). An UV-A light source ($\lambda \leq 400$ nm, 20 W) was used to drive the photocatalytic reactions. All electrochemical measurements were performed in a dark Faraday cage.

5.2.3 Synthesis of ZnO nanorods and sensitization by PTCA

Before the synthesis, the FTO glass was ultrasonically cleaned with deionized water, followed by ethanol, acetone, and then isopropyl alcohol, for 5 min in each solvent. A hydrophilization treatment of the FTO surface was performed for 1 hour, at 70 ºC using a solution containing H_2O_2:NH_4OH:H_2O (ratio 1:1:5, v/v). Then, the FTO glass was rinsed with deionized water and dried under N_2 gas stream.

The synthesis of ZnO nanorods on FTO glass was performed by a direct electrodeposition method, using a solution of 2.5 mM $Zn(NO_3)_2{\cdot}6H_2O$, at 80 ºC, and applying a cathodic potential of -1.0 V (*vs* Ag/AgCl) for 30 minutes.[229] The surface of homogeneous and uniform ZnO nanorods was subjected to an annealing treatment at 350 ºC in an oven, for 1 h, and at atmospheric pressure, to increase the crystallinity of the nanostructures.

The photosensitizer was prepared by dissolving perylene-3,4,9,10-tetracarboxylic dianhydride in an aqueous solution at 5% KOH, under stirring at 65 ºC. After cooling to room temperature, a solution of 0.1 M HCl was added drop by drop until pH 4.8 was reached. The precipitate was vacuum filtered. The obtaining red powder was named perylene tetracarboxylic acid (PTCA). The $ZnO_{350\ °C}$|PTCA heterojunction was obtained after dropping 10 µL of a suspension of 4 g L^{-1} PTCA dispersed in N,N-dimethylformamide (DMF) (4 g L^{-1}) onto the surface of ZnO nanorods and dried at room temperature.

5.2.4 Characterization

Diffuse reflectance and optical absorbance measurements of $ZnO_{350\ °C}$|PTCA were performed using a UV-DRS spectrophotometer (model V-630, Jasco). The diffuse reflectance results were used to calculate the band gap energy of $ZnO_{350\ °C}$|PTCA. Fourier-transform infrared spectroscopy (FTIR) analyses were carried out using a Bruker spectrophotometer (model ALPHA II). X-ray photoelectron spectroscopy (XPS) measurements were performed to quantitatively identify the chemical composition of the $ZnO_{350\ °C}$|PTCA heterojunction by using a Scientia Omicron ESCA+ spectrophotometer equipped with Al Kα monochromatic X-ray source (hν = 1486.6 eV).

5.2.5 Analytical procedure

Chronoamperometric measurements and linear sweep voltammetry (LSV) with a scan rate of 5 mVs^{-1}, a potential step of 0.5 mV in the range of 0.6 to -0.4 V were performed to evaluate the photocurrent transient behavior. The experimental parameters, such as the potential bias, supporting electrolyte, and pH, were optimized to improve the analytical response. All PEC measurements for quantification of 4-NP were conducted using the chronoamperometric technique, applying a working potential of 0.2 V (*vs* Ag/AgCl). Standard deviation studies were performed based on three measurements carried out for each experiment (n = 3).

The method developed by the United States Environmental Protection Agency (Method 555 U.S. EPA)[267] was adapted and used for the chromatographic detection of 4-NP. A Shimadzu HPLC-DAD (LC-10AD) with manual injector and UV detector (model SPD - 10 AV) was used. LabSolutions software (version 5.6) was used to process the results. A C18 reverse-phase column (25 cm x 4.6 mm ID x 5 µm particle) and a C18 pre-column (2 cm x 4 mm ID x 5 µm particle) both purchased from Sigma/Aldrich (Ascentis® Supelco) were used for the chromatographic separation of 4-NP. The following chromatographic parameters were used for analysis: injection volume of 20 µL, mobile phase composed of acetonitrile (A) and phosphoric acid (0.025 M) (B) in isocratic mode (60% A), run time of 7.5 min, flow rate of 1.0 mL/min and wavelength of 315 nm. The chromatographic analytical curve was obtained in the working range from 5.0 to 50 nM.

The LOD and the sensitivity for the PEC results were calculated from the equations: LOD = $3s_b/a$ and S = a/A, respectively (where s_b is the standard deviation of the blank; a is the slope from the calibration curve and A is the geometric area of the electrode). The LOD for the chromatographic results was estimated to be three times the average noise height of the blank.

The natural water samples were collected at the water treatment plant (WTP) of the Serviço Autônomo de Água e Esgoto (SAAE) originates from the Monjolinho River in São Carlos, São Paulo (Coordinates: 21º 59' 13.4"S 47º 52' 32.2"W). The natural water was cleaned up before chromatographic analysis. First filtered two or three times with qualitative filter paper, followed by filtration with a reconstituted cellulose filter membrane (0.45 µm porosity) and finally filtered with disposable syringe filters (0.20 µm porosity). For the PEC analysis, the natural water was subjected only to a qualitative filtering procedure to remove solid particles present in the sample.

The supply water was collected from a residence located in the city of São Carlos, São Paulo (Coordinates: 22º 01' 51.6"S 47º 52' 58.6"W). The tap water samples were also submitted to the clean-up step, as described for the natural water, for the chromatographic analyses. There was no need to filter the tap water samples for the PEC analyses.

Subsequently, the natural and tap water samples were buffered with the same salt composition used for the preparation of the PBS buffer solution, used in the PEC experiments. The samples were fortified with known amounts of 4-NP to obtain solutions in the concentration range from 0.5 to 50 nM, used in the PEC and chromatographic analyses.

5.2.6 Statistical study

The statistical comparison was performed to evaluate the performance of both methodologies for the detection of 4-NP in the same concentration range. The results of the analytical responses of water samples with known concentrations of 4-NP were statistically analyzed through the methodology that compares two analytical techniques, according to Miller and Miller.[262-264] Appling the paired *t*-test it was also possible to determine if the results are statistically equivalent, by using the equation $t = (d_M\sqrt{n})/SD$ (where d_M is the arithmetic average of the differences between each concentration value obtained for each methodology and each analyzed sample; n is the number of concentrations analyzed by each technique and SD is the standard deviation).[262]

5.3 RESULTS AND DISCUSSIONS

5.3.1 Influence of PTCA concentration

The effect of PTCA concentration on the amperometric response of FTO-ZnO$_{350\ °C}$ in 10 mM PBS solution and applied potential of 0.2 V (*vs* Ag/AgCl) is investigated over a concentration range from 2.3 to 37.4 mM. Figure S5.1 shows a significant increase in the amperometric response of the FTO-ZnO$_{350\ °C}$ sensor when modified with PTCA at the concentration from 2.3 to 9.3 mM, followed by a subsequent decay of the photocurrent response for the concentrations 18.7 and 37.4 mM. This behavior suggests that the amount of PTCA at the concentration of 2.3 mM has no significant influence on the photocurrent response of the semiconductor. On the other hand, when the concentration exceeds 18.7 mM, the PTCA immobilized at the surface of ZnO acts as a barrier, hindering the absorption of photons from the light for the charges generation in the semiconductor, thus reducing the photocurrent response. Therefore, 9.3 mM was chosen as the optimum PTCA concentration for the immobilization at the surface of the FTO-ZnO$_{350\ °C}$ sensor.

5.3.2 FTIR analysis

The interaction of PTCA with the surface of ZnO$_{350\ °C}$ was studied by Fourier transform infrared spectroscopy (FTIR). Figure 5.3 shows the FTIR spectra of ZnO$_{350\ °C}$|PTCA, unmodified ZnO$_{350\ °C}$ electrode, and PTCA. The spectrum obtained for ZnO$_{350\ °C}$|PTCA (a) presents absorption bands at 425 and 544 cm^{-1}, which are characteristic of the hexagonal wurtzite phase of ZnO and refer to the Zn-O bond stretching vibration, respectively.[268, 269] The absorption bands at 1010 and 933 eV refer to the stretching vibration of the C-O bond.[269] The bands at 808 and 740 cm^{-1} are related to the immobilized PTCA at the surface of ZnO and associated with the C-H bonds present in the PTCA molecule. The bands located from 1317 to 1590 cm^{-1} belong to the single and double bonds vibrations between carbons existing in the aromatic ring of the PTCA molecule, as well as O-H bonds associated with the carboxylic groups present in the molecule.[270] The bands at 1709 and 1746 cm^{-1} are related to the C=O bonds and the carboxylic groups present in the PTCA molecule. A small absorption band of O-H bond stretching vibration is observed at 3690 cm^{-1}. Therefore, FTIR results confirm the presence and interaction of the bands present in the PTCA molecule and the ZnO surface.

Figure 5.3 - FTIR spectra for (a) ZnO$_{350\ °C}$|PTCA, (b) ZnO$_{350\ °C}$, and (c) PTCA.

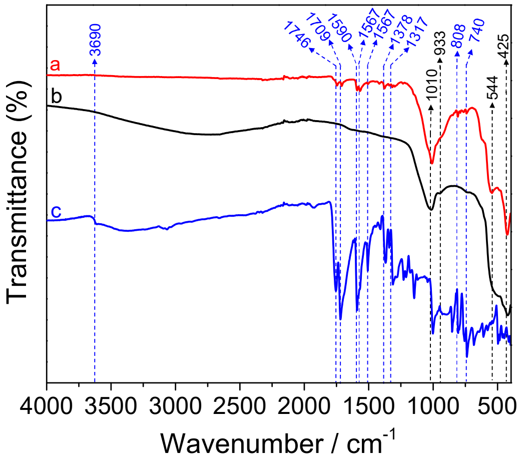

Source: Own authorship.

5.3.3 XPS analysis

XPS measurements were performed for the ZnO$_{350\ °C}$|PTCA to verify the chemical state of the elements and the presence of possible impurities in the film. XPS spectrum (survey) of ZnO$_{350\ °C}$|PTCA (Fig. 5.4) confirms the presence of zinc atoms (Zn 3d at 9.3 eV; Zn 3p at 87.4 eV; Zn 3s at 138.6 eV and Zn 2p at 1020.5 and 1043.4 eV), carbon (C 1s at 283.2 eV) and oxygen (O 1s at 530.3 eV). The signal related to the carbon atom is mostly related to PTCA, but there is also a small contribution of (adventitious) carbon from atmospheric CO_2, which usually occurs in samples when they are exposed to the air.[271] The presence of oxygen corresponds mainly to ZnO and PTCA, and a minority part comes from atmospheric oxygen.[234] Therefore, no impurities were found in the $ZnO_{350\,°C}$|PTCA.

Figure 5.4 - XPS spectrum of $ZnO_{350\,°C}$|PTCA.

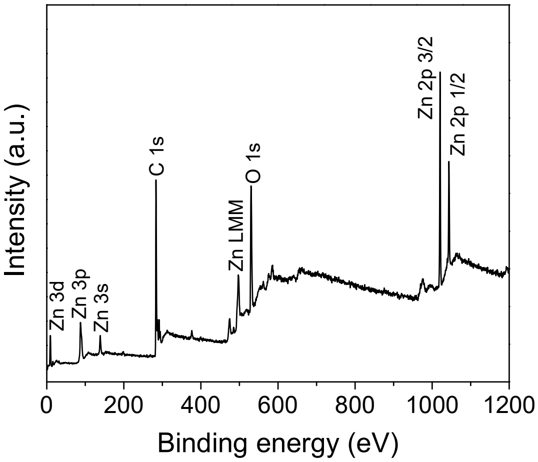

Source: Own authorship.

The oxygen bond composition (O 1s) present in $ZnO_{350\,°C}$|PTCA was investigated by XPS experiments (Fig. 5.5). The O 1s peak (in red) in Figure 5.5a was separated into components presenting the three different oxygen states, namely: oxygen assigned to -O-Zn bonds (in blue); oxygen assigned to O^{2-} ions (-O-deficient) in the oxygen vacancy regions of the ZnO crystalline structure (in green); and chemically adsorbed oxygen or hydroxyl groups present on the ZnO surface (-O-surface) (in pink). The study of the variation in O 1s composition for ZnO and $ZnO_{350\,°C}$ was discussed in the topic 4.3.1 (chapter 4). By comparing the spectra of the variation in O 1s composition in $ZnO_{350\,°C}$|PTCA (Fig. 5.5a) with the XPS results previously obtained for ZnO and $ZnO_{350\,°C}$ (Fig. 4.5a and 4.5b), it is possible to verify the increased presence of -O-deficient and -O-surface, and the decrease of -O-Zn bonds. The significant increase of -O-surface is attributed to the immobilization and interaction of the PTCA with the $ZnO_{350\,°C}$ surface. The variation of the oxygen percentage composition for each film can be confirmed from Figure 5.5b.

Figure 5.5 - XPS O 1s spectra of (a) $ZnO_{350\,^{\circ}C}$|PTCA and (b) percentage area relative to the -O-Zn, -O-deficient, and -O-surface groups for each film.

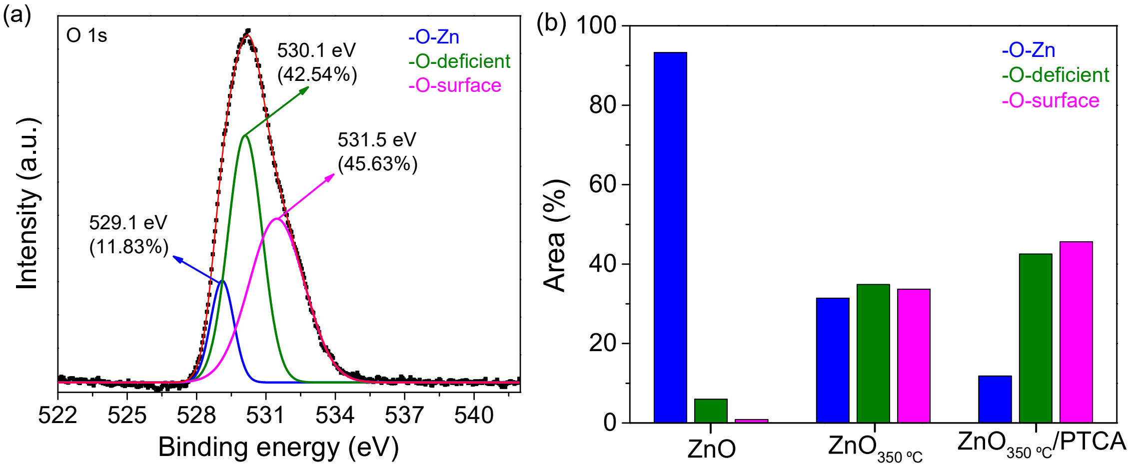

Source: Own authorship.

The variation in carbon bond composition (C 1s) was also investigated and the results are presented in Figure 5.6. Figure 5.6a presents the C 1s spectrum of the ZnO before annealing treatment, and the presence of C=C (283.9 eV), C-C (284.8 eV), and C-O-C (287.8 eV) carbon bonds were observed. After annealing treatment, the spectrum of the $ZnO_{350\,^{\circ}C}$ presented a small percentage of O-C=O bonds (288.4 eV) (Fig. 5.6b). The increase of O-C=O bonds is verified in the C 1s spectrum for the $ZnO_{350\,^{\circ}C}$ modified with PTCA, which may be related to the existing carboxylic bonds in the PTCA molecule (Fig. 5.6c).

Figure 5.6 - XPS C 1s spectra of the films (a) ZnO, (b) $ZnO_{350\,^{\circ}C}$, and (c) $ZnO_{350\,^{\circ}C}$|PTCA.

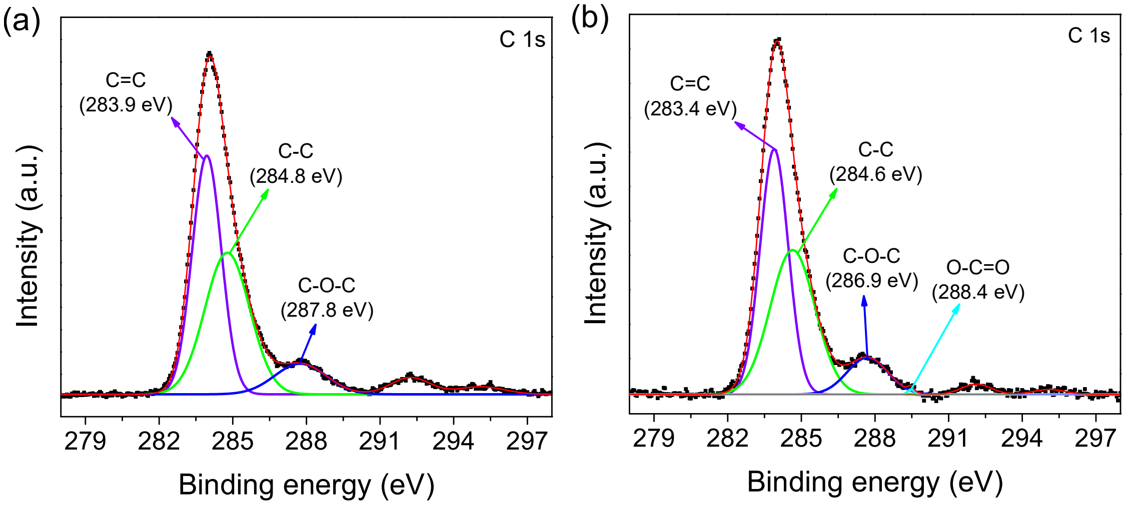

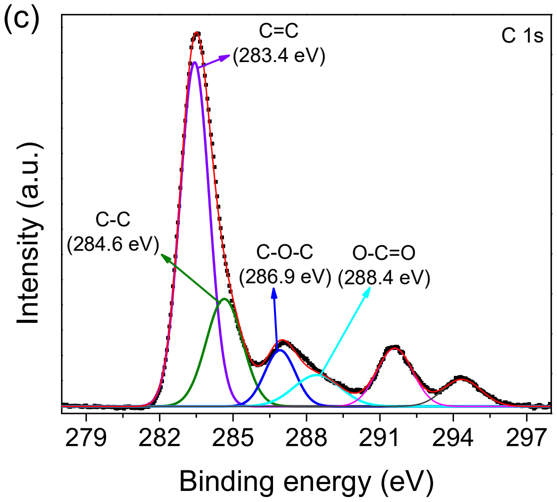

Source: Own authorship.

5.3.4 Band gap calculation

The annealing treatment and the surface modification with PTCA provided a morphological change in ZnO structure. The $ZnO_{350\ °C}$|PTCA was characterized by spectrophotometric techniques to evaluate its optical properties. The interaction between the PTCA and the surface of the ZnO occurs by hydrogen bonds through the active carboxyl groups.[59] As PTCA absorbs in a wide range of the visible region, it has advantages as a photosensitizer, improving the electron transfer.[253] Absorbance measurements using a UV-Vis spectrophotometer were performed to verify the wavelengths of the PTCA, $ZnO_{350\ °C}$, and $ZnO_{350\ °C}$|PTCA (Fig. 5.7a). Therefore, the absorption band from 394 to 473 nm verified for the $ZnO_{350\ °C}$|PTCA is associated with PTCA.[272] A Kubelka-Munk graph, which relates the absorption coefficient ($(\alpha hv)^2$) and the incident photon energy (hv) obtained from the diffuse reflectance results of $ZnO_{350\ °C}$|PTCA, is presented in the Figure 5.7b. The E_g is estimated by extrapolating the linear region of the curve from the graph $(\alpha hv)^2$ *vs* hv to the intersection point with the baseline of the spectrum, where the maximum energy absorption by ZnO is observed. Thus, a band gap of 2.94 eV is estimated for the $ZnO_{350\ °C}$|PTCA. ZnO is a direct band gap semiconductor, with a theoretical band gap of approximately 3.37 eV.[273] Accordingly, the annealing treatment and the modification of the ZnO surface causes a decrease in the band gap value compared to the theoretical value. This ensures a rapid decrease in reflectance because ZnO absorbs energy easily equal or greater than E_g and rapidly generates an electron-hole pair with a significant photocurrent signal.[241]

Figure 5.7 - (a) Absorbance spectra of the ZnO$_{350\,°\mathrm{C}}$|PTCA (▬), ZnO$_{350\,°\mathrm{C}}$ (▬) and PTCA (▬); (b) Kubelka-Munk graph for ZnO$_{350\,°\mathrm{C}}$ and ZnO$_{350\,°\mathrm{C}}$|PTCA.

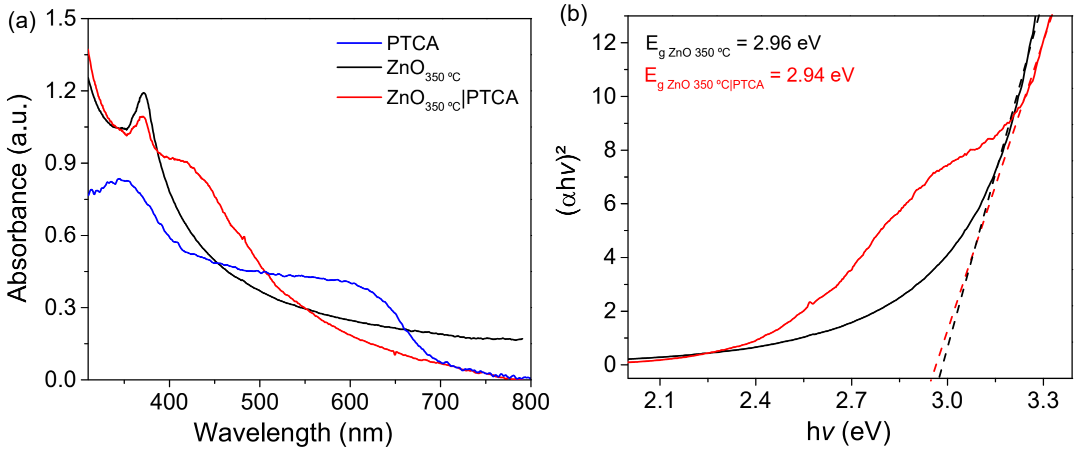

Source: Own authorship.

5.3.5 PEC analysis

5.3.5.1 Dependency on FTO-ZnO$_{350°\mathrm{C}}$|PTCA and applied potentials

LSV measurements were performed to evaluate the FTO-ZnO$_{350°\mathrm{C}}$|PTCA behavior in the absence and presence of the target molecule. The study was carried out in PBS buffer solution (pH 7.0) containing 8.0 nM 4-NP, under chopped-light illumination (Fig. 5.8).

Figure 5.8 - Photocurrent transients for FTO-ZnO350 $_{°\mathrm{C}}$|PTCA in the absence (▬) and presence (▬) of 8 nM 4-NP in 10 mM PBS buffer (pH 7.0) under UV-A illumination.

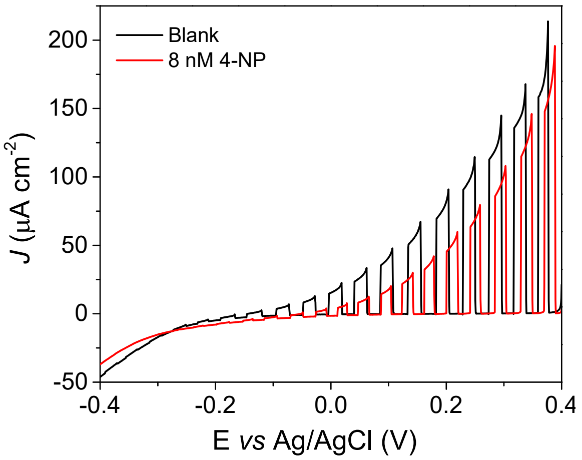

Source: Own authorship.

Under illumination, ZnO modified with PTCA absorbs radiation from UV-A light, therefore the electrons from the HOMO of PTCA are excited and promoted to its LUMO, and subsequently, the electrons from the valence band of the semiconductor are promoted to its conduction band. Accordingly, the electrons from the LUMO are quickly transferred to the conduction band of ZnO and collected by the electrochemical system registering an anodic photocurrent. In the presence of 4-NP, the analyte acts as an electron receptor species, due to its molecular energy level. Therefore, in this PEC system, the presence of 4-NP promotes the decay in the photocurrent response, due to the scavenger of electrons from the surface of the FTO-ZnO$_{350\ °C}$|PTCA sensor (Fig. 5.9).

Figure 5.9 - Proposed schematic representation for the amperometric detection of 4-NP using the FTO-ZnO$_{350\ °C}$|PTCA photosensor.

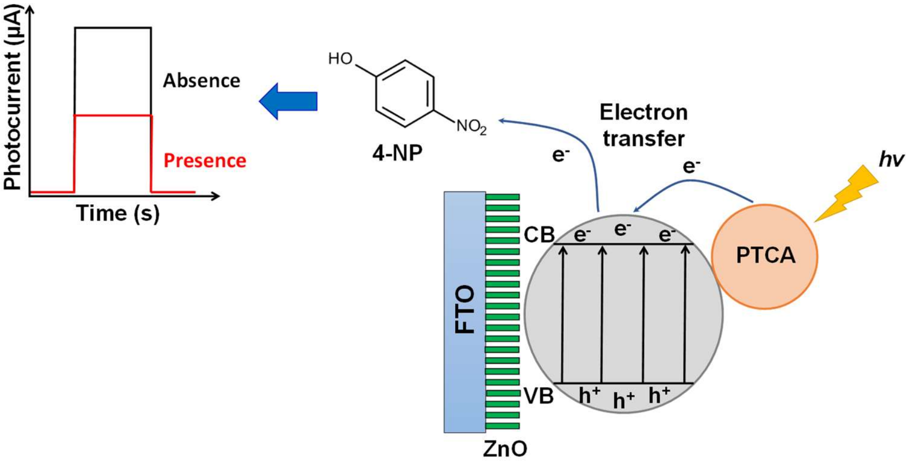

Source: Own authorship.

5.3.5.2 Working potential

The applied potential has fundamental importance in amperometric analyses as it contributes to the sensitivity of the method. Thereby, the effect of the potential on the photocurrent response of FTO-ZnO$_{350\ °C}$|PTCA in the presence of 4-NP was investigated (Fig. 5.10). The results show a gradual increase of the photocurrent response in the range from -0.3 to 0.3 V (*vs* Ag/AgCl). However, a considerable increase of the standard deviation (SD) of the photocurrent responses is observed for applied potential above 0.2 V, representing instability of the measured photocurrent. Moreover, the increase of about 40% of the photocurrent is not significant because of the increase of the SD (approximately 300%).

Figure 5.10 - Influence of the applied potential on the PEC response of the FTO-$ZnO_{350\ °C}$|PTCA in the presence of 8.0 nM 4-NP in 10 mM PBS buffer (pH 7.0) under UV-A illumination.

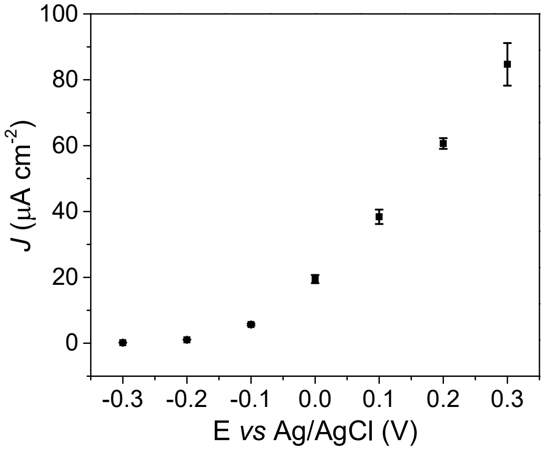

Source: Own authorship.

5.3.5.3 pH effect and supporting electrolyte

The effect of the pH on the amperometric response of FTO-$ZnO_{350\ °C}$|PTCA in the presence of 8.0 nM 4-NP was studied in the range from 5.0 to 9.1 (Fig. 5.11). A significant increase of the photocurrent response is observed from pH 5.0 to 6.0, and then a small increase to pH 7.0. At pH greater than 7.0 the decrease of the photocurrent response is observed (pH 8.1 and 9.1). A maximum value of photocurrent was obtained for pH 7.0, a value close to the pKa reported in the literature for 4-NP (pKa 7.1).[274] Thus, the reaction rate is favored in neutral pH. Moreover, the chemical nature of the synthesized ZnO semiconductor film in the long term shows instable photocurrent in acidic pH. ZnO film is high solubel in acid medium, promoting its removal from the substrate surface. Therefore, pH 7.0 was selected as optimal pH for further experiments.

The study of the supporting electrolyte was performed using PBS and Britton-Robinson (BR) buffers and sodium sulfate solution (Na_2SO_4) pH 7.0. The photocurrent responses are presented in Figure 5.12. BR buffer solution effects negligibly on the PEC responses of the FTO-$ZnO_{350\ °C}$|PTCA in the presence of 8.0 nM 4-NP. The photocurrent values of 7 μA cm^{-2} were obtained for Na_2SO_4 and PBS buffer. The instability of FTO-$ZnO_{350\ °C}$|PTCA photocurrent in Na_2SO_4 was evaluated using RSD. The results show an increase of about 6-fold compared to RSD obtained for the measurements in PBS buffer solution. Thus, the PBS buffer with the highest photocurrent response and a lower RSD (0.107 μA cm^{-2}) is the ideal supporting electrolyte for the proposed electrochemical system.

Figure 5.11 - Influence of pH on the PEC response of the FTO-ZnO$_{350\,°C}$|PTCA in the presence of 8.0 nM 4-NP, applied potential of 0.2 V (*vs* Ag/AgCl) under UV-A illumination. Inset: Graph relating pH and photocurrent densities with their respective SD.

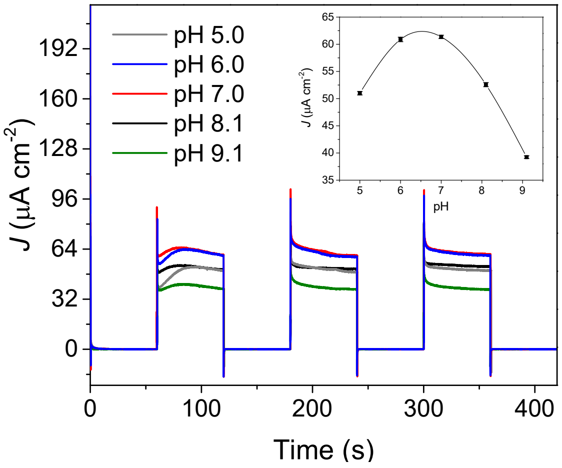

Source: Own authorship.

Figure 5.12 - Influence of the supporting electrolyte (pH 7.0) on the PEC response of the FTO-ZnO$_{350\,°C}$|PTCA in the presence of 8.0 nM 4-NP, applied potential 0.2 V (*vs* Ag/AgCl) under UV-A illumination. Inset: supporting electrolyte *vs* photocurrent densities.

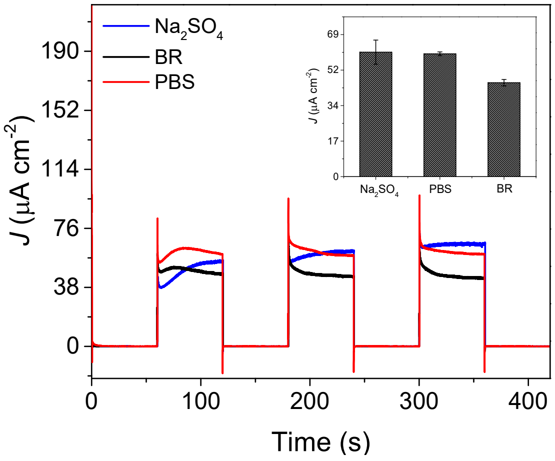

Source: Own authorship.

5.3.5.4 Amperometric detection of 4-NP using ZnO$_{350°C}$|PTCA under UV-A illumination

The proposed photosensor was applied for the quantification of 0.1, 2.0, 3.0, 5.0, 7.0, 8.0, 9.0, 11.0, 13.0, 15.0 and 50 nM 4-NP in 10 mM PBS buffer (pH 7.0). Considering the decrease of the amperometric response of the FTO-ZnO$_{350\,°C}$|PTCA sensor in the presence of 4-NP (Fig. 5.13a), the calibration curve was plotted as a function of the decreasing photocurrent response ((I_0 – I)/I_0) with increasing analyte concentration in solution, as shown in Figure 5.13B.

Figure 5.13 - (A) Amperometric response for the FTO-$ZnO_{350\ ^{\circ}C}$|PTCA in the absence (a) and presence of 4-NP in the concentration range from 0.1 to 15.0 nM (b – k). (B) Calibration and linear curve.

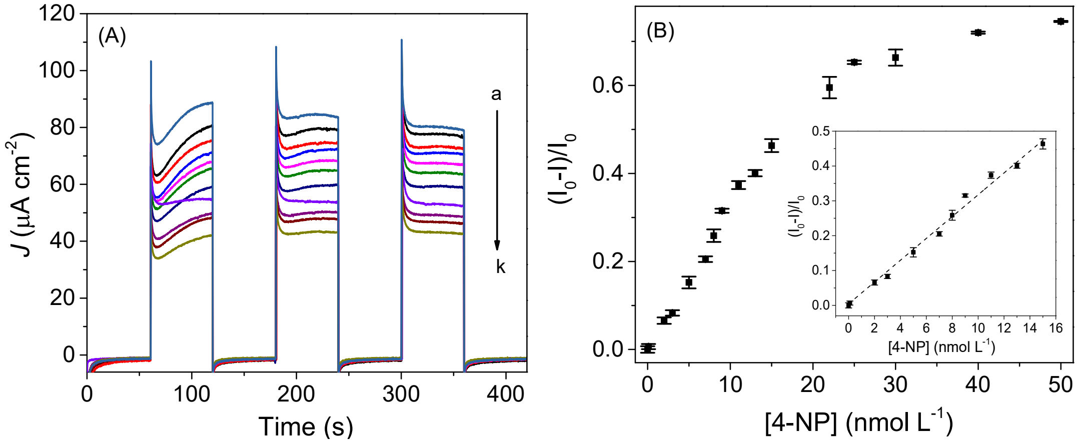

Note: I_0 and I correspond to the photocurrent response of the sensor in the absence and presence of 4-NP, respectively. Source: Own authorship.

As previously discussed, in this analytical system, the 4-NP molecule acts as an electron receptor species and a decrease in photocurrent response with the increase of the analyte concentration in solution is expected. Under optimized conditions, the photosensor showed a good linear correlation for 4-NP detection (0.993) for concentration range from 0.1 to 15.0 nM. The LOD and the sensitivity calculated for 4-NP detection using the FTO-$ZnO_{350\ ^{\circ}C}$|PTCA photosensor were 0.09 nM and 0.51 A M^{-1} cm^{-2}, respectively. The notable analytical performance of the developed photosensor is compared with previously reported PEC and electrochemical sensors for the detection of 4-NP (Table 5.1).

Table 5.1 - Analytical performance of the previously reported PEC and electrochemical sensors for 4-NP detection

Sensor	Method	LOD (nM)	Sensitivity (A M^{-1} cm^{-2})	Reference
CS/rGO/Pd/GCE	DPV	86.0	0.07	275
CB/β-CD/SPCE	DPV	40.0	9.17	276
Ni/Cu_2O photocathode	PEC	16.0	---	277
CMO Ns/GCE	DPV	10.0	2.46	278
NiS_2-rGO/CMNPs/GCE	DPV	6.90	2.43	279
GO/AuNPs/ZnAPTPP	PEC	0.04	---	280
FTO-$ZnO_{350\ ^{\circ}C}$|PTCA	PEC	0.09	0.51	This work

Key: CS, chitosan; rGO, reduced graphene oxide; GCE, glassy carbon electrode; CB, carbon black; CD, cyclodextrin; SPCE, screen-printed carbon electrode; Ni, nickel; Cu_2O, copper(I) oxide; CMO Ns,

$CoMnO_3$ nanosheets; NiS_2, nickel disulfide; CMNPs, curcumin nanoparticles; GO, graphene oxide; AuNPs, gold nanoparticles; ZnAPTPP, zinc monoamino porphyrin; PEC, photoelectrochemical. Source: Own authorship.

Control experiments were carried out to evaluate the performance of the FTO-ZnO$_{350\ °C}$|PTCA photosensor in the linear range determined for 4-NP detection (0.1 – 15.0 nM) and the calibration curves are presented in Figure 5.14. The results show very low photocurrent responses using the FTO-ZnO sensor before annealing treatment and without surface modification. Similar behavior is observed for ZnO modified with the PTCA (FTO-ZnO|PTCA), but an average increase of about 11-fold in photocurrent response is observed compared to the FTO-ZnO sensor. A significant increase in photocurrent response for 4-NP detection is observed using annealed FTO-ZnO$_{350\ °C}$. As discussed in chapter 4, the annealing treatment increases the crystallinity of the semiconductor-based material and increases significantly the photocurrent response. The photocurrent has increased about 20% compared to the FTO-ZnO$_{350\ °C}$ sensor after combining the annealing treatment and surface modification (FTO-ZnO$_{350\ °C}$|PTCA). This result proves that under illumination PTCA assists in signal enhancement by increasing the electron transfer rate from ZnO to the system (Fig. 5.12b). The calibration curves obtained for the control experiments using FTO-ZnO and FTO-ZnO|PTCA photosensors did not show good linearity for the selected working range in comparison to FTO-ZnO$_{350\ °C}$ and FTO-ZnO$_{350\ °C}$|PTCA photosensors. This confirms that the annealing treatment and the surface modification steps contribute significantly to the sensitivity of the developed method for 4-NP detection.

Figure 5.14 - (a) Calibration curves for FTO-ZnO (●), FTO-ZnO|PTCA (▲), FTO-ZnO$_{350\ °C}$ (▼) and FTO-ZnO$_{350\ °C}$|PTCA (■) photosensors, concentration range from 0.1 to 15.0 nM 4-NP. (b) Amperometric responses for the photosensors in the presence of 8.0 nM 4-NP.

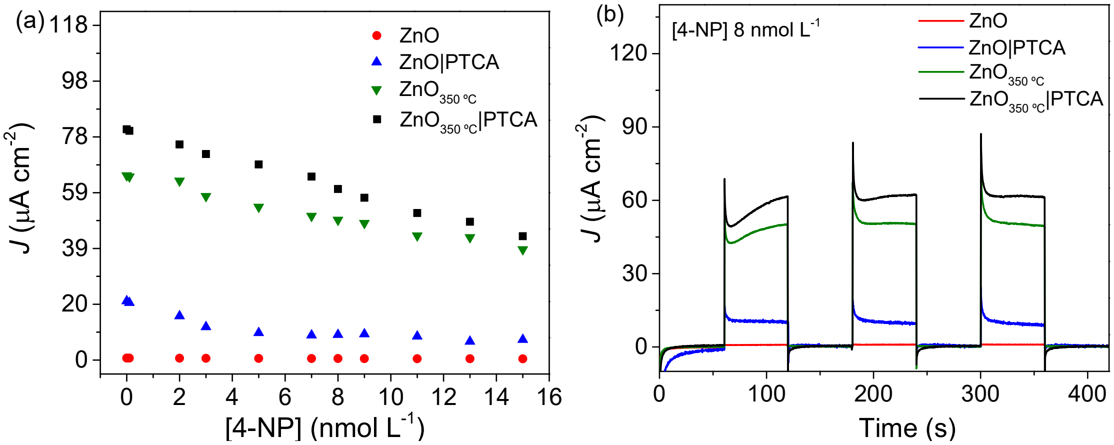

Source: Own authorship.

5.3.5.5 Stability study

The stability of the proposed photosensor was evaluated by following the changes in the photocurrent during 1240 s of uninterrupted measurement. Considering 10 amperometric responses for the detection of 8.0 nM 4-NP in 10 mM PBS buffer (pH 7.0) (Fig. 5.15), a decrease of only 6.17% in the photocurrent response was observed. The stability of the developed sensor is related to the good adherence of the PTCA-modified ZnO film to the surface of the FTO substrate and due to the physic-chemical properties of the synthesized ZnO nanotubes.

Figure 5.15 - Stability study of the photocurrent response using the FTO-$ZnO_{350\ °C}$|PTCA photosensor for the detection of 8.0 nM 4-NP in 10 mM PBS buffer (pH 7.0) and applied potential of 0.2 V (*vs* Ag/AgCl).

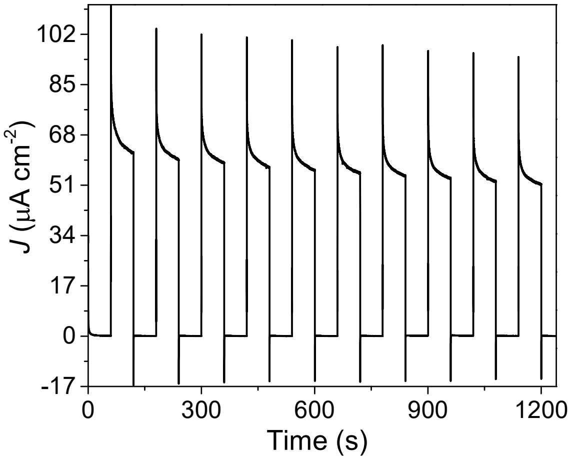

Source: Own authorship.

5.3.5.6 Repeatability and reproducibility

The repeatability of the proposed photosensor was verified through the variations in the amperometric responses recorded in the presence of 8.0 nM 4-NP in 10 mM PBS buffer (pH 7.0), using the same sensor during 5 days (Fig. 5.16a). The repeatability plot shows the stability of the average photocurrent between days I and III and a significant increase in the SD is observed. The photocurrent response starts to decrease from day IV. A decrease of 6.9% in the photocurrent value is observed from day I to day V. This decrease may be related to the adsorption of molecules from the air on the sensor surface, thus inhibiting the photocurrent signal and increasing the SD over the days.

The reproducibility study for FTO-$ZnO_{350\ °C}$|PTCA was performed by evaluating the photocurrent responses of four photosensors (E1, E2, E3, and E4) prepared using the same optimized methodology (synthesis, annealing treatment, and PTCA immobilization) used for the detection of 8.0 nM 4-NP (Fig. 5.16b). A low RSD (1.3%) was calculated for the amperometric responses of different photosensors, proving that the methodology developed for the preparation of the FTO-ZnO$_{350\ ^{\circ}C}$|PTCA photosensor is reproducible.

Figure 5.16 - (a) Repeatability and (b) reproducibility study of the FTO-ZnO$_{350\ ^{\circ}C}$|PTCA photosensor for the detection of 8.0 nM 4-NP in 10 mM PBS buffer (pH 7.0) and applied potential of 0.2 V (*vs* Ag/AgCl) (n = 3).

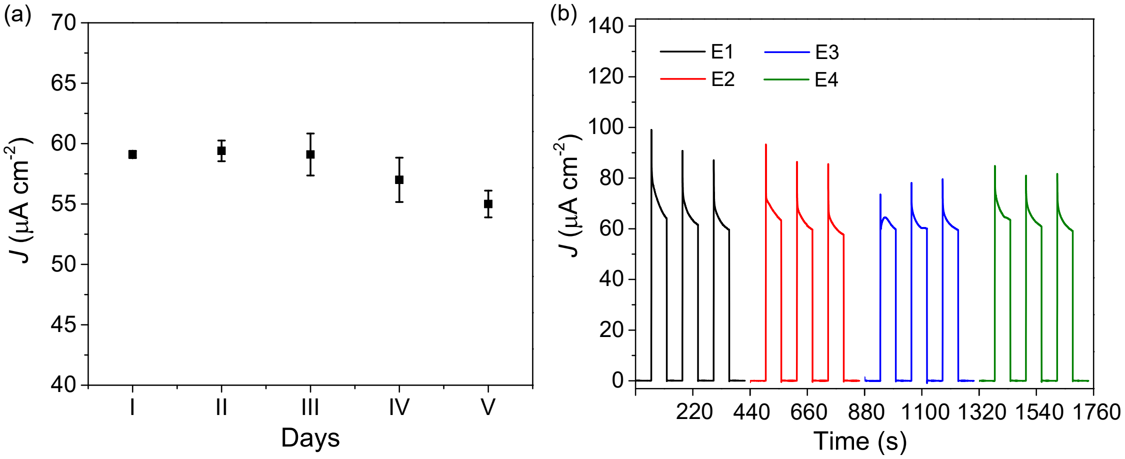

Source: Own authorship.

5.3.5.7 Interfering study

The amperometric response of the FTO-ZnO$_{350\ ^{\circ}C}$|PTCA photosensor for 4-NP detection was verified in the presence of possible interfering molecules that may coexist in the same matrix. As the main goal is to use the developed photosensor for the detection of 4-NP in complex water samples, the phenolic compounds such as hydroquinone (HQ), 3-nitrophenol (3-NP), phenol (Ph), 3-aminophenol (3-AP), and bisphenol-A (BPA). In addition, the interference of the metal cations Fe^{3+}, Mn^{2+}, Zn^{2+}, Pb^{2+}, and Cd^{2+} were investigated as possible interferents because they are routinely found in this type of matrix. The interferents were prepared in 10 mM PBS buffer (pH 7.0). The amperometric response was recorded for a solution containing 8.0 nM 4-NP and compared with the amperometric response of a solution containing the mixture of 4-NP: interferents, in a ratio of 1:1 for phenolic compound and 1:100 for metallic cations (applied potential of 0.2 V (*vs* Ag/AgCl) and under UV-A illumination) (Fig. 5.17).

Figure 5.17 - Amperometric response of FTO-ZnO$_{350\,^{\circ}\mathrm{C}}$|PTCA photosensor in the presence of 8.0 nM 4-NP and interfering molecules, in a ratio of (a) 1:1 for HQ, 3-NP, Ph, 3-AP, and BPA, and in a ratio of (b) 1:100 for Fe^{3+}, Mg^{2+}, Zn^{2+}, Pb^{2+}, and Cd^{2+} (n = 3).

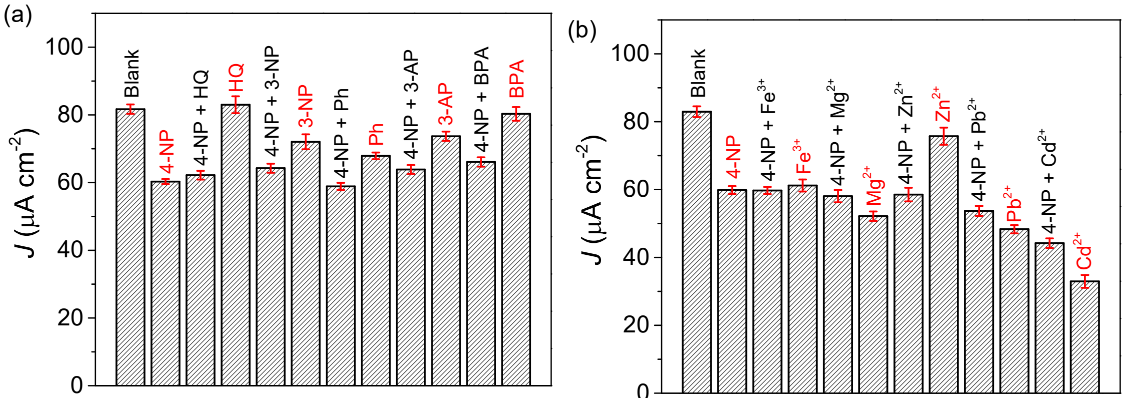

Source: Own authorship.

The amperometric response for 4-NP showed an increase of 3.1%, 6.5%, 5.9%, and 7.9% in the presence of HQ, 3-NP, 3-AP, and BPA, respectively, and a decrease of 6.1% in the presence of Ph. In the presence of the cations Fe^{3+}, Mg^{2+}, Zn^{2+}, Pb^{2+} and Cd^{2+}, a decrease of 0.2%, 2.9%, 2.2%, 9.8%, and 26.1%, respectively, of the amperometric response for 4-NP was observed. Therefore, this study showed that there were no significant changes in the detection response of 4-NP in the presence of phenolic substances and metallic cations, except for Cd^{2+} which can be considered a possible interfering agent.

5.3.5.8 Applicability of FTO-ZnO$_{350\,^{\circ}\mathrm{C}}$|PTCA

The applicability of the photosensor was investigated for the detection of 4-NP in natural water and tap water samples. Water samples were buffered and fortified with known amounts of 4-NP and calibration curves were obtained in the concentration range from 0.5 to 15.0 nM, using the same optimized experimental conditions for the analytical curve of 4-NP in PBS buffer (pH 7.0) (Fig. 5.18). The calibration curves correlate the decrease of photocurrent response $((I_0 - I)/I_0)$ with increasing analyte concentration in solution. The curves obtained for the natural water sample (blue) and the tap water sample (red) show an increase in the response $(I_0 - I)/I_0$ compared to the calibration curve obtained for 4-NP in PBS buffer. This increase in photocurrent response may be associated to a matrix effect and/or the influence of random errors.

Figure 5.18 - Calibration curves obtained for the detection of 4-NP in the concentration range from 0.5 to 15.0 nM in PBS buffer (pH 7.0), in natural, and tap water.

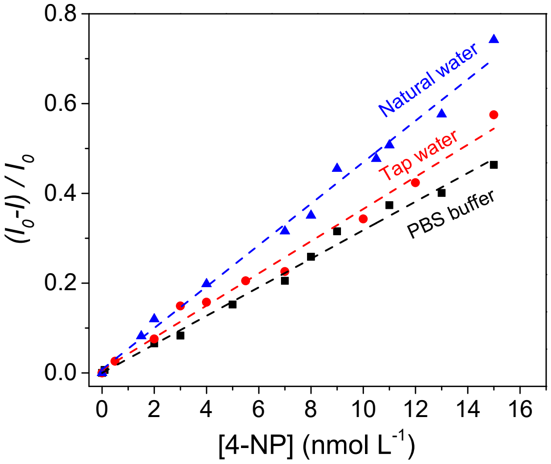

Note: I_0 and I correspond to the photocurrent response of the sensor in the absence and presence of 4-NP, respectively. Source: Own authorship.

The influence of the real sample on the detection responses was investigated. The recovery study was performed using the calibration curves obtained in the samples (Table S5.1). Three levels of 4-NP fortification were evaluated for natural water (1.5, 8.0, and 13.0 nM) and for tap water (0.5, 4.0, and 10.0 nM). The recovery values were found in the range of 93.7% to 107.6 % for tap water, with RSD less than 4.5% and for natural water in the range of 94.6% to 108.1%, with RSD less than 5.2%. These results confirm the potential of the photosensor for the determination of 4-NP in complex samples such as natural water.

5.3.6 Chromatographic detection of 4-NP

The quantification of 4-NP was also performed by the chromatographic detection technique (HPLC), in order to statistically compare the detection results with those obtained by the PEC technique. The chromatographic parameters were optimized for the detection of 4-NP, based on the detection method for this class of compounds described by the U.S. EPA.[267] Experiments were carried out varying the proportion of the organic mobile phase to combine a well-defined chromatographic peak with a shorter retention time. The mobile phase was composed by ACN:phosphoric acid (0.025 M) (60:40, v/v) and isocratic mode, flow rate of 1.0 mL/min, at $\lambda = 315$ nm and injection volume of 20 µL. The chromatographic detection response for 4-NP and its respective linear calibration curve is presented in Figure 5.19.

Figure 5.19 - (a) Chromatogram of 10.0 μM 4-NP prepared in acetonitrile (ACN) and (b) calibration curve for 4-NP in the concentration range from 5.0 to 50.0 nM.

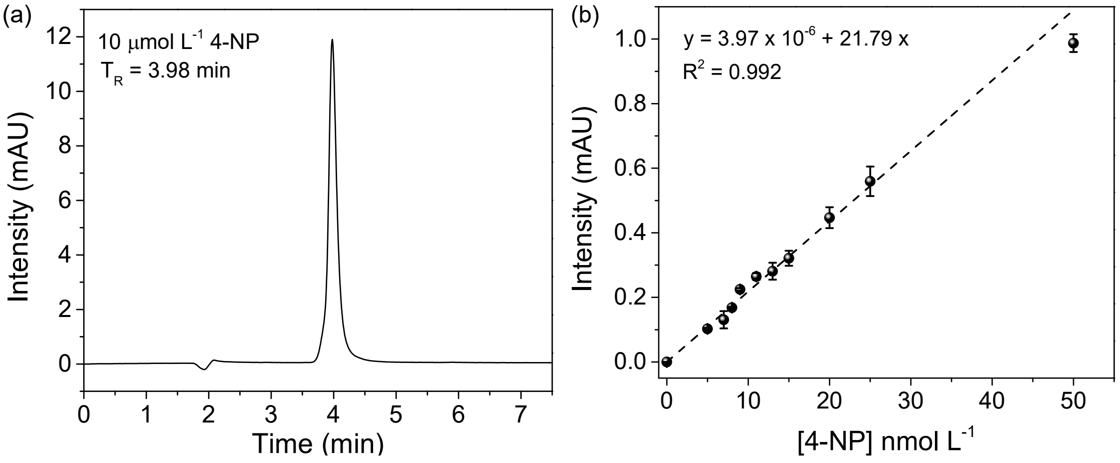

Source: Own authorship.

Under optimized conditions, the chromatographic detection of 4-NP showed good linear correlation ($R^2 = 0.992$), with a calculated LOD of 4.6 nM, repeatability of 2.6% (RSD, n = 7) and reproducibility of 3.7% (RSD, n = 5).

The natural water sample collected from a WTP and the tap water sample were also analyzed by HPLC for the quantification of 4-NP and the detection results are presented in Figure S5.2. Calibration curves were obtained for 4-NP in the concentration range from 5.0 to 15.0 nM in pre-filtered water samples, using the standard addition method. The analytical calibration curves in water samples were compared to the one obtained in organic solvent (ACN), to verify the existence of a matrix effect (Fig. S5.2). The recovery study was also carried out for the chromatographic detection of 4-NP and values of recovery were obtained in the range from 92.5 to 105.3% for tap water, with RSD lower than 5.4% and in the range from 91.7 to 107.4% for natural water, with RSD lower than 6.2%.

5.3.7 Statistical study

The comparison between methods was evaluated by the linear regression of the calibration curves obtained for the results of PEC detection plotted on the y-axis and the results obtained by the standard detection technique (HPLC) plotted on the x-axis, for each sample analyzed in the same concentration range of 4-NP. An excellent correlation between methodologies was observed for the detection of 4-NP in natural ($a = 0.031$, $b = 0.999$ and $R^2 = 0.998$) and tap water ($a = 4.22 \times 10^{-4}$, $b = 0.996$ and $R^2 = 0.999$) samples, as evidenced in Figure 5.20.

Figure 5.20 - Linear regression plots of the detection values for 4-NP obtained by photoelectrochemical (PEC) and chromatographic (HPLC) techniques in (a) tap and (b) natural water samples.

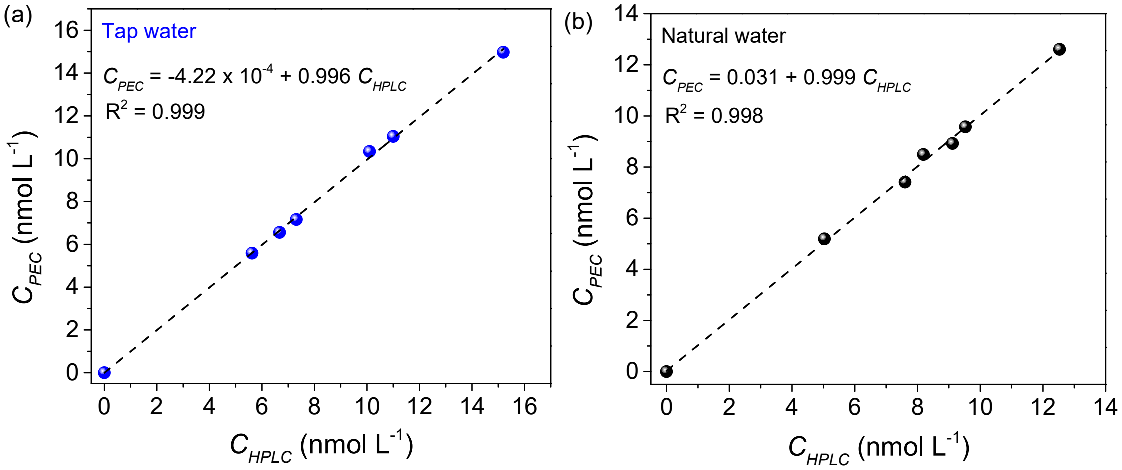

Source: Own authorship.

In order to confirm whether the two methodologies are analogous for the detection of 4-NP in the concentration range of 5.0 to 15.0 nM (n −1 = 5), the detection results for both samples were evaluated by applying the paired *t*-test.[262] The critical value for n = 6, at 95% confidence, is 2.57 (DF = 5; α = 0.05).[262] Values of 0.61 for the tap water sample and 0.41 for the natural sample were obtained. Therefore, the calculated *t*-test values are lower than the reference critical value, demonstrating that the results obtained for the detection of 4-NP in water samples by PEC and chromatographic techniques are considered statistically equivalent. Thus, the optimized PEC methodology used for 4-NP detection is analogous to the standard chromatographic methodology.

5.4 CONCLUSIONS

In this work, we presented a novel PEC sensor based on synthesized ZnO nanorods with advanced physic-chemical properties for the successful detection of 4-NP under UV-A illumination. The surface of the $ZnO_{350\ °C}$ was modified with the photosensitizer PTCA which provided increased photocurrent response. The $ZnO_{350\ °C}$|PTCA was characterized by using FTIR, XPS, and UV-vis spectroscopy. An enhancement of 20% in the photocurrent response of ZnO was observed by immobilizing 9.3 mM PTCA on the surface. The PTCA played an important role by providing an increase in the electron transfer rate from ZnO to the system. The FTO-$ZnO_{350\ °C}$|PTCA sensor presented good repeatability (RSD 6.9%) and reproducibility (RSD 1.3%). The applicability of the proposed photosensor was evaluated by sensing 4-NP in natural and tap water, attesting a great potential of the developed PEC strategy for monitoring water quality. Based on the optimized method, the chromatographic detection of 4-NP in real samples was also performed for statistical comparison of the detection results obtained by the PEC method. Using paired *t*-test, it was demonstrated that the developed PEC method can determine 4-NP in concentration range from 5.0 to 15.0 nM, in complex samples, with high accuracy like the chromatographic method. According to the results, the developed PEC sensing strategy emerges as a robust and promising tool for sub-nM monitoring of 4-NP in water.

CONCLUSIONS AND OUTLOOK

This thesis presented the development of novel PEC strategies for the detection of phenolic compounds in aqueous samples. The main goal of the thesis was the construction of high-performance photosensors and portable approaches for the on-site monitoring of phenolic compounds. Commercial TiO_2 and synthesized ZnO were successfully used to fabricate three PEC sensors, namely SPE|TiO_2, SPE|AuNPs@TiO_2, and FTO-$ZnO_{350\ °C}$|PTCA. Integration of the TiO_2-based sensors into a portable flow injection cell provided higher sensitivity and consequently lower detection limits. The optimized synthesis of the nano-sized ZnO combined with a post-growth annealing treatment and modification with the photosensitizer PTCA provided higher sensitivity and low limit of detection for sensors based ZnO.

The first proposed PEC sensing strategy concerns the development of a simple and cost-effective flow injection-based amperometric photosensor for the quantification of 4-AP (chapter 2). In this regard, a homemade flow cell was designed for PEC analyses using TiO_2-based photosensors. Graphite screen printed electrodes were modified with TiO_2 (P25) suspension without any modification (SPE|TiO_2). Addition of Nafion® as an adhesive binding material ensured the stability of TiO_2 at the surface of the electrode during flow measurements. The sensitive detection of HQ (as a model molecule) and 4-AP was possible due to the presence of ROS at the surface of TiO_2 under UV light. Under optimized conditions, the sensitivity and limit of detection for 4-AP were 0.6 A M^{-1} cm^{-2} and 18 nM, respectively.

Taking advantage of the intrinsic features of TiO_2 (P25) and the benefits of the FIA system demonstrated in chapter 2, another flow injection-based photosensor was developed in the subsequent chapter, this time by impregnating AuNPs into TiO_2 structure (chapter 3). Size-controlled AuNPs with an estimated average size of 18.7 ± 3.8 nm were successfully impregnated into TiO_2 by photo-assisted synthesis. XRD, Raman spectroscopy, SEM, EDX, TEM were used to characterize the surface of the plasmonic catalytic (AuNPs@TiO_2). UV-DR analysis was also performed to determine its band gap. Based on those characterization results, the presence of AuNPs significantly improved TiO_2 light absorption ability by the SPR effect. SPE|AuNPs@TiO_2 was prepared using the same modification protocol of graphite screen printed electrodes described in the previous chapter. ROS generated on SPE|AuNPs@TiO_2 under visible light were responsible for the quantification of HQ. The detection limit of 33.8 nM was calculated for HQ with a sensitivity of 0.22 A M^{-1} cm^{-2}. In addition, AuNPs@TiO_2 can also be used as a photocatalyst in environmental remediation strategies for organic contaminants.

Although the synthesis of ZnO nanorods has been widely studied, the use of this semiconductor-based material as PEC sensors is not yet widespread. Therefore, the third configuration exploits the unique photocatalytic properties of ZnO nanorods in the construction of a high-performance photosensor. In chapter 4, well-aligned ZnO nanorods with enhanced optical properties were synthesized on FTO substrate by a low-temperature electrodeposition method in the absence of catalyst or seed layer. A post-growth annealing study was performed. XRD, SEM, XPS, UV-DR, Raman spectroscopy, and electrochemical techniques were used to characterize the nanorods. Morphological characterization confirmed the strong influence of the post-growth annealing temperature of ZnO on its crystallinity. At 350 °C, larger crystallite size and maximum crystallinity were observed for ZnO nanorods. Amperometric measurements confirmed the improvement in its electrical properties, with a 94-fold increase in the average photocurrent response after annealing treatment at 350 °C. Therefore, the improved photocatalytic properties of FTO-$ZnO_{350\ °C}$ have made it more attractive for the construction of another PEC sensing strategy for phenols, described in the following chapter.

Immobilization of perylene acid (PTCA) on the surface of FTO-$ZnO_{350\ °C}$ allowed the extension of the light absorption capacity of ZnO nanorods into the near visible range (chapter 5). Also, PTCA played an important role by increasing the electron transfer rate from ZnO to the system. FTIR, XPS, and UV-vis spectroscopies were used to characterize the surface of FTO-$ZnO_{350\ °C}$|PTCA. FTIR results proved hydrogen bonds through the active carboxyl groups in PTCA were responsible for the surface interaction with ZnO nanorods. A negligible background current was observed in this PEC methodology as a consequence of robust and controlled synthesis protocol of ZnO nanorods. The stability of FTO-$ZnO_{350\ °C}$|PTCA sensor was confirmed by repeatability and reproducibility studies. Under optimized experimental conditions, the detection mechanism was based on electron harvesting by 4-NP from the ZnO surface upon UV-A light, leading to a reduction in electron transfer between ZnO and the electrode. Thus, the FTO-$ZnO_{350\ °C}$|PTCA photosensor was used to quantify 4-NP by recording the decrease of photocurrent response that was proportional to the increasing concentration of the analyte in the solution. The proposed PEC strategy resulted in a good linear correlation with high sensitivity 0.51 A M^{-1} cm^{-2} and a limit of detection of 0.09 nM for 4-NP. A statistical study confirmed that the developed PEC method can determine 4-NP with high accuracy like the traditional chromatographic method.

One of the significant advantages of these three PEC sensing methodologies described in this thesis is detection in nM range for phenols with high sensitivities. This result confirms the potential of the developed sensors and the placement of PEC as a valuable and promising analytical technique. Moreover, the straightforward and robust manufacturing protocols used for each setup combined with the easily portable approaches are the attractive points of the developed sensing analytical strategies. Herein, the photosensors were developed for analyses of phenols in river water (chapter 2 and 5), effluent (chapter 3), and tap water (chapter 5). However, their efficiency and accuracy suggest that they can also be used in a wider range of sensing applications, for example, in the analysis of food and human fluids.

Both TiO_2 and ZnO are semiconductor materials with unique features and easy-access. They are an excellent support material for doping or heterojunctions. Many attempts have been made to improve their physicochemical properties and photocatalytic activity. Therefore, the developed sensors can be combined with other organic or inorganic materials and make innovative heterojunctions by taking advantage of the different possibilities to extend their light absorption range. Another highlight of the sensing approaches developed in this thesis is the use of cost effective materials and the construction of a homemade PEC flow cell with a capacity of 400 μL. This PEC flow cell was idealized with the goal of the lowest possible waste discharge during flow analyses.

Technology transfer is always desired in the analytical community, especially for electrochemists. By envisioning the future possibility of bringing the photosensors developed from the fundamental research to the marketplace, the results of sensitivity, reproducibility/repeatability, and stability can ensure their reliability for commercial purposes. However, the challenge of manufacturing high-quality sensors at a large scale is still a step that needs to be particularly evaluated. Another challenge to be overcome is the demand for the development of sustainable analytical devices and the use of fully environmentally friendly materials. Many efforts are still needed to achieve these goals in PEC analytical systems.

BIBLIOGRAPHY

1. SAID, K. A. M.; ISMAIL, A. F.; KARIM, Z. A.; ABDULLAH, M. S.; HAFEEZ, A. A review of technologies for the phenolic compounds recovery and phenol removal from wastewater. **Process Safety and Environmental Protection**, Amsterdam, v. 151, p. 257-289, 2021.

2. AL BSOUL, A.; HAILAT, M.; ABDELHAY, A.; TAWALBEH, M.; AL-OTHMAN, A.; AL-KHARABSHEH, I. N.; AL-TAANI, A. A. Efficient removal of phenol compounds from water environment using *Ziziphus* leaves adsorbent. **Science of the Total Environment**, Amsterdam, v. 761, p. 143229, 2021.

3. FU, S.; ZHU, Y.; ZHANG, Y.; ZHANG, M.; ZHANG, Y.; QIAO, L.; YIN, N.; SONG, K.; LIU, M.; WANG, D. Recent advances in carbon nanomaterials-based electrochemical sensors for phenolic compounds detection. **Microchemical Journal**, Amsterdam, v. 171, p. 106776, 2021.

4. SIVAGAMI, K.; ANAND, D.; DIVYAPRIYA, G.; NAMBI, I. Treatment of petroleum oil spill sludge using the combined ultrasound and fenton oxidation process. **Ultrasonics Sonochemistry**, Amsterdam, v. 51, p. 340-349, 2019.

5. SINGH, S.; MISHRA, R.; SHARMA, R. S.; MISHRA, V. Phenol remediation by peroxidase from an invasive mesquite: turning an environmental wound into wisdom. **Journal of Hazardous Materials**, Amsterdam, v. 334, p. 201-211, 2017.

6. POPIOLEK, I.; POREBSKI, G. Adverse events associated with analgesics: a focus on paracetamol use. *In*: RAJENDRAM, R.; PATEL, V.B.; PREEDY, V.R.; MARTIN, C.R. (ed.). **Treatments, mechanisms, and adverse reactions of anesthetics and analgesics**. *E-book:* Academic Press, 2022. Cap. 28, p. 309-317. Disponível em: https://doi.org/10.1016/B978-0-12-820237-1.00028-4. Acesso em: 15 ago. 2021.

7. DOMINGO, J. L.; MARQUÈS, M.; NADAL, M.; SCHUHMACHER, M. Health risks for the population living near petrochemical industrial complexes. 1. cancer risks: a review of the scientific literature. **Environmental Research**, San Diego, v. 186, p. 109495, 2020.

8. HANAFI, M. F.; SAPAWE, N. A review on the water problem associate with organic pollutants derived from phenol, methyl orange, and remazol brilliant blue dyes. **Materials Today: proceedings**, London, v. 31, p. A141-A150, 2020.

9. LAN, S.; WANG, X.; LIU, Q.; BAO, J.; YANG, M.; FA, H.; HOU, C.; HUO, D. Fluorescent sensor for indirect measurement of methyl parathion based on alkaline-induced hydrolysis using N-doped carbon dots. **Talanta**, Amsterdam, v. 192, p. 368-373, 2019.

10. LIAO, X.; CAO, J.; HU, Y.; ZHANG, C.; HU, L. Mechanism of unactivated peroxymonosulfate-induced degradation of methyl parathion: kinetics and transformation pathway. **Chemosphere**, Oxford, v. 284, p. 131332, 2021.

11. ENGUITA, F. J.; LEITÃO, A. L. Hydroquinone: environmental pollution, toxicity, and microbial answers. **BioMed Research International**, London, v. 2013, p. 542168, 2013.

12. SONG, H.; CHEN, T. S. P-aminophenol-induced liver toxicity: tentative evidence of a role for acetaminophen. **Journal of Biochemical and Molecular Toxicology**, Hoboken, v. 15, n. 1, p. 34-40, 2001.

13. OTHMANI, A.; MAGDOULI, S.; KUMAR, P. S.; KAPOOR, A.; CHELLAM, P. V.; GÖKKUŞ, Ö. Agricultural waste materials for adsorptive removal of phenols, chromium (VI) and cadmium (II) from wastewater: a review. **Environmental Research**, San Diego, v. 204, p. 111916, 2022.

14. PATEL, H.; VASHI, R. T. **Characterization and treatment of textile wastewater**. Boston: Elsevier, 2015. p. 21-71.

15. ANNACHHATRE, A. P.; GHEEWALA, S. H. Biodegradation of chlorinated phenolic compounds. **Biotechnology Advances**, Oxford, v. 14, n. 1, p. 35-56, 1996.

16. ENVIROMENTAL PROTECTION AGENCY. **Phenol**. 2000. Disponível em: https://www.epa.gov/sites/default/files/2016-09/documents/phenol.pdf. Acesso em: 25 ago. 2021.

17. CAO, J.; XIE, Q.; DI, H.; LIANG, Y.; MA, G.; YI, Z.; ZHANG, P.; FU, P.; LI, J. Molecular complex based dispersive liquid–liquid microextraction for simultaneous HPLC determination of eight phenolic compounds in water samples. **Journal of Molecular Liquids**, Amsterdam, v. 309, p. 113115, 2020.

18. JAVADI, T.; FARAJMAND, B.; YAFTIAN, M. R.; ZAMANI, A. Homogenizer assisted dispersive liquid-phase microextraction for the extraction-enrichment of phenols from aqueous samples and determination by gas chromatography. **Journal of Chromatography A**, Amsterdam, v. 1614, p. 460733, 2020.

19. ZHU, W.; ZHAO, N. J.; YANG, R. F.; CHEN, Y. N.; CHEN, X. W.; YIN, G. F.; LIU, J. G.; LIU, W. Q. Simultaneous measurement of phenols by three-way fluorescence spectroscopy: a comparison of N-PLS/RBL, U-PLS/RBL and PARAFAC. **Spectrochimica Acta Part A:** molecular and biomolecular spectroscopy, Oxford, v. 239, p. 118511, 2020.

20. HUSSAIN, C. M.; KEÇILI, R. Separation techniques for environmental analysis. *In*: **Modern Environmental Analysis Techniques for Pollutants**. *E-book*: Elsevier, 2020. cap. 7, p. 163-198. Disponível em: https://doi.org/10.1016/B978-0-12-816934-6.00007-2. Acesso em: 03 set. 2021.

21. CHEN, X.; GUO, Z.; WANG, Y.; LIU, Y.; XU, Y.; LIU, J.; LI, Z.; ZHAO, J. Temperature sensitive polymer-dispersive liquid–liquid microextraction with gas chromatography–mass spectrometry for the determination of phenols. **Journal of Chromatography A**, Amsterdam, v. 1592, p. 183-187, 2019.

22. YADAV, N.; GARG, V. K.; CHHILLAR, A. K.; RANA, J. S. Detection and remediation of pollutants to maintain ecosustainability employing nanotechnology: a review. **Chemosphere**, Oxford, v. 280, p. 130792, 2021.

23. FU, S.; ZHU, Y.; ZHANG, Y.; ZHANG, M.; ZHANG, Y.; QIAO, L.; YIN, N.; SONG, K.; LIU, M.; WANG, D. Recent advances in carbon nanomaterials-based electrochemical sensors for phenolic compounds detection. **Microchemical Journal**, Amsterdam, v. 171, p. 106776, 2021.

24. CAETANO, F. R.; CARNEIRO, E. A.; AGUSTINI, D.; FIGUEIREDO-FILHO, L. C. S.; BANKS, C. E.; BERGAMINI, M. F.; MARCOLINO-JUNIOR, L. H. Combination of electrochemical biosensor and textile threads: a microfluidic device for phenol determination in tap water. **Biosensors and Bioelectronics**, Oxford, v. 99, p. 382-388, 2018.

25. MEI, L. P.; FENG, J. J.; WU, L.; ZHOU, J. Y.; CHEN, J. R.; WANG, A. J. Novel phenol biosensor based on laccase immobilized on reduced graphene oxide supported palladium–copper alloyed nanocages. **Biosensors and Bioelectronics**, Oxford, v. 74, p. 347-352, 2015.

26. WANG, B.; OKOTH, O. K.; YAN, K.; ZHANG, J. A highly selective electrochemical sensor for 4-chlorophenol determination based on molecularly imprinted polymer and PDDA-functionalized graphene. **Sensors and Actuators B:** chemical, Lausanne, v. 236, p. 294-303, 2016.

27. CHEN, W.; LI, R.; LI, Z.; YANG, Y.; ZHU, H.; LIU, J. Promising copper oxide-histidine functionalized graphene quantum dots hybrid for electrochemical detection of hydroquinone. **Journal of Alloys and Compounds**, Lausanne, v. 777, p. 1001-1009, 2019.

28. LI, C.; WU, Z.; YANG, H.; DENG, L.; CHEN, X. Reduced graphene oxide-cyclodextrin-chitosan electrochemical sensor: effective and simultaneous determination of o- and p-nitrophenols. **Sensors and Actuators B:** chemical, Lausanne, v. 251, p. 446-454, 2017.

29. GUO, H.; FAN, T.; YAO, W.; YANG, W.; WU, N.; LIU, H.; WANG, M.; YANG, W. Simultaneous determination of 4-aminophenol and acetaminophen based on high electrochemical performance of ZIF-67/MWCNT-COOH/Nafion composite. **Microchemical Journal**, Amsterdam, v. 158, p. 105262, 2020.

30. XIE, Y.; LIU, T.; CHU, Z.; JIN, W. Recent advances in electrochemical enzymatic biosensors based on regular nanostructured materials. **Journal of Electroanalytical Chemistry**, Lausanne, v. 893, p. 115328, 2021.

31. HASHIM, H. S.; FEN, Y. W.; OMAR, N. A. S.; FAUZI, N. I. M.; DANIYAL, W. M. E. M. M. Recent advances of priority phenolic compounds detection using phenol oxidases-based electrochemical and optical sensors. **Measurement**, Oxford, v. 184, p. 109855, 2021.

32. FARTAS, F. M.; ABDULLAH, J.; YUSOF, N. A.; SULAIMAN, Y.; SAIMAN, M. I. Biosensor based on tyrosinase immobilized on graphene-decorated gold nanoparticle/chitosan for phenolic detection in aqueous. **Sensors**, Basel, v. 17, n. 5, p. 1132, 2017.

33. ZHANG, Y.; ZHANG, J.; WU, H.; GUO, S.; ZHANG, J. Glass carbon electrode modified with horseradish peroxidase immobilized on partially reduced graphene oxide for detecting phenolic compounds. **Journal of Electroanalytical Chemistry**, Lausanne, v. 681, p. 49-55, 2012.

34. LOU, C.; JING, T.; ZHOU, J.; TIAN, J.; ZHENG, Y.; WANG, C.; ZHAO, Z.; LIN, J.; LIU, H.; ZHAO, C.; GUO, Z. Laccase immobilized polyaniline/magnetic graphene composite electrode for detecting hydroquinone. **International Journal of Biological Macromolecules**, Amsterdam, v. 149, p. 1130-1138, 2020.

35. SCHOLZ, F. Voltammetric techniques of analysis: the essentials. **ChemTexts**, New York, v. 1, n. 4, p. 17, 2015.

36. KALAMBATE, P. K.; RAO, Z.; DHANJAI; WU, J.; SHEN, Y.; BODDULA, R.; HUANG, Y. Electrochemical (bio) sensors go green. **Biosensors and Bioelectronics**, Oxford, v. 163, p. 112270, 2020.

37. KANG, Z.; YAN, X.; WANG, Y.; ZHAO, Y.; BAI, Z.; LIU, Y.; ZHAO, K.; CAO, S.; ZHANG, Y. Self-powered photoelectrochemical biosensing platform based on Au NPs@ZnO nanorods array. **Nano Research**, Beijing, v. 9, n. 2, p. 344-352, 2016.

38. GERISCHER, H. **Advances in electrochemistry and electrochemical engineering**. New York: P. Delahay Interscience, 1961. 326p.

39. PETER, L. M. Photoelectrochemistry: from basic principles to photocatalysis. *In*: SCHNEIDER, J.; BAHNEMANN, D.; YE, J.; PUMA, G.L.; DIONYSIOU, D.D. (ed.). **Photocatalysis:** fundamentals and perspectives. *E-book*: The Royal Society of Chemistry, 2016. Cap. 1, p. 1-28. Disponível em: https://doi.org/10.1039/9781782622338-00001. Acesso em: 03 set. 2021.

40. SHU, J.; TANG, D. Recent advances in photoelectrochemical sensing: from engineered photoactive materials to sensing devices and detection modes. **Analytical Chemistry**, Washington, v. 92, n. 1, p. 363-377, 2020.

41. ZHANG, Z. X.; ZHAO, C. Z. Progress of photoelectrochemical analysis and sensors. **Chinese Journal of Analytical Chemistry**, Beijing, v. 41, n. 3, p. 436-444, 2013.

42. GOKTAS, S.; GOKTAS, A. A comparative study on recent progress in efficient ZnO based nanocomposite and heterojunction photocatalysts: a review. **Journal of Alloys and Compounds**, Lausanne, v. 863, p. 158734, 2021.

43. MORRISON, S. R. **Electrochemistry at semiconductor and oxidized metal electrodes**. New York: Springer, 1980. 416p.

44. WOOD, D. L.; TAUC, J. Weak absorption tails in amorphous semiconductors. **Physical Review B**, College Park, v. 5, p. 3144-3151, 1972.

45. SHI, L.; YIN, Y.; ZHANG, L.-C.; WANG, S.; SILLANPÄÄ, M.; SUN, H. Design and engineering heterojunctions for the photoelectrochemical monitoring of environmental pollutants: A review. **Applied Catalysis B:** environmental, Amsterdam, v. 248, p. 405-422, 2019.

46. LI, J.; XIONG, P.; TANG, J.; LIU, L.; GAO, S.; ZENG, Z.; XIE, H.; TANG, D.; ZHUANG, J. Biocatalysis-induced formation of BiOBr/Bi_2S_3 semiconductor heterostructures: a highly efficient strategy for establishing sensitive photoelectrochemical sensing system for organophosphorus pesticide detection. **Sensors and Actuators B:** chemical, Lausanne, v. 331, p. 129451, 2021.

47. YUE, Z.; LISDAT, F.; PARAK, W. J.; HICKEY, S. G.; TU, L.; SABIR, N.; DORFS, D.; BIGALL, N. C. Quantum-dot-based photoelectrochemical sensors for chemical and biological detection. **ACS Applied Materials & Interfaces**, Washington, v. 5, n. 8, p. 2800-2814, 2013.

48. REGHUNATH, S.; PINHEIRO, D.; KR, S. D. A review of hierarchical nanostructures of TiO_2: advances and applications. **Applied Surface Science Advances**, Amsterdam, v. 3, p. 100063, 2021.

49. ANI, I. J.; AKPAN, U. G.; OLUTOYE, M. A.; HAMEED, B. H. Photocatalytic degradation of pollutants in petroleum refinery wastewater by TiO_2- and ZnO-based photocatalysts: recent development. **Journal of Cleaner Production**, Oxford, v. 205, p. 930-954, 2018.

50. WANG, H.; ZHANG, L.; CHEN, Z.; HU, J.; LI, S.; WANG, Z.; LIU, J.; WANG, X. Semiconductor heterojunction photocatalysts: design, construction, and photocatalytic performances. **Chemical Society Reviews**, Cambridge, v. 43, n. 15, p. 5234-5244, 2014.

51. BLASKIEVICZ, S. F.; MASCARO, L. H.; ZHAO, Y.; MARKEN, F. Semiconductor photoelectroanalysis and photobioelectroanalysis: a perspective. **TrAC Trends in Analytical Chemistry**, Oxford, v. 135, p. 116154, 2021.

52. ZHU, L.; LI, H.; LIU, Z.; XIA, P.; XIE, Y.; XIONG, D. Synthesis of the 0D/3D CuO/ZnO heterojunction with enhanced photocatalytic activity. **Journal of Physical Chemistry C**, Washington, v. 122, n. 17, p. 9531-9539, 2018.

53. ZHANG, X.; LI, S.; JIN, X.; ZHANG, S. A new photoelectrochemical aptasensor for the detection of thrombin based on functionalized graphene and CdSe nanoparticles multilayers. **Chemical Communications**, Cambridge, v. 47, n. 17, p. 4929-4931, 2011.

54. DI BARTOLOMEO, A. Graphene Schottky diodes: an experimental review of the rectifying graphene/semiconductor heterojunction. **Physics Reports**, Amsterdam, v. 606, p. 1-58, 2016.

55. ZHOU, F.; JING, W.; XU, Y.; CHEN, Z.; JIANG, Z.; WEI, Z. Performance enhancement of ZnO nanorod-based enzymatic glucose sensor via reduced graphene oxide deposition and UV irradiation. **Sensors and Actuators B:** chemica**l**, Lausanne, v. 284, p. 377-385, 2019.

56. MENDONÇA, C. D.; KHAN, S. U.; RAHEMI, V.; VERBRUGGEN, S. W.; MACHADO, S. A. S.; DE WAEL, K. Surface plasmon resonance-induced visible light photocatalytic TiO_2 modified with AuNPs for the quantification of hydroquinone. **Electrochimica Acta**, Oxford, v. 389, p. 138734, 2021.

57. TADA, H.; MITSUI, T.; KIYONAGA, T.; AKITA, T.; TANAKA, K. All-solid-state Z-scheme in CdS–Au–TiO_2 three-component nanojunction system. **Nature Materials**, Berlin, v. 5, n. 10, p. 782-786, 2006.

58. ZHANG, Y. C.; YANG, M.; ZHANG, G.; DIONYSIOU, D. D. HNO_3-involved one-step low temperature solvothermal synthesis of N-doped TiO_2 nanocrystals for efficient photocatalytic reduction of Cr(VI) in water. **Applied Catalysis B:** environmental, Amsterdam, v. 142-143, p. 249-258, 2013.

59. LI, H.; LI, J.; XU, Q.; YANG, Z.; HU, X. A derivative photoelectrochemical sensing platform for 4-nitrophenolate contained organophosphates pesticide based on carboxylated perylene sensitized nano-TiO_2. **Analytica Chimica Acta**, Amsterdam, v. 766, p. 47-52, 2013.

60. YAN, P.; JIANG, D.; TIAN, Y.; XU, L.; QIAN, J.; LI, H.; XIA, J.; LI, H. A sensitive signal-on photoelectrochemical sensor for tetracycline determination using visible-light-driven flower-like CN/BiOBr composites. **Biosensors and Bioelectronics**, Oxford, v. 111, p. 74-81, 2018.

61. PRADO, T. M.; BADARÓ, C. C.; MACHADO, R. G.; FADINI, P. S.; FATIBELLO-FILHO, O.; MORAES, F. C. Using bismuth vanadate/copper oxide nanocomposite as photoelectrochemical sensor for naproxen determination in sewage. **Electroanalysis**, Weinheim, v. 32, n. 9, p. 1930-1937, 2020.

62. PRADO, T. M.; CARRICO, A.; CINCOTTO, F. H.; FATIBELLO-FILHO, O.; MORAES, F. C. Bismuth vanadate/graphene quantum dot: a new nanocomposite for photoelectrochemical determination of dopamine. **Sensors and Actuators B:** Chemical, Lausanne, v. 285, p. 248-253, 2019.

63. WANG, G. L.; JIAO, H. J.; LIU, K. L.; WU, X. M.; DONG, Y. M.; LI, Z. J.; ZHANG, C. A novel strategy for the construction of photoelectrochemical sensors based on quantum dots and electron acceptor: the case of dopamine detection. **Electrochemistry Communications**, New York, v. 41, p. 47-50, 2014.

64. CAO, L.; LI, Z.; JIA, R.; CHEN, L.; WU, Y.; DI, J. Sensitive photoelectrochemical determination of ciprofloxacin using an indium tin oxide photoelectrode modified with small gold nanoparticles. **Analytical Letters**, Philadelphia, v. 53, n. 9, p. 1472-1488, 2020.

65. LI, X.; ZHENG, Z.; LIU, X.; ZHAO, S.; LIU, S. Nanostructured photoelectrochemical biosensor for highly sensitive detection of organophosphorous pesticides. **Biosensors and Bioelectronics**, Oxford, v. 64, p. 1-5, 2015.

66. ZHAO, W.-W.; XU, J.-J.; CHEN, H.-Y. Photoelectrochemical enzymatic biosensors. **Biosensors and Bioelectronics**, Oxford, v. 92, p. 294-304, 2017.

67. FAN, L.; ZHAO, G.; SHI, H.; LIU, M.; WANG, Y.; KE, H. A femtomolar level and highly selective 17β-estradiol photoelectrochemical aptasensor applied in environmental water samples analysis. **Environmental Science & Technology**, Washington, v. 48, n. 10, p. 5754-5761, 2014.

68. QIAO, Y.; LI, J.; LI, H.; FANG, H.; FAN, D.; WANG, W. A label-free photoelectrochemical aptasensor for bisphenol A based on surface plasmon resonance of gold nanoparticle-sensitized ZnO nanopencils. **Biosensors and Bioelectronics**, Oxford, v. 86, p. 315-320, 2016.

69. WANG, P.; DAI, W.; GE, L.; YAN, M.; GE, S.; YU, J. Visible light photoelectrochemical sensor based on Au nanoparticles and molecularly imprinted poly(o-phenylenediamine)-modified TiO_2 nanotubes for specific and sensitive detection chlorpyrifos. **Analyst**, Cambridge, v. 138, n. 3, p. 939-945, 2013.

70. CHEN, K.; LIU, M.; ZHAO, G.; SHI, H.; FAN, L.; ZHAO, S. Fabrication of a novel and simple microcystin-LR photoelectrochemical sensor with high sensitivity and selectivity. **Environmental Science & Technology**, Washington, v. 46, n. 21, p. 11955-11961, 2012.

71. SUN, X.; GAO, C.; ZHANG, L.; YAN, M.; YU, J.; GE, S. Photoelectrochemical sensor based on molecularly imprinted film modified hierarchical branched titanium dioxide nanorods for chlorpyrifos detection. **Sensors and Actuators B:** chemical, Lausanne, v. 251, p. 1-8, 2017.

72. GONG, J.; WANG, X.; LI, X.; WANG, K. Highly sensitive visible light activated photoelectrochemical biosensing of organophosphate pesticide using biofunctional crossed bismuth oxyiodide flake arrays. **Biosensors and Bioelectronics**, Oxford, v. 38, n. 1, p. 43-49, 2012.

73. SHANMUGAM, S. T.; TRASHIN, S.; DE WAEL, K. Singlet oxygen-based photoelectrochemical detection of DNA. **Biosensors and Bioelectronics**, Oxford, v. 195, p. 113652, 2022.

74. FAN, Z.; FAN, L.; SHUANG, S.; DONG, C. Highly sensitive photoelectrochemical sensing of bisphenol A based on zinc phthalocyanine/TiO_2 nanorod arrays. **Talanta**, Amsterdam, v. 189, p. 16-23, 2018.

75. YAN, P.; JIANG, D.; LI, H.; BAO, J.; XU, L.; QIAN, J.; CHEN, C.; XIA, J. $BiPO_4$ nanocrystal/BiOCl nanosheet heterojunction as the basis for a photoelectrochemical 4-chlorophenol sensor. **Sensors and Actuators B:** chemical, Lausanne, v. 279, p. 466-475, 2019.

76. TRASHIN, S.; RAHEMI, V.; RAMJI, K.; NEVEN, L.; GORUN, S. M.; DE WAEL, K. Singlet oxygen-based electrosensing by molecular photosensitizers. **Nature Communications**, Berlin, v. 8, n. 1, p. 16108, 2017.

77. NEVEN, L.; SHANMUGAM, S. T.; RAHEMI, V.; TRASHIN, S.; SLEEGERS, N.; CARRIÓN, E. N.; GORUN, S. M.; DE WAEL, K. Optimized photoelectrochemical detection of essential drugs bearing phenolic groups. **Analytical Chemistry**, Washington, v. 91, n. 15, p. 9962-9969, 2019.

78. RAHEMI, V.; TRASHIN, S.; HAFIDEDDINE, Z.; VAN DOORSLAER, S.; MEYNEN, V.; GORTON, L.; DE WAEL, K. Amperometric flow-injection analysis of phenols induced by reactive oxygen species generated under daylight irradiation of titania impregnated with horseradish peroxidase. **Analytical Chemistry**, Washington, v. 92, n. 5, p. 3643-3649, 2020.

79. MENDONÇA, C. D.; RAHEMI, V.; HEREIJGERS, J.; BREUGELMANS, T.; MACHADO, S. A. S.; DE WAEL, K. Integration of a photoelectrochemical cell in a flow system for quantification of 4-aminophenol with titanium dioxide. **Electrochemistry Communications**, New York, v. 117, p. 106767, 2020.

80. WANG, R.; YAN, K.; WANG, F.; ZHANG, J. A highly sensitive photoelectrochemical sensor for 4-aminophenol based on CdS-graphene nanocomposites and molecularly imprinted polypyrrole. **Electrochimica Acta**, Oxford, v. 121, p. 102-108, 2014.

81. YAN, K.; YANG, Y.; ZHU, Y.; ZHANG, J. Highly selective self-powered sensing platform for p-nitrophenol detection constructed with a photocathode-based photocatalytic fuel cell. **Analytical Chemistry**, Washington, v. 89, n. 17, p. 8599-8603, 2017.

82. WANG, J.; LIU, Z. Recent advances in two-dimensional layered materials for photoelectrochemical sensing. **TrAC Trends in Analytical Chemistry**, Oxford, v. 133, p. 116089, 2020.

83. MUNTEANU, F.-D.; LINDGREN, A.; EMNÉUS, J.; GORTON, L.; RUZGAS, T.; CSÖREGI, E.; CIUCU, A.; VAN HUYSTEE, R. B.; GAZARYAN, I. G.; LAGRIMINI, L. M. Bioelectrochemical monitoring of phenols and aromatic amines in flow injection using novel plant peroxidases. **Analytical Chemistry**, Washington, v. 70, n. 13, p. 2596-2600, 1998.

84. HAGHIGHI, B.; JAROSZ-WILKOŁAZKA, A.; RUZGAS, T.; GORTON, L.; LEONOWICZ, A. Characterization of graphite electrodes modified with laccases from *Trametes hirsuta* and *Cerrena unicolor* and their use for flow injection amperometric determination of some phenolic compounds. **International Journal of Environmental Analytical Chemistry**, Oxford, v. 85, n. 9-11, p. 753-770, 2005.

85. YEH, W.-L.; KUO, Y.-R.; CHENG, S.-H. Voltammetry and flow-injection amperometry for indirect determination of dopamine. **Electrochemistry Communications**, New York, v. 10, n. 1, p. 66-70, 2008.

86. WANG, Z.; TANG, Y.; HU, H.; XING, L.; ZHANG, G.; GAO, R. Chemiluminescence detection of hydroquinone with flow-injection analysis of luminol-hydrogen peroxide system catalyzed by Jacobsen's catalyst. **Journal of Luminescence**, Amsterdam, v. 145, p. 818-823, 2014.

87. VAKH, C.; EVDOKIMOVA, E.; POCHIVALOV, A.; MOSKVIN, L.; BULATOV, A. A novel flow injection chemiluminescence method for automated and miniaturized determination of phenols in smoked food samples. **Food Chemistry**, Oxford, v. 237, p. 929-935, 2017.

88. UPAN, J.; REANPANG, P.; CHAILAPAKUL, O.; JAKMUNEE, J. Flow injection amperometric sensor with a carbon nanotube modified screen printed electrode for determination of hydroquinone. **Talanta**, Amsterdam, v. 146, p. 766-771, 2016.

89. DIAS, A. C. B.; FIGUEIREDO, E. C.; GRASSI, V.; ZAGATTO, E. A. G.; ARRUDA, M. A. Z. Molecularly imprinted polymer as a solid phase extractor in flow analysis. **Talanta**, Amsterdam, v. 76, n. 5, p. 988-996, 2008.

90. SANTOS, W. D. J. R.; LIMA, P. R.; TARLEY, C. R. T.; KUBOTA, L. T. A catalytically active molecularly imprinted polymer that mimics peroxidase based on hemin: application to the determination of p-aminophenol. **Analytical and Bioanalytical Chemistry**, Heidelberg, v. 389, n. 6, p. 1919-1929, 2007.

91. WONG, A.; SOTOMAYOR, M. D. P. T. Determination of carbofuran and diuron in FIA system using electrochemical sensor modified with organometallic complexes and graphene oxide. **Journal of Electroanalytical Chemistry**, Lausanne, v. 731, p. 163-171, 2014.

92. LIU, J.; CHEN, H.; LIN, Z.; LIN, J.-M. Preparation of surface imprinting polymer capped mn-doped zns quantum dots and their application for chemiluminescence detection of 4-nitrophenol in tap water. **Analytical Chemistry**, Washington, v. 82, n. 17, p. 7380-7386, 2010.

93. GIMENES, D. T.; SANTOS, W. T. P. D.; MUNOZ, R. A. A.; RICHTER, E. M. Internal standard in flow injection analysis with amperometric detection. **Electrochemistry Communications**, New York, v. 12, n. 2, p. 216-218, 2010.

94. KUMAR, P.; KIM, K.-H.; DEEP, A. Recent advancements in sensing techniques based on functional materials for organophosphate pesticides. **Biosensors and Bioelectronics**, Oxford, v. 70, p. 469-481, 2015.

95. ZHANG, S.; LI, L.; ZHAO, H. A portable photoelectrochemical probe for rapid determination of chemical oxygen demand in wastewaters. **Environmental Science & Technology**, Washington, v. 43, n. 20, p. 7810-7815, 2009.

96. LAZAR, M. A.; DAOUD, W. A. Achieving selectivity in TiO_2-based photocatalysis. **RSC Advances**, Cambridge, v. 3, n. 13, p. 4130-4140, 2013.

97. WANG, Y.; ZU, M.; LI, S.; BUTBUREE, T.; WANG, L.; PENG, F.; ZHANG, S. Dual modification of TiO_2 nanorods for selective photoelectrochemical detection of organic compounds. **Sensors and Actuators B:** chemical, Lausanne, v. 250, p. 307-314, 2017.

98. YAN, K.; WU, J.; JI, W.; WU, J.; ZHANG, J. Integration of redox cycling in a photoelectrochemical sensing platform for tyrosinase activity evaluation. **Electrochemistry Communications**, New York, v. 108, p. 106555, 2019.

99. PELAEZ, M.; NOLAN, N. T.; PILLAI, S. C.; SEERY, M. K.; FALARAS, P.; KONTOS, A. G.; DUNLOP, P. S. M.; HAMILTON, J. W. J.; BYRNE, J. A.; O'SHEA, K.; ENTEZARI, M. H.; DIONYSIOU, D. D. A review on the visible light active titanium dioxide photocatalysts for environmental applications. **Applied Catalysis B:** environmental, Amsterdam, v. 125, p. 331-349, 2012.

100. SZCZEPANIK, B. Photocatalytic degradation of organic contaminants over clay-TiO_2 nanocomposites: a review. **Applied Clay Science**, Amsterdam, v. 141, p. 227-239, 2017.

101. NAKATA, K.; FUJISHIMA, A. TiO_2 photocatalysis: design and applications. **Journal of Photochemistry and Photobiology C:** photochemistry reviews, Amsterdam, v. 13, n. 3, p. 169-189, 2012.

102. ZHANG, S.; ZHANG, S.; PENG, B.; WANG, H.; YU, H.; WANG, H.; PENG, F. High performance hydrogenated TiO_2 nanorod arrays as a photoelectrochemical sensor for organic compounds under visible light. **Electrochemistry Communications**, New York, v. 40, p. 24-27, 2014.

103. WANG, Y.; HONG, C. S. Effect of hydrogen peroxide, periodate and persulfate on photocatalysis of 2-chlorobiphenyl in aqueous TiO_2 suspensions. **Water Research**, Oxford, v. 33, n. 9, p. 2031-2036, 1999.

104. RAHMAN, M. M.; HUSSEIN, M. A.; ALAMRY, K. A.; AL-SHEHRY, F. M.; ASIRI, A. M. Polyaniline/graphene/carbon nanotubes nanocomposites for sensing environmentally hazardous 4-aminophenol. **Nano-Structures & Nano-Objects**, Amsterdam, v. 15, p. 63-74, 2018.

105. KAUR, B.; SRIVASTAVA, R. Simultaneous electrochemical determination of nanomolar concentrations of aminophenol isomers using nanocrystalline zirconosilicate modified carbon paste electrode. **Electrochimica Acta**, Oxford, v. 141, p. 61-71, 2014.

106. ZHANG, S. S.; LIU, H. X.; YUAN, Z. B. Comparison of high-performance capillary electrophoresis and liquid chromatography on analysis of zinc 5-aminosalicylate dihydrate and related materials. **Journal of Chromatography B:** biomedical sciences and applications, Amsterdam, v. 705, n. 1, p. 165-170, 1998.

107. ZHONG, C.; HE, M.; LIAO, H.; CHEN, B.; WANG, C.; HU, B. Polydimethylsiloxane/covalent triazine frameworks coated stir bar sorptive extraction coupled with high performance liquid chromatography-ultraviolet detection for the determination of phenols in environmental water samples. **Journal of Chromatography A**, Amsterdam, v. 1441, p. 8-15, 2016.

108. ARCE, M. M.; SANLLORENTE, S.; ORTIZ, M. C.; SARABIA, L. A. Easy-to-use procedure to optimise a chromatographic method. application in the determination of bisphenol-A and phenol in toys by means of liquid chromatography with fluorescence detection. **Journal of Chromatography A**, Amsterdam, v. 1534, p. 93-100, 2018.

109. YANG, W. C.; YU, X. D.; YU, A. M.; CHEN, H.-Y. Study of a novel cationic calix[4]arene used as selectivity modifier in capillary electrophoresis with electrochemical detection. **Journal of Chromatography A**, Amsterdam, v. 910, n. 2, p. 311-318, 2001.

110. ZHANG, Q. L.; WU, L.; LV, C.; ZHANG, X. Y. A novel on-line gold nanoparticle-catalyzed luminol chemiluminescence detector for high-performance liquid chromatography. **Journal of Chromatography A**, Amsterdam, v. 1242, p. 84-91, 2012.

111. SCANDURRA, G.; ANTONELLA, A.; CIOFI, C.; SAITTA, G.; LANZA, M. Electrochemical detection of p-aminophenol by flexible devices based on multi-wall carbon nanotubes dispersed in electrochemically modified nafion. **Sensors**, Basel, v. 14, n. 5, p. 8926-8939, 2014.

112. JIAN, X.; LIU, X.; YANG, H.-M.; GUO, M. M.; SONG, X. L.; DAI, H. Y.; LIANG, Z. H. Graphene quantum dots modified glassy carbon electrode via electrostatic self-assembly strategy and its application. **Electrochimica Acta**, Oxford, v. 190, p. 455-462, 2016.

113. ZHU, G.; YI, Y.; LIU, Z.; LEE, H. J.; CHEN, J. Highly sensitive electrochemical sensing based on 2-hydroxypropyl-β-cyclodextrin-functionalized graphene nanoribbons. **Electrochemistry Communications**, New York, v. 66, p. 10-15, 2016.

114. FIASCHI, G.; COSENTINO, S.; PANDEY, R.; MIRABELLA, S.; STRANO, V.; MAIOLO, L.; GRANDJEAN, D.; LIEVENS, P.; SHACHAM-DIAMAND, Y. A novel gas-phase mono and bimetallic clusters decorated ZnO nanorods electrochemical sensor for 4-aminophenol detection. **Journal of Electroanalytical Chemistry**, Lausanne, v. 811, p. 89-95, 2018.

115. SHAIKSHAVALI, P.; REDDY, T. M.; PALAKOLLU, V. N.; KARPOORMATH, R.; RAO, Y. S.; VENKATAPRASAD, G.; GOPAL, T. V.; GOPAL, P. Multi walled carbon nanotubes supported CuO-Au hybrid nanocomposite for the effective application towards the electrochemical determination of acetaminophen and 4-aminophenol. **Synthetic Metals**, Lausanne, v. 252, p. 29-39, 2019.

116. ZHANG, D.; QIAN, J.; YI, Y.; KINGSFORD, O. J.; ZHU, G. Nitrogen-doped hollow carbon nanospheres wrapped with MoS_2 nanosheets for simultaneous electrochemical determination of acetaminophen and 4-aminophenol. **Journal of Electroanalytical Chemistry**, Lausanne, p. 113229, 2019.

117. LINSEBIGLER, A. L.; LU, G.; YATES, J. T. Photocatalysis on TiO_2 surfaces: principles, mechanisms, and selected results. **Chemical Reviews**, Washington, v. 95, n. 3, p. 735-758, 1995.

118. KURBANOGLU, S.; UNAL, M. A.; OZKAN, S. A. Recent developments on electrochemical flow injection in pharmaceuticals and biologically important compounds. **Electrochimica Acta**, Oxford, v. 287, p. 135-148, 2018.

119. ŘUŽIČKA, J.; HANSEN, E. H. Flow injection analyses: part I. a new concept of fast continuous flow analysis. **Analytica Chimica Acta**, Amsterdam, v. 78, n. 1, p. 145-157, 1975.

120. FUJISHIMA, A.; ZHANG, X.; TRYK, D. A. TiO_2 photocatalysis and related surface phenomena. **Surface Science Reports**, Amsterdam, v. 63, n. 12, p. 515-582, 2008.

121. TROJANOWICZ, M.; SZEWCZYNSKA, M.; WCISLO, M. Electroanalytical flow measurements–recent advances. **Electroanalysis**, Weinheim, v. 15, n. 5-6, p. 347-365, 2003.

122. MIAO, F.; GAO, M.; YU, X.; XIAO, P.; WANG, M.; WANG, Y.; WANG, S.; WANG, X. TiO_2 electrocatalysis via three-electron oxygen reduction for highly efficient generation of hydroxyl radicals. **Electrochemistry Communications**, New York, v. 113, p. 106687, 2020.

123. BULEANDRA, M.; RABINCA, A. A.; MIHAILCIUC, C.; BALAN, A.; NICHITA, C.; STAMATIN, I.; CIUCU, A. A. Screen-printed prussian blue modified electrode for simultaneous detection of hydroquinone and catechol. **Sensors and Actuators B:** chemical, Lausanne, v. 203, p. 824-832, 2014.

124. YAO, Y.; LIU, Y.; YANG, Z. A novel electrochemical sensor based on a glassy carbon electrode modified with Cu–MWCNT nanocomposites for determination of hydroquinone. **Analytical Methods**, Cambridge, v. 8, n. 12, p. 2568-2575, 2016.

125. ZHOU, J.; LI, X.; YANG, L.; YAN, S.; WANG, M.; CHENG, D.; CHEN, Q.; DONG, Y.; LIU, P.; CAI, W.; ZHANG, C. The Cu-MOF-199/single-walled carbon nanotubes modified electrode for simultaneous determination of hydroquinone and catechol with extended linear ranges and lower detection limits. **Analytica Chimica Acta**, Amsterdam, v. 899, p. 57-65, 2015.

126. BLOOMFIELD, M. S. A sensitive and rapid assay for 4-aminophenol in paracetamol drug and tablet formulation, by flow injection analysis with spectrophotometric detection. **Talanta**, Amsterdam, v. 58, n. 6, p. 1301-1310, 2002.

127. XU, H.; DUAN, C.-F.; ZHANG, Z.-F.; CHEN, J.-Y.; LAI, C.-Z.; LIAN, M.; LIU, L.-J.; CUI, H. Flow injection determination of p-aminophenol at trace level using inhibited luminol–dimethylsulfoxide–NaOH–EDTA chemiluminescence. **Water Research**, Oxford, v. 39, n. 2, p. 396-402, 2005.

128. VERBRUGGEN, S. W. TiO_2 photocatalysis for the degradation of pollutants in gas phase: From morphological design to plasmonic enhancement. **Journal of Photochemistry and Photobiology C:** photochemistry reviews, Amsterdam, v. 24, p. 64-82, 2015.

129. ASLAM, M.; ABDULLAH, A. Z.; RAFATULLAH, M. Recent development in the green synthesis of titanium dioxide nanoparticles using plant-based biomolecules for environmental and antimicrobial applications. **Journal of Industrial and Engineering Chemistry**, New York, v. 98, p. 1-16, 2021.

130. RIAZ, S.; PARK, S.-J. An overview of TiO_2-based photocatalytic membrane reactors for water and wastewater treatments. **Journal of Industrial and Engineering Chemistry**, New York, v. 84, p. 23-41, 2020.

131. ZHOU, Y.; ZHANG, L.; TAO, S. Porous TiO_2 with large surface area is an efficient catalyst carrier for the recovery of wastewater containing an ultrahigh concentration of dye. **RSC Advances**, Cambridge, v. 8, n. 7, p. 3433-3442, 2018.

132. CHEN, D.; CHENG, Y.; ZHOU, N.; CHEN, P.; WANG, Y.; LI, K.; HUO, S.; CHENG, P.; PENG, P.; ZHANG, R.; WANG, L.; LIU, H.; LIU, Y.; RUAN, R. Photocatalytic degradation of organic pollutants using TiO_2-based photocatalysts: a review. **Journal of Cleaner Production**, Oxford, v. 268, p. 121725, 2020.

133. QIU, Z.; SHU, J.; TANG, D. Near-infrared-to-ultraviolet light-mediated photoelectrochemical aptasensing platform for cancer biomarker based on core–shell $NaYF_4$:Yb,Tm@TiO_2 upconversion microrods. **Analytical Chemistry**, Washington, v. 90, n. 1, p. 1021-1028, 2018.

134. PEH, C. K. N.; WANG, X. Q.; HO, G. W. Increased photocatalytic activity of CuO/TiO_2 through broadband solar absorption heating under natural sunlight. **Procedia Engineering**, Amsterdam, v. 215, p. 171-179, 2017.

135. ZHANG, Y.; XU, M.; GAO, P.; GAO, W.; BIAN, Z.; JIA, N. Photoelectrochemical sensing of dopamine using gold-TiO_2 nanocomposites and visible-light illumination. **Microchimica Acta**, Wien, v. 186, n. 6, p. 326, 2019.

136. ZHAO, W. W.; XU, J. J.; CHEN, H.Y. Photoelectrochemical bioanalysis: the state of the art. **Chemical Society Reviews**, Cambridge, v. 44, n. 3, p. 729-741, 2015.

137. SINGH, J.; SAHU, K.; SATPATI, B.; SHAH, J.; KOTNALA, R. K.; MOHAPATRA, S. Facile synthesis, structural and optical properties of Au-TiO_2 plasmonic nanohybrids for photocatalytic applications. **Journal of Physics and Chemistry of Solids**, Oxford, v. 135, p. 109100, 2019.

138. CAI, G.; YU, Z.; REN, R.; TANG, D. Exciton–plasmon interaction between AuNPs/graphene nanohybrids and CdS quantum dots/TiO_2 for photoelectrochemical aptasensing of prostate-specific antigen. **ACS Sensors**, Washington, v. 3, n. 3, p. 632-639, 2018.

139. PARK, H.; PARK, Y.; KIM, W.; CHOI, W. Surface modification of TiO_2 photocatalyst for environmental applications. **Journal of Photochemistry and Photobiology C:** photochemistry reviews, Amsterdam, v. 15, p. 1-20, 2013.

140. BARBIERIKOVÁ, Z.; DVORANOVÁ, D.; BREZOVÁ, V.; DŽUNUZOVIĆ, E.; SREDOJEVIĆ, D. N.; LAZIĆ, V.; NEDELJKOVIĆ, J. M. Visible-light-responsive surface-modified TiO_2 powder with 4-chlorophenol: a combined experimental and DFT study. **Optical Materials**, Amsterdam, v. 89, p. 237-242, 2019.

141. HU, Z.; ZHAO, L.; LI, W.; WANG, S.; DONG, B. Ag nanoparticle-modified double-layer composite film based on P25/$NaLuF_4$:Yb^{3+}/Er^{3+} and flower TiO_2 for highly efficient dye-sensitized solar cells. **Applied Surface Science**, Amsterdam, v. 491, p. 286-293, 2019.

142. ZHANG, Z.; MA, Y.; BU, X.; WU, Q.; HANG, Z.; DONG, Z.; WU, X. Facile one-step synthesis of TiO_2/Ag/SnO_2 ternary heterostructures with enhanced visible light photocatalytic activity. **Scientific Reports**, Berlin, v. 8, n. 1, p. 10532, 2018.

143. WEI, F.; WANG, H.; RAN, W.; LIU, T.; LIU, X. Preparation of S–N co-doped $CoFe_2O_4$@rGO@TiO_2 nanoparticles and their superior UV-Vis light photocatalytic activities. **RSC Advances**, Cambridge, v. 9, n. 11, p. 6152-6162, 2019.

144. LIU, D.; HUANG, P.; LIU, Y.; WU, Z.; LI, D.; GUO, J.; WU, T. Cd/In-Codoped TiO_2 nanochips for high-efficiency photocatalytic dye degradation. **Dalton Transactions**, Cambridge, v. 47, n. 17, p. 6177-6183, 2018.

145. CHEN, W. T.; CHAN, A.; SUN-WATERHOUSE, D.; LLORCA, J.; IDRISS, H.; WATERHOUSE, G. I. N. Performance comparison of Ni/TiO_2 and Au/TiO_2 photocatalysts for H_2 production in different alcohol-water mixtures. **Journal of Catalysis**, San Diego, v. 367, p. 27-42, 2018.

146. KONTOLETA, E.; TSOUKALA, A.; ASKES, S. H. C.; ZOETHOUT, E.; OKSENBERG, E.; AGRAWAL, H.; GARNETT, E. C. Using hot electrons and hot holes for simultaneous cocatalyst deposition on plasmonic nanostructures. **ACS Applied Materials & Interfaces**, Washington, v. 12, n. 32, p. 35986-35994, 2020.

147. PAUL, K. K.; GIRI, P. K. Plasmonic metal and semiconductor nanoparticle decorated TiO_2-based photocatalysts for solar light driven photocatalysis. *In*: WANDELT, K. (ed.). **Encyclopedia of interfacial chemistry**. Oxford: Elsevier, 2018. p.786-794.

148. NIE, J.; SCHNEIDER, J.; SIELAND, F.; XIA, S.; BAHNEMANN, D. W. The role of Au loading for visible-light photocatalytic activity of Au-TiO_2 (anatase). **Journal of Photochemistry and Photobiology A:** chemistry, Lausanne, v. 366, p. 111-117, 2018.

149. WANG, H.; YOU, T.; SHI, W.; LI, J.; GUO, L. Au/TiO_2/Au as a plasmonic coupling photocatalyst. **Journal of Physical Chemistry C**, Washington, v. 116, n. 10, p. 6490-6494, 2012.

150. CARETTI, I.; KEULEMANS, M.; VERBRUGGEN, S. W.; LENAERTS, S.; VAN DOORSLAER, S. Light-induced processes in plasmonic gold/TiO_2 photocatalysts studied by electron paramagnetic resonance. **Topics in Catalysis**, New York, v. 58, n. 12, p. 776-782, 2015.

151. LIAO, T.-W.; VERBRUGGEN, S. W.; CLAES, N.; YADAV, A.; GRANDJEAN, D.; BALS, S.; LIEVENS, P. TiO_2 films modified with Au nanoclusters as self-cleaning surfaces under visible light. **Nanomaterials**, Basel, v. 8, n. 1, p. 30, 2018.

152. ASAPU, R.; CLAES, N.; CIOCARLAN, R. G.; MINJAUW, M.; DETAVERNIER, C.; COOL, P.; BALS, S.; VERBRUGGEN, S. W. Electron transfer and near-field mechanisms in plasmonic gold-nanoparticle-modified TiO_2 photocatalytic systems. **ACS Applied Nano Materials**, Washington, v. 2, n. 7, p. 4067-4074, 2019.

153. PEETERS, H.; KEULEMANS, M.; NUYTS, G.; VANMEERT, F.; LI, C.; MINJAUW, M.; DETAVERNIER, C.; BALS, S.; LENAERTS, S.; VERBRUGGEN, S. W. Plasmonic gold-embedded TiO_2 thin films as photocatalytic self-cleaning coatings. **Applied Catalysis B:** environmental, Amsterdam, v. 267, p. 118654, 2020.

154. VELLAICHAMY, B.; PRAKASH, P.; THOMAS, J. Synthesis of AuNPs@RGO nanosheets for sustainable catalysis toward nitrophenols reduction. **Ultrasonics Sonochemistry**, Amsterdam, v. 48, p. 362-369, 2018.

155. YANG, Y.; MA, Z.; XU, L.; WANG, H.; FU, N. Preparation of reduced graphene oxide/meso-TiO_2/AuNPs ternary composites and their visible-light-induced photocatalytic degradation n of methylene blue. **Applied Surface Science**, Amsterdam, v. 369, p. 576-583, 2016.

156. NAIK, G. K.; MISHRA, P. M.; PARIDA, K. Green synthesis of Au/TiO_2 for effective dye degradation in aqueous system. **Chemical Engineering Journal**, Lausanne, v. 229, p. 492-497, 2013.

157. SCARISOREANU, M.; ILIE, A. G.; GONCEARENCO, E.; BANICI, A. M.; MORJAN, I. P.; DUTU, E.; TANASA, E.; FORT, I.; STAN, M.; MIHAILESCU, C. N.; FLEACA, C. Ag, Au and Pt decorated TiO_2 biocompatible nanospheres for UV & vis photocatalytic water treatment. **Applied Surface Science**, Amsterdam, v. 509, p. 145217, 2020.

158. DO, T. C. M. V.; NGUYEN, D. Q.; NGUYEN, K. T.; LE, P. H. TiO_2 and Au-TiO_2 nanomaterials for rapid photocatalytic degradation of antibiotic residues in aquaculture wastewater. **Materials**, Basel, v. 12, n. 15, p. 2434, 2019.

159. MACDONALD, T. J.; AMBROZ, F.; BATMUNKH, M.; LI, Y.; KIM, D.; CONTINI, C.; PODUVAL, R.; LIU, H.; SHAPTER, J. G.; PAPAKONSTANTINOU, I.; PARKIN, I. P. TiO_2 nanofiber photoelectrochemical cells loaded with sub-12 nm AuNPs: size dependent performance evaluation. **Materials Today Energy**, Oxford, v. 9, p. 254-263, 2018.

160. LIM, S. P.; PANDIKUMAR, A.; HUANG, N. M.; LIM, H. N. Facile synthesis of Au@TiO_2 nanocomposite and its application as a photoanode in dye-sensitized solar cells. **RSC Advances**, Cambridge, v. 5, n. 55, p. 44398-44407, 2015.

161. MALTANAVA, H.; POZNYAK, S.; STARYKEVICH, M.; IVANOVSKAYA, M. Electrocatalytic activity of Au nanoparticles onto TiO_2 nanotubular layers in oxygen electroreduction reaction: size and support effects. **Electrochimica Acta**, Oxford, v. 222, p. 1013-1020, 2016.

162. TAKAI, A.; KAMAT, P. V. Capture, store, and discharge. shuttling photogenerated electrons across TiO_2–silver interface. **ACS Nano**, Washington, v. 5, n. 9, p. 7369-7376, 2011.

163. SAHA, S.; VICTORIOUS, A.; SOLEYMANI, L. Modulating the photoelectrochemical response of titanium dioxide (TiO_2) photoelectrodes using gold (Au) nanoparticles excited at different wavelengths. **Electrochimica Acta**, Oxford, v. 380, p. 138154, 2021.

164. ZHONG, N.; CHEN, M.; WANG, Z.; ZHONG, D.; CHANG, H.; ZHAO, M.; XU, Y.; LI, M. A highly sensitive photocatalytic plastic optic-fiber sensor for selective detection of phenol in aqueous solutions. **Sensors and Actuators B:** chemical, Lausanne, v. 285, p. 341-349, 2019.

165. ZAREI, M. Sensitive visible light-driven photoelectrochemical aptasensor for detection of tetracycline using ZrO_2/g-C_3N_4 nanocomposite. **Sensors International**, Beijing, v. 1, p. 100029, 2020.

166. WU, H.; HU, J.; LI, H.; LI, H. A novel photo-electrochemical sensor for determination of hydroquinone based on copper hexacyanoferrate and platinum films modified n-silicon electrode. **Sensors and Actuators B:** chemical, Lausanne, v. 182, p. 802-808, 2013.

167. ZHANG, H.; LI, H.; LI, J.; SUN, H.; ZHOU, L.; WANG, R. A novel photoelectrochemical sensor based on Gr-SiNWS-Si/Pt electrode for sensing of hydroquinone. **International Journal of Electrochemical Science**, Belgrade, v. 14, n. 2, p. 1794-1808, 2019.

168. WANG, P.; HUANG, D.; GUO, W.; DI, J. Photoelectrochemical sensing for hydroquinone based on gold nanoparticle-modified indium tin oxide glass electrode. **Journal of Solid State Electrochemistry**, New York, v. 22, n. 1, p. 123-128, 2018.

169. TURKEVICH, J. Colloidal gold. part I. **Gold Bulletin**, Heidelberg, v. 18, n. 3, p. 86-91, 1985.

170. TURKEVICH, J.; STEVENSON, P. C.; HILLIER, J. A study of the nucleation and growth processes in the synthesis of colloidal gold. **Discussions of the Faraday Society**, Aberdeen, v. 11, n. 0, p. 55-75, 1951.

171. VERBRUGGEN, S. W.; KEULEMANS, M.; GORIS, B.; BLOMMAERTS, N.; BALS, S.; MARTENS, J. A.; LENAERTS, S. Plasmonic 'rainbow' photocatalyst with broadband solar light response for environmental applications. **Applied Catalysis B:** environmental, Amsterdam, v. 188, p. 147-153, 2016.

172. VERBRUGGEN, S. W.; KEULEMANS, M.; VAN WALSEM, J.; TYTGAT, T.; LENAERTS, S.; DENYS, S. CFD modeling of transient adsorption/desorption behavior in a gas phase photocatalytic fiber reactor. **Chemical Engineering Journal**, Lausanne, v. 292, p. 42-50, 2016.

173. PARK, H. H.; PARK, H.; JAMISON, A. C.; LEE, T. R. Colloidal stability evolution and completely reversible aggregation of gold nanoparticles functionalized with rationally designed free radical initiators. **Colloid and Polymer Science**, New York, v. 292, n. 2, p. 411-421, 2014.

174. TANAKA, A.; OGINO, A.; IWAKI, M.; HASHIMOTO, K.; OHNUMA, A.; AMANO, F.; OHTANI, B.; KOMINAMI, H. Gold–titanium(IV) oxide plasmonic photocatalysts prepared by a colloid-photodeposition method: correlation between physical properties and photocatalytic activities. **Langmuir**, Washington, v. 28, n. 36, p. 13105-13111, 2012.

175. KHORE, S. K.; KADAM, S. R.; NAIK, S. D.; KALE, B. B.; SONAWANE, R. S. Solar light active plasmonic Au@TiO_2 nanocomposite with superior photocatalytic performance for H_2 production and pollutant degradation. **New Journal of Chemistry**, Cambridge, v. 42, n. 13, p. 10958-10968, 2018.

176. CHORKENDORFF, I.; NIEMANTSVERDRIET, J. W. Catalyst characterization. *In*: **Concepts of Modern Catalysis and Kinetics**, Weinheim: Wiley-VCH. 2003. p.129-166.

177. LI, Y.; WANG, H.; FENG, Q.; ZHOU, G.; WANG, Z.-S. Gold nanoparticles inlaid TiO_2 photoanodes: a superior candidate for high-efficiency dye-sensitized solar cells. **Energy & Environmental Science**, Cambridge, v. 6, n. 7, p. 2156-2165, 2013.

178. GEINTS, Y. E.; PANINA, E. K.; ZEMLYANOV, A. A. Shape-mediated light absorption by spherical microcapsule with gold-nanoparticles-dope. **Journal of Quantitative Spectroscopy and Radiative Transfer**, Oxford, v. 236, p. 106595, 2019.

179. SUBRAMANIAN, V.; WOLF, E. E.; KAMAT, P. V. Influence of metal/metal ion concentration on the photocatalytic activity of TiO_2−Au composite nanoparticles. **Langmuir**, Washington, v. 19, n. 2, p. 469-474, 2003.

180. TAHIR, M.; TAHIR, B.; AMIN, N. A. S. Gold-nanoparticle-modified TiO_2 nanowires for plasmon-enhanced photocatalytic CO_2 reduction with H_2 under visible light irradiation. **Applied Surface Science**, Amsterdam, v. 356, p. 1289-1299, 2015.

181. TANG, H.; PRASAD, K.; SANJINÈS, R.; SCHMID, P. E.; LÉVY, F. Electrical and optical properties of TiO_2 anatase thin films. **Journal of Applied Physics**, Melville, v. 75, n. 4, p. 2042-2047, 1994.
182. TSUKAMOTO, D.; SHIRAISHI, Y.; SUGANO, Y.; ICHIKAWA, S.; TANAKA, S.; HIRAI, T. Gold nanoparticles located at the interface of anatase/rutile TiO_2 particles as active plasmonic photocatalysts for aerobic oxidation. **Journal of the American Chemical Society**, Washington, v. 134, n. 14, p. 6309-6315, 2012.

183. PRIEBE, J. B.; RADNIK, J.; LENNOX, A. J. J.; POHL, M.-M.; KARNAHL, M.; HOLLMANN, D.; GRABOW, K.; BENTRUP, U.; JUNGE, H.; BELLER, M.; BRÜCKNER, A. Solar hydrogen production by plasmonic Au–TiO_2 catalysts: impact of synthesis protocol and TiO_2 phase on charge transfer efficiency and H_2 evolution rates. **ACS Catalysis**, Washington, v. 5, n. 4, p. 2137-2148, 2015.

184. BOTT, A. W. Electrochemistry of semiconductors. **Current Separations**, Chicago, v. 17, n. 3, p. 87-92, 1998.

185. VELICKÝ, M.; TOTH, P. S. From two-dimensional materials to their heterostructures: an electrochemist's perspective. **Applied Materials Today**, Amsterdam, v. 8, p. 68-103, 2017.

186. LIN, X.; CHEN, H.; HU, Z.; HOU, Y.; DAI, W. Enhanced visible light photocatalysis of TiO_2 by co-modification with Eu and Au nanoparticles. **Solid State Sciences**, Amsterdam, v. 83, p. 181-187, 2018.

187. EUROPEAN COMISSION. **Health effects of artificial light**. Disponível em: https://ec.europa.eu/health/scientific_committees/opinions_layman/artificial-light/en/index.htm. Acesso em: 29 set. 2020.

188. PATAI, S. **The chemistry of the hydroxyl group**. Virgínia: Interscience Publishers, 1971. 1236p.

189. MATHEW, S.; ABRAHAM, T. E.; ZAKARIA, Z. A. Reactivity of phenolic compounds towards free radicals under in vitro conditions. **Journal of Food Science and Technology**, New Delhi, v. 52, n. 9, p. 5790-5798, 2015.

190. EUROPEAN COMMISSION. **Residues:** guidance for generating and reporting methods of analysis in support of pre-registration data requirements for annex ii (part a, section 4) and annex iii (part a, section 5) of directive 91/414. 2000. Disponível em: http://www.biotecnologiebt.it/userfiles/studies/39/files/SANCO_3029_99_rev4.pdf. Acesso em: 29 set. 2020.

191. EUROPEAN COMMISSION. **Guidance document on pesticide residue analytical methods**. 2010. Disponível em: http://www.biotecnologiebt.it/userfiles/studies/39/files/SANCO_825_00_rev8_1_2010.pdf. Acesso em: 29 set. 2020.

192. FANG, X.; LIU, J.; WANG, J.; ZHAO, H.; REN, H.; LI, Z. Dual signal amplification strategy of Au nanopaticles/ZnO nanorods hybridized reduced graphene nanosheet and multienzyme functionalized Au@ZnO composites for ultrasensitive electrochemical detection of tumor biomarker. **Biosensors and Bioelectronics**, Oxford, v. 97, p. 218-225, 2017.

193. THONGMA, S.; TANTISANTISOM, K.; GRISDANURAK, N.; BOONKOOM, T. UV enhanced white-light response based on p-Si/n-ZnO nanorod heterojunction photosensor. **Sensors and Actuators A:** physical, Lausanne, v. 296, p. 324-330, 2019.

194. SHEN, G.-H.; HONG, F. C.-N. Ultraviolet photosensors fabricated with Ag nanowires coated with ZnO nanoparticles. **Thin Solid Films**, Lausanne, v. 570, p. 363-370, 2014.

195. BAK, D.; KIM, J. H. Facile fabrication of pseudo-microspherical ZnO/CdS core-shell photocatalysts for solar hydrogen production by water splitting. **Ceramics International**, Oxford, v. 43, p. 13493-13499, 2017.

196. LEE, K. M.; LAI, C. W.; NGAI, K. S.; JUAN, J. C. Recent developments of zinc oxide based photocatalyst in water treatment technology: a review. **Water Research**, Oxford, v. 88, p. 428-448, 2016.

197. MEENAKSHI, G.; SIVASAMY, A. Synthesis and characterization of zinc oxide nanorods and its photocatalytic activities towards degradation of 2,4-D. **Ecotoxicology and Environmental Safety**, San Diego, v. 135, p. 243-251, 2017.

198. GIRI, P.; CHAKRABARTI, P. Effect of Mg doping in ZnO buffer layer on ZnO thin film devices for electronic applications. **Superlattices and Microstructures**, London, v. 93, p. 248-260, 2016.

199. LEFATSHE, K.; DUBE, P.; SEBUSO, D.; MADHUKU, M.; MUIVA, C. Optical dispersion analysis of template assisted 1D-ZnO nanorods for optoelectronic applications. **Ceramics International**, Oxford, v. 47, n. 6, p. 7407-7415, 2021.

200. WU, G.; SONG, Y.; WAN, J.; ZHANG, C.; YIN, F. Synthesis of ultrafine ZnO nanoparticles supported on nitrogen-doped ordered hierarchically porous carbon for supercapacitor. **Journal of Alloys and Compounds**, Lausanne, v. 806, p. 464-470, 2019.

201. NAEEM, F.; NAEEM, S.; ZHAO, Z.; SHU, G.-Q.; ZHANG, J.; MEI, Y.; HUANG, G. Atomic layer deposition synthesized ZnO nanomembranes: a facile route towards stable supercapacitor electrode for high capacitance. **Journal of Power Sources**, Amsterdam, v. 451, p. 227740, 2020.

202. LIM, J. W.; HWANG, D. K.; LIM, K. Y.; KANG, M.; SHIN, S.-C.; KIM, H.-S.; CHOI, W. K.; SHIM, J. W. ZnO-morphology-dependent effects on the photovoltaic performance for inverted polymer solar cells. **Solar Energy Materials and Solar Cells**, Amsterdam, v. 169, p. 28-32, 2017.

203. KIRTHIKA, B.; SEKAR, S.; SARAVANAN, S.; SHIVASANKARAN, N.; BALAN, A. V.; KALIRAJAN, M. Performance analysis of synthesized ZnO nanoparticles coated photovoltaic cell. **Materials Today:** proceedings, London, v. 21, p. 511-513, 2020.

204. WANG, J.; CHEN, R.; XIANG, L.; KOMARNENI, S. Synthesis, properties and applications of ZnO nanomaterials with oxygen vacancies: a review. **Ceramics International**, Oxford, v. 44, n. 7, p. 7357-7377, 2018.

205. DASH, P.; MANNA, A.; MISHRA, N. C.; VARMA, S. Synthesis and characterization of aligned ZnO nanorods for visible light photocatalysis. **Physica E:** low-dimensional systems and nanostructures, Amsterdam, v. 107, p. 38-46, 2019.

206. GAO, P. X.; MAI, W.; WANG, Z. L. Superelasticity and nanofracture mechanics of ZnO nanohelices. **Nano Letters**, Washington, v. 6, n. 11, p. 2536-2543, 2006.

207. RAJALAKSHMI, M.; SOHILA, S.; RAMYA, S.; DIVAKAR, R.; GHOSH, C.; KALAVATHI, S. Blue green and UV emitting ZnO nanoparticles synthesized through a non-aqueous route. **Optical Materials**, Amsterdam, v. 34, n. 8, p. 1241-1245, 2012.

208. ISLAM, S.; KARIM, M. R.; ZAMAN, M. B. Shape controllable preparation and characterization of submicron lamellar and rod clusters of zinc oxide via conventional and microwave accelerated reaction methods. **Materials Letters**, Amsterdam, v. 92, p. 376-378, 2013.

209. HUANG, N.; ZHU, M. W.; GAO, L. J.; GONG, J.; SUN, C.; JIANG, X. A template-free sol–gel technique for controlled growth of ZnO nanorod arrays. **Applied Surface Science**, Amsterdam, v. 257, n. 14, p. 6026-6033, 2011.

210. ZHANG, D.; PAN, W.; ZHOU, L.; YU, S. Room-temperature benzene sensing with Au-doped ZnO nanorods/exfoliated WSe_2 nanosheets and density functional theory simulations. **ACS Applied Materials & Interfaces**, Washington, v. 13, n. 28, p. 33392-33403, 2021.

211. PATRA, N.; MANIKANDAN, M.; SINGH, V.; PALANI, I. A. Investigations on LSPR effect of Cu/Al nanostructures on ZnO nanorods towards photodetector applications. **Journal of Luminescence**, Amsterdam, v. 238, p. 118331, 2021.

212. LEE, B.-J.; JO, S.-I.; HEO, S.-G.; LEE, W.-Y.; JEONG, G.-H. Structure-controllable synthesis of ZnO nanowires using water vapor in an atmospheric-pressure microwave plasma system. **Current Applied Physics**, Amsterdam, v. 28, p. 52-58, 2021.

213. LUPAN, O.; MAGARIU, N.; KHALEDIALIDUSTI, R.; MISHRA, A. K.; HANSEN, S.; KRÜGER, H.; POSTICA, V.; HEINRICH, H.; VIANA, B.; ONO, L. K.; CUENYA, B. R.; CHOW, L.; ADELUNG, R.; PAUPORTÉ, T. Comparison of thermal annealing versus hydrothermal treatment effects on the detection performances of ZnO nanowires. **ACS Applied Materials & Interfaces**, Washington, v. 13, n. 8, p. 10537-10552, 2021.

214. CHEN, X. X.; CHEN, L.; LI, G.; CAI, L. X.; MIAO, G. Y.; GUO, Z.; MENG, F. L. Selectively enhanced gas-sensing performance to n-butanol based on uniform CdO-decorated porous ZnO nanobelts. **Sensors and Actuators B:** chemical, Lausanne, v. 334, p. 129667, 2021.

215. MUSAT, V.; FORTUNATO, E.; PURICA, M.; MAZILU, M.; REGO, A. M. B. D.; DIACONU, B.; BUSANI, T. Multifunctional zinc oxide nanostructures for a new generation of devices. **Materials Chemistry and Physics**, Lausanne, v. 132, n. 2, p. 339-346, 2012.

216. SINGH, N.; PANDEY, P.; HAQUE, F. Z. Effect of heat and time-period on the growth of ZnO nanorods by sol–gel technique. **Optik - International Journal for Light and Electron Optics**, Munich, v. 123, n. 15, p. 1340-1342, 2012.

217. CHEN, L. J.; CHUANG, Y. J. Hydrothermal synthesis and characterization of hexagonal zinc oxide nanorods with a hexamethylenetetramine (HMTA) template-assisted at a low temperature. **Materials Letters**, Amsterdam, v. 68, p. 460-462, 2012.

218. BAEK, S. H.; NOH, B.Y.; SHIN, J. K.; KIM, J. H. Optical and photovoltaic properties of silicon wire solar cells with controlled ZnO nanorods antireflection coating. **Journal of Materials Science**, New York, v. 47, n. 9, p. 4138-4145, 2012.

219. CHUANG, M.Y.; CHEN, Y. C.; SU, Y. K.; HSIAO, C. H.; HUANG, C. S.; TSAI, J.J.; YU, H. C. Negative differential resistance behavior and memory effect in laterally bridged ZnO nanorods grown by hydrothermal method. **ACS Applied Materials & Interfaces**, Washington, v. 6, n. 8, p. 5432-5438, 2014.

220. GROMYKO, I.; KRUNKS, M.; DEDOVA, T.; KATERSKI, A.; KLAUSON, D.; ACIK, I. O. Surface properties of sprayed and electrodeposited ZnO rod layers. **Applied Surface Science**, Amsterdam, v. 405, p. 521-528, 2017.

221. LIU, T.; CHEN, W.; HUA, Y.; LIU, X. Au/ZnO nanoarchitectures with Au as both supporter and antenna of visible-light. **Applied Surface Science**, Amsterdam, v. 392, p. 616-623, 2017.

222. PATIL, S. B.; SINGH, A. K. Electrodeposited vertically aligned ZnO nanorods thin films on steel substrate for CdS quantum dots sensitized solar cell. **Electrochimica Acta**, Oxford, v. 56, n. 16, p. 5693-5701, 2011.

223. QIU, J.; GUO, M.; WANG, X. Electrodeposition of hierarchical ZnO nanorod-nanosheet structures and their applications in dye-sensitized solar cells. **ACS Applied Materials & Interfaces**, Washington, v. 3, n. 7, p. 2358-2367, 2011.

224. MUCHUWENI, E.; SATHIARAJ, T. S.; NYAKOTYO, H. Effect of annealing on the microstructural, optical and electrical properties of ZnO nanowires by hydrothermal synthesis for transparent electrode fabrication. **Materials Science and Engineering:** b, Amsterdam, v. 227, p. 68-73, 2018.

225. NARAYANAN, G. N.; GANESH, R. S.; KARTHIGEYAN, A. Effect of annealing temperature on structural, optical and electrical properties of hydrothermal assisted zinc oxide nanorods. **Thin Solid Films**, Lausanne, v. 598, p. 39-45, 2016.

226. SHOHANY, B. G.; ZAK, A. K. Doped ZnO nanostructures with selected elements - structural, morphology and optical properties: a review. **Ceramics International**, Oxford, v. 46, n. 5, p. 5507-5520, 2020.

227. MAHADIK, S. A.; PATHAN, H. M.; SALUNKE-GAWALI, S.; BUTCHER, R. J. Aminonaphthoquinones as photosensitizers for mesoporous ZnO based dye-sensitized solar cells. **Journal of Alloys and Compounds**, Lausanne, v. 845, p. 156279, 2020.

228. COSTA, M. B.; LUCAS, F. W. D. S.; MASCARO, L. H. Electrodeposition of Fe-doped Sb_2Se_3 thin films for photoelectrochemical applications and study of the doping effects on their properties. **Journal of Solid State Electrochemistry**, New York, v. 22, n. 5, p. 1557-1562, 2018.

229. SEIPEL, B.; NADARAJAH, A.; WUTZKE, B.; KÖNENKAMP, R. Electrodeposition of ZnO nanorods in the presence of metal ions. **Materials Letters**, Amsterdam, v. 63, n. 9, p. 736-738, 2009.

230. CULLITY, B. D. **Elements of x-ray diffraction**. Reading, Mass: Addison Wesley, 1956. 514p.

231. LANGFORD, J. I.; WILSON, A. J. C. Scherrer after sixty years: a survey and some new results in the determination of crystallite size. **Journal of Applied Crystallography**, Chester, v. 11, n. 2, p. 102-113, 1978.

232. SENER, E.; BAYRAM, O.; HASAR, U. C.; SIMSEK, O. Structural and optical properties of RF sputtered ZnO thin films: annealing effect. **Physica B:** condensed matter, Amsterdam, v. 605, p. 412421, 2021.

233. KUMAR, V.; GUPTA, R.; BANSAL, A. Hydrothermal growth of ZnO nanorods for use in dye-sensitized solar cells. **ACS Applied Nano Materials**, Washington, v. 4, n. 6, p. 6212-6222, 2021.

234. JIANG, L.; LI, J.; HUANG, K.; LI, S.; WANG, Q.; SUN, Z.; MEI, T.; WANG, J.; ZHANG, L.; WANG, N.; WANG, X. Low-temperature and solution-processable zinc oxide transistors for transparent electronics. **ACS Omega**, Washington, v. 2, n. 12, p. 8990-8996, 2017.

235. LI, J.-M.; WANG, Y.-T.; HSU, Y.-J. A more accurate, reliable method to evaluate the photoelectrochemical performance of semiconductor electrode without under/over estimation. **Electrochimica Acta**, Oxford, v. 267, p. 141-149, 2018.

236. SWATHI, S.; BABU, E. S.; YUVAKKUMAR, R.; RAVI, G.; CHINNATHAMBI, A.; ALHARBI, S. A.; VELAUTHAPILLAI, D. Branched and unbranched ZnO nanorods grown via chemical vapor deposition for photoelectrochemical water-splitting applications. **Ceramics International**, Oxford, v. 47, n. 7, Part A, p. 9785-9790, 2021.

237. LITCH, S. Semiconductor electrodes and photoelectrochemistry. *In*: **ENCYCLOPEDIA of electrochemistry**. New Jersey: Wiley-VCH. 2002. v. 6, 597p.

238. EL GHOUL, J.; KRAINI, M.; MIR, L. E. Synthesis of Co-doped ZnO nanoparticles by sol–gel method and its characterization. **Journal of Materials Science:** materials in electronics, Dordrecht, v. 26, n. 4, p. 2555-2562, 2015.

239. TUMMAPUDI, N.; MODEM, S.; JALADI, N. K.; CHOUDARY, G.; KURAPATI, S. R. Structural, morphological, optical and mechanical studies of annealed ZnO nano particles. **Physica B:** condensed matter, Amsterdam, v. 597, p. 412401, 2020.

240. SABEEH, S. H.; JASSAM, R. H. The effect of annealing temperature and Al dopant on characterization of ZnO thin films prepared by sol-gel method. **Results in Physics**, Amsterdam, v. 10, p. 212-216, 2018.

241. FINKLEA, H. O. **Semiconductor electrodes**. Michigan: Elsevier, 1988. 519p.

242. SPINELLE, L.; GERBOLES, M.; KOK, G.; PERSIJN, S.; SAUERWALD, T. Review of portable and low-cost sensors for the ambient air monitoring of benzene and other volatile organic compounds. **Sensors**, Basel, v. 17, n. 7, p. 1520, 2017.

243. KIM, C.; JI, T.; EOM, J. B. Determination of organic compounds in water using ultraviolet LED. **Measurement Science and Technology**, Bristol, v. 29, n. 4, p. 045802, 2018.

244. TAYLOR, A. C.; FONES, G. R.; MILLS, G. A. Trends in the use of passive sampling for monitoring polar pesticides in water. **Trends in Environmental Analytical Chemistry**, Amsterdam, v. 27, p. e00096, 2020.

245. DENG, Z.-H.; LI, N.; JIANG, H.-L.; LIN, J.-M.; ZHAO, R.-S. Pretreatment techniques and analytical methods for phenolic endocrine disrupting chemicals in food and environmental samples. **TrAC Trends in Analytical Chemistry**, Oxford, v. 119, p. 115592, 2019.

246. ELKAMEL, I. B.; HAMDAOUI, N.; MEZNI, A.; AJJEL, R. Enhancement of dielectric properties of Ni and Co doped ZnO due to the oxygen vacancies for UV photosensors application. **Physica E:** low-dimensional systems and nanostructures, Amsterdam, v. 119, p. 114031, 2020.

247. POSTELS, B.; BAKIN, A.; WEHMANN, H. H.; SULEIMAN, M.; WEIMANN, T.; HINZE, P.; WAAG, A. Electrodeposition of ZnO nanorods for device application. **Applied Physics A**, Heidelberg, v. 91, n. 4, p. 595-599, 2008.

248. CAO, S.; YAN, X.; KANG, Z.; LIANG, Q.; LIAO, X.; ZHANG, Y. Band alignment engineering for improved performance and stability of $ZnFe_2O_4$ modified CdS/ZnO nanostructured photoanode for PEC water splitting. **Nano Energy**, Amsterdam, v. 24, p. 25-31, 2016.

249. GHAHRAMANIFARD, F.; ROUHOLLAHI, A.; FAZLOLAHZADEH, O. Electrodeposition of Cu-doped p-type ZnO nanorods: effect of Cu doping on structural, optical and photoelectrocatalytic property of ZnO nanostructure. **Superlattices and Microstructures**, London, v. 114, p. 1-14, 2018.

250. TU, W.; LEI, J.; WANG, P.; JU, H. Photoelectrochemistry of free-base-porphyrin-functionalized zinc oxide nanoparticles and their applications in biosensing. **Chemistry – A European Journal**, Weinheim, v. 17, n. 34, p. 9440-9447, 2011.

251. LV, W.; LIU, J.; HE, Y.; YOU, J. Atomic layer deposition of ZnO thin film on surface modified monolayer MoS_2 with enhanced photoresponse. **Ceramics International**, Oxford, v. 44, n. 18, p. 23310-23314, 2018.

252. JAAFAR, S. N. H.; MINGGU, L. J.; ARIFIN, K.; KASSIM, M. B.; WAN, W. R. D. Natural dyes as TIO_2 sensitizers with membranes for photoelectrochemical water splitting: an overview. **Renewable and Sustainable Energy Reviews**, Oxford, v. 78, p. 698-709, 2017.

253. FORD, W. E. Photochemistry of 3,4,9,10-perylenetetracarboxylic dianhydride dyes: visible absorption and fluorescence spectra and fluorescence quantum yields of the mono(n-octyl)imide derivative in aqueous and non-aqueous solutions. **Journal of Photochemistry**, Lausanne, v. 34, n. 1, p. 43-54, 1986.

254. FERRERE, S.; ZABAN, A.; GREGG, B. A. Dye sensitization of nanocrystalline tin oxide by perylene derivatives. **Journal of Physical Chemistry B**, Washington, v. 101, n. 23, p. 4490-4493, 1997.

255. ROYAL SOCIETY OF CHEMISTRY. **3,4,9,10-perylenetetracarboxylic acid**. ChemSpider. Disponível em: http://www.chemspider.com/Chemical-Structure.59845.html. Acesso em: 20 ago. 2020.

256. WANG, G.-L.; XU, J.-J.; CHEN, H.-Y. Selective detection of trace amount of Cu2+ using semiconductor nanoparticles in photoelectrochemical analysis. **Nanoscale**, Cambridge, v. 2, n. 7, p. 1112-1114, 2010.

257. SOUSA, C. S.; LIMA, K. C. M. S.; BOTELHO, C. N.; PEREIRA, N. M.; FERNANDES, R. N.; SILVA, G. G.; DAMOS, F. S.; LUZ, R. C. S. Photoelectrochemical sensor for determination of naringin at low oxidation potential using a modified FTO electrode with cadmium sulfide and titanium dioxide sensitized with chloroprotoporphyrin IX iron(III). **Journal of Solid State Electrochemistry**, New York, v. 24, n. 8, p. 1715-1726, 2020.

258. GANDHIMATHI, R.; DHEIVAMALAR, S.; DHANASEKARAN, R. Geometry optimization, HOMO and LUMO energy, molecular electrostatic potential, NMR, FT-IR and FT-Raman analyzes on 4-nitrophenol. **The European Physical Journal Applied Physics**, Les Ulis, v. 69, n. 1, p. 10202, 2015.

259. BORTOTI, A. A.; GAVANSKI, A. D. F.; VELAZQUEZ, Y. R.; GALLI, A.; DE CASTRO, E. G. Facile and low cost oxidative conversion of MoS_2 in α-MoO_3: synthesis, characterization and application. **Journal of Solid State Chemistry**, San Diego, v. 252, p. 111-118, 2017.

260. UNITED STATES ENVIRONMENTAL PROTECTION AGENCY (USEPA). **4-nitrophenol**. 2000. Disponível em: https://www.epa.gov/sites/default/files/2016-09/documents/4-nitrophenol.pdf. Acesso em: 09 jun. 2018.

261. ANGELES, L. F.; AGA, D. S. Catching the elusive persistent and mobile organic compounds: novel sample preparation and advanced analytical techniques. **Trends in Environmental Analytical Chemistry**, Amsterdam, v. 25, p. e00078, 2020.

262. MILLER, J. N.; MILLER, J. C. Statistics and chemometrics for analytical chemistry. Harlow: Pearson Education Limited, 2005.

263. MILLER, J. C.; MILLER, J. N. Basic statistical methods for analytical chemistry. part I. statistics of repeated measurements. a review. **Analyst**, Cambridge, v. 113, n. 9, p. 1351-1356, 1988.

264. MILLER, J. N. Basic statistical methods for analytical chemistry. part 2. calibration and regression methods. a review. **Analyst**, Cambridge, v. 116, n. 1, p. 3-14, 1991.

265. RAYMUNDO-PEREIRA, P. A.; CAMPOS, A. M.; MENDONÇA, C. D.; CALEGARO, M. L.; MACHADO, S. A. S.; OLIVEIRA, O. N. Printex 6L carbon nanoballs used in electrochemical sensors for simultaneous detection of emerging pollutants hydroquinone and paracetamol. **Sensors and Actuators B:** chemical, Lausanne, v. 252, p. 165-174, 2017.

266. RAYMUNDO-PEREIRA, P. A.; GOMES, N. O.; MACHADO, S. A. S.; OLIVEIRA, O. N. Simultaneous, ultrasensitive detection of hydroquinone, paracetamol and estradiol for quality control of tap water with a simple electrochemical method. **Journal of Electroanalytical Chemistry**, Lausanne, v. 848, p. 113319, 2019.

267. UNITED STATES ENVIRONMENTAL PROTECTION AGENCY (USEPA). **Method 555 - Determination of chlorinated acids in water by high performance liquid chromatography with a photodiode array ultraviolet detector**. 1992. Disponível em: https://www.epa.gov/nscep. Acesso em: 15 out. 2020.

268. ANŽLOVAR, A.; OREL, Z. C.; KOGEJ, K.; ŽIGON, M. Polyol-mediated synthesis of zinc oxide nanorods and nanocomposites with poly(methyl methacrylate). **Journal of Nanomaterials**, London, v. 2012, p. 760872, 2012.

269. LAMBA, R.; UMAR, A.; MEHTA, S. K.; KANSAL, S. K. Well-crystalline porous ZnO–SnO_2 nanosheets: an effective visible-light driven photocatalyst and highly sensitive smart sensor material. **Talanta**, Amsterdam, v. 131, p. 490-498, 2015.

270. SEMENOV, V. V.; ZOLOTAREVA, N. V.; LADILINA, E. Y.; LERMONTOVA, S. A.; KLAPSHINA, L. G.; GRIGOR’EV, I. S.; LOPATIN, M. A.; KIRILLOV, A. I.; KULIKOVA, T. I.; DOMRACHEV, G. A. Reaction of perylene-3,4,9,10-tetracarboxylic acid dianhydride with 3-aminopropyltriethoxysilane and hexamethyldisilazane. **Russian Journal of General Chemistry**, New York, v. 81, n. 7, p. 1496, 2011.

271. MILLER, D. J.; BIESINGER, M. C.; MCINTYRE, N. S. Interactions of CO_2 and CO at fractional atmosphere pressures with iron and iron oxide surfaces: one possible mechanism for surface contamination? **Surface and Interface Analysis**, Hoboken, v. 33, n. 4, p. 299-305, 2002.

272. ZHANG, Q.; LIU, X.; WANG, H.; LIU, Q.; LIU, Q.; ZHANG, X. Photoelectrochemical thrombin biosensor based on perylene-3,4,9,10-tetracarboxylic acid and Au co-functionalized ZnO nanorods with signal-off quenching effect of Ag@Ag_2S. **Analyst**, Cambridge, v. 146, p. 855-863, 2021.

273. ÖZGÜR, Ü.; ALIVOV, Y. I.; LIU, C.; TEKE, A.; RESHCHIKOV, M. A.; DOĞAN, S.; AVRUTIN, V.; CHO, S. J.; MORKOÇ, H. A comprehensive review of ZnO materials and devices. **Journal of Applied Physics**, Melville, v. 98, n. 4, p. 041301, 2005.

274. NATIONAL LIBRARY OF MEDICINE. **4-Nitrophenol**. PubChem database. Disponível em: https://pubchem.ncbi.nlm.nih.gov/compound/4-Nitrophenol. Acesso em: 25 ago. 2020.

275. DHANAVEL, S.; REVATHY, T. A.; PADMANABAN, A.; NARAYANAN, V.; STEPHEN, A. Highly efficient catalytic reduction and electrochemical sensing of hazardous 4-nitrophenol using chitosan/rGO/palladium nanocomposite. **Journal of Materials Science:** materials in electronics, Dordrecht, v. 29, n. 16, p. 14093-14104, 2018.

276. KUBENDHIRAN, S.; SAKTHIVEL, R.; CHEN, S.-M.; MUTHARANI, B.; CHEN, T.-W. Innovative strategy based on a novel carbon-black−β-cyclodextrin nanocomposite for the simultaneous determination of the anticancer drug flutamide and the environmental pollutant 4-nitrophenol. **Analytical Chemistry**, Washington, v. 90, n. 10, p. 6283-6291, 2018.

277. PANG, X.; BAI, H.; ZHAO, Y.; QU, L.; XU, D.; DING, J.; FAN, W.; SHI, W. Photoelectrochemical detection of 4-nitrophenol by sensitive Ni/Cu_2O photocathode. **Electrochimica Acta**, Oxford, v. 367, p. 137453, 2021.

278. BALASUBRAMANIAN, P.; BALAMURUGAN, T. S. T.; CHEN, S.-M.; CHEN, T. W. Simplistic synthesis of ultrafine $CoMnO_3$ nanosheets: an excellent electrocatalyst for highly sensitive detection of toxic 4-nitrophenol in environmental water samples. **Journal of Hazardous Materials**, Amsterdam, v. 361, p. 123-133, 2019.

279. MEJRI, A.; MARS, A.; ELFIL, H.; HAMZAOUI, A. H. Reduced graphene oxide nanosheets modified with nickel disulfide and curcumin nanoparticles for non-enzymatic electrochemical sensing of methyl parathion and 4-nitrophenol. **Microchimica Acta**, Wien, v. 186, n. 11, p. 704, 2019.

280. MA, X.; WU, Y.; DEVARAMANI, S.; ZHANG, C.; NIU, Q.; SHINGER, M. I.; LI, W.; SHAN, D.; LU, X. Preparation of GO-COOH/AuNPs/ZnAPTPP nanocomposites based on the π–π conjugation: efficient interface for low-potential photoelectrochemical sensing of 4-nitrophenol. **Talanta**, Amsterdam, v. 178, p. 962-969, 2018.

281. TSAI, Y. C.; CHIU, C. C. Amperometric biosensors based on multiwalled carbon nanotube-nafion-tyrosinase nanobiocomposites for the determination of phenolic compounds. **Sensors and Actuators B:** chemical, Lausanne, v. 125, n. 1, p. 10-16, 2007.

282. YANG, J.; LI, D.; FU, J.; HUANG, F.; WEI, Q. TiO_2-CuCNFs based laccase biosensor for enhanced electrocatalysis in hydroquinone detection. **Journal of Electroanalytical Chemistry**, Lausanne, v. 766, p. 16-23, 2016.

283. TASHKHOURIAN, J.; DANESHI, M.; NAMI-ANA, F.; BEHBAHANI, M.; BAGHERI, A. Simultaneous determination of hydroquinone and catechol at gold nanoparticles mesoporous silica modified carbon paste electrode. **Journal of Hazardous Materials**, Amsterdam, v. 318, p. 117-124, 2016.

284. NAZARI, M.; KASHANIAN, S.; MORADIPOUR, P.; MALEKI, N. A novel fabrication of sensor using ZnO-Al_2O_3 ceramic nanofibers to simultaneously detect catechol and hydroquinone. **Journal of Electroanalytical Chemistry**, Lausanne, v. 812, p. 122-131, 2018.

285. DANG, Y.; ZHAI, Y.; YANG, L.; PENG, Z.; CHENG, N.; ZHOU, Y. Selective electrochemical detection of hydroquinone and catechol at a one-step synthesised pine needle-like nano-$CePO_4$ modified carbon paste electrode. **RSC Advances**, Cambridge, v. 6, n. 87, p. 83994-84002, 2016.

286. ZRINSKI, I.; PUNGJUNUN, K.; MARTINEZ, S.; ZAVAŠNIK, J.; STANKOVIĆ, D.; KALCHER, K.; MEHMETI, E. Evaluation of phenolic antioxidant capacity in beverages based on laccase immobilized on screen-printed carbon electrode modified with graphene nanoplatelets and gold nanoparticles. **Microchemical Journal**, Amsterdam, v. 152, p. 104282, 2020.

APPENDIX A – SUPPLEMENTARY INFORMATION (CHAPTER 2)

Figure S2.1 - Schematic FIA setup. (A) Buffer solution; (B) Peristaltic pump; (C) Sample injection; (D) Manual injection valve; (E) Mixer; (F) Waste; (G) Photoelectrochemical flow cell; (H) Potentiostat and (I) Computer.

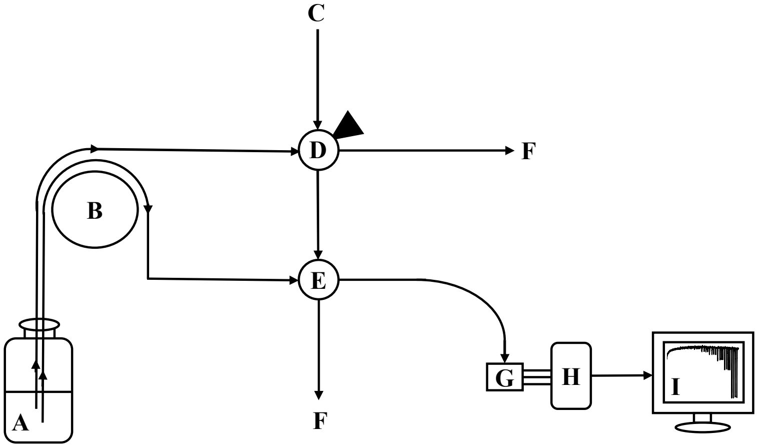

Source: Mendonça *et al.*, 2020.

Figure S2.2 – Chronoamperogram HQ in 10 mM KH_2PO_4 containing 0.1 M KCl (pH 7.0), applied potential -0.14 V vs Ag pseudo reference electrode. Flow rate: 1 mL/min. (a) 0.0125, (b) 0.025, (c) 0.05, (d) 0.15, (e) 0.25, (f) 0.5, (g) 1.0, (h) 2.5, (i) 5.0, (j) 10 and (k) 25 µM, (n = 4).

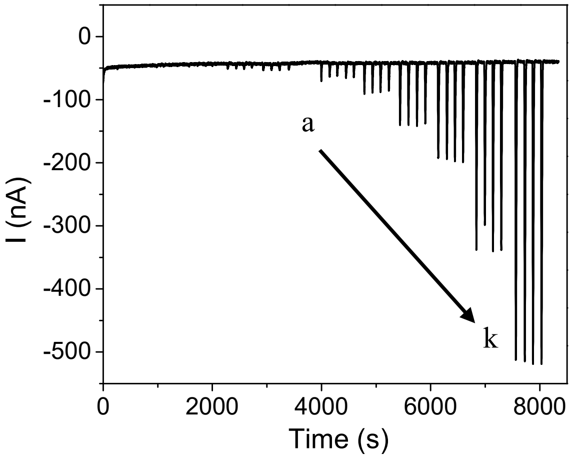

Source: Mendonça *et al.*, 2020.

Figure S2.3 – Chronoamperometric curve for different concentration of HQ in 10 mM KH_2PO_4 containing 0.1 M KCl (pH 7.0), applied potential -0.14 V vs Ag pseudo reference electrode, under UV illumination (black) and in the absence of a light source (red). Flow rate: 1 mL/min. Concentration range: 0.0125 - 25 µM (n = 4).

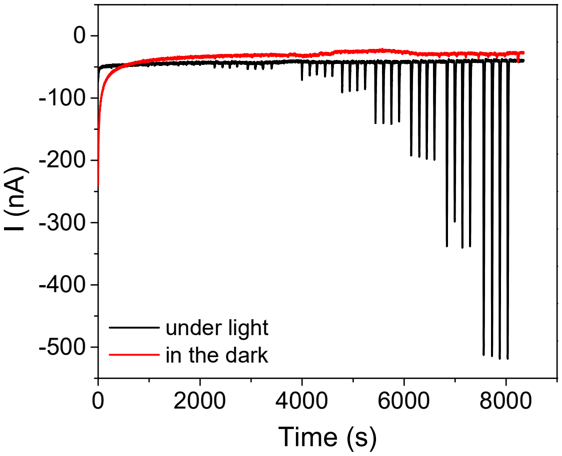

Source: Mendonça *et al*., 2020.

Figure S2.4 – Calibration curve for 0.0125 – 25 µM HQ in 10 mM KH_2PO_4 containing 0.1 M KCl (pH 7.0), applied potential -0.14 V vs Ag pseudo reference electrode and using bare graphite SPE electrode (n = 4). Flow rate: 1 mL/min.

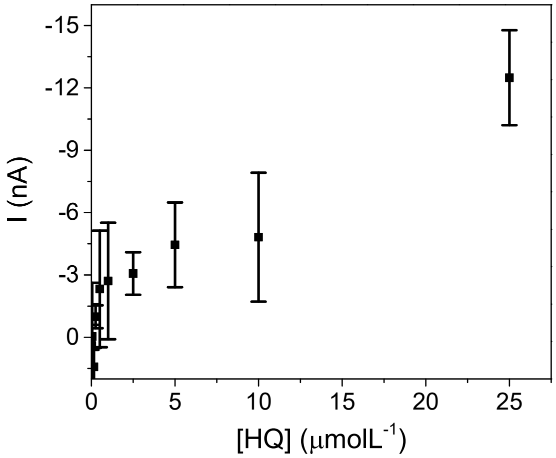

Source: Mendonça *et al*., 2020.

Figure S2.5 – Sensitivity variation during inter-days measurements for one electrode (n = 5) for 0.0125 – 2.5 μM HQ in 10 mM KH_2PO_4 containing 0.1 M KCl (pH 7.0), applied potential -0.14 V vs Ag pseudo reference electrode. Flow rate: 1 mL/min.

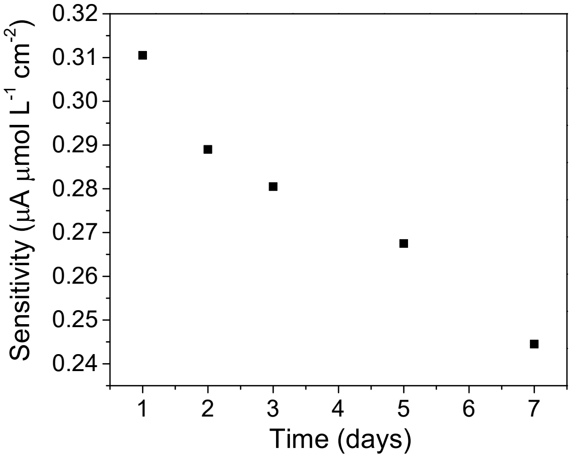

Source: Mendonça *et al.*, 2020.

Figure S2.6 – Flow rate effect on the current response in the presence of 2.5 μM HQ in 10 mM KH_2PO_4 containing 0.1 M KCl (pH 7.0), applied potential -0.14 V vs Ag pseudo reference electrode (n = 4).

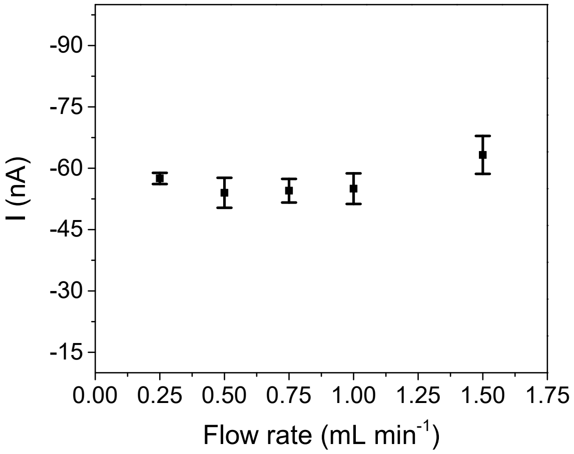

Source: Mendonça *et al.*, 2020.

Figure S2.7 – Changes in background current upon applying different potentials in the presence of 2.5 μM HQ in 10 mM KH_2PO_4 containing 0.1 M KCl (pH 7.0) (n = 4). Flow rate: 1 mL/min.

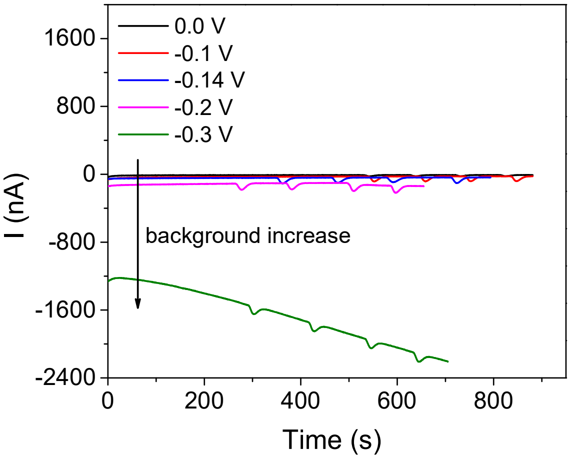

Source: Mendonça *et al*., 2020.

Figure S2.8 – Chronoamperogram 4-AP at SPE|TiO_2 under illumination in 10 mM KH_2PO_4 containing 0.1 M KCl (pH 7.0), applied potential -0.14 V vs Ag pseudo reference electrode (n = 4). Flow rate: 1 mL/min. (a) 0.0125, (b) 0.025, (c) 0.05, (d) 0.15, (e) 0.25, (f) 0.5, (g) 1.0, (h) 2.5, (i) 5.0, (j) 10 and (k) 25 μM.

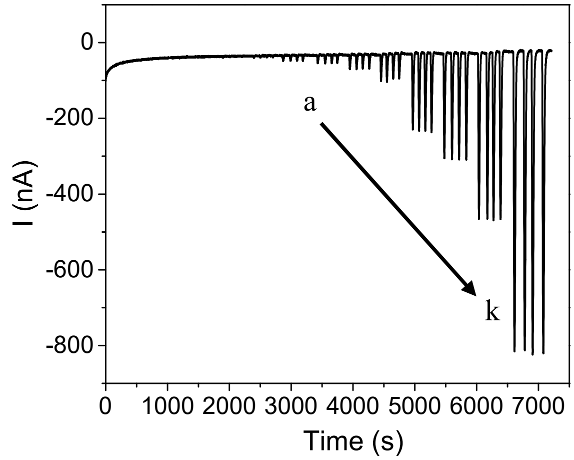

Source: Mendonça *et al*., 2020.

Interference study:

The photoresponse of the proposed photosensor was studied in the presence of bisphenol A (BPA), 2-chlorophenol (2-ClP), 3-nitrophenol (3-NP) and phenol (Ph), as possible interfering compounds. The amperometric responses of 4-AP showed an increase of 4.3%, 5.2%, 4.1% and 4.5%, in presence of BPA, 2-ClP, 3-NP and Ph, respectively (Fig. S2.9). The trend of the reactivity can be explained by the nature of the phenolic structures, the position of the functionalities, and the ability of the substituents to form electron-donor conjugation.[188, 281] Through these results we can conclude there are no significant changes on 4-AP photocurrent by the presence of these possible interfering compounds.

Figure S2.9 – Amperometric responses of solution containing 2.5 µmol L^{-1} of 4-AP and 2.5 µmol L^{-1} of other phenolic compounds: BPA, 2-ClP, 3-NP and Ph, respectively, at SPE|TiO_2 under UV illumination in 10 mM KH_2PO_4 containing 0.1 M KCl (pH 7.0) and applied potential -0.14 V (n = 4).

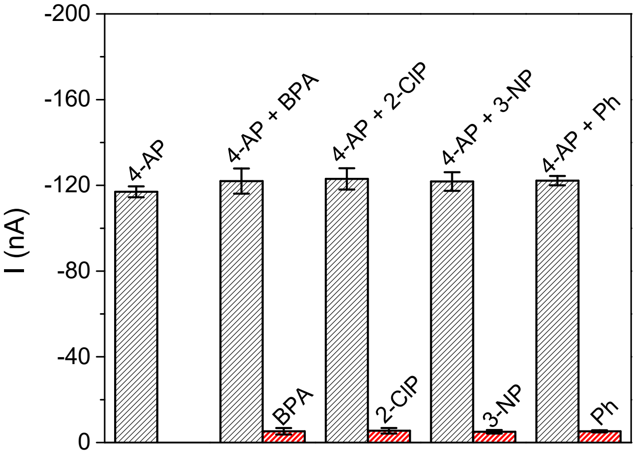

Source: Mendonça *et al*., 2020.

Table S2.1 – Recovery results of HQ and 4-AP quantification in water samples.

Sample	HQ			4-AP		
	Added (µM)	Detected (µM)	Recovered (%)	Added (µM)	Detected (µM)	Recovered (%)
Tap	0.75	0.71	94.4	0.10	0.095	95.4
	1.50	1.63	108.9	0.40	0.37	93.5
	2.00	1.93	96.5	0.75	0.78	103.4
River	0.75	0.68	90.0	0.10	0.098	98.4
	1.50	1.37	91.5	0.40	0.39	96.9
	2.00	2.06	102.8	0.75	0.80	106.9

Source: Mendonça *et al*., 2020.

APPENDIX B – SUPPLEMENTARY INFORMATION (CHAPTER 3)

Figure S3.1 - Photoelectrochemical flow system. (A) buffer solution; (B) peristaltic pump; (C) sample; (D) manual injection valve; (E) mixer; (F) waste; (G) photoelectrochemical flow cell; (H) potentiostat and (I) data collection.

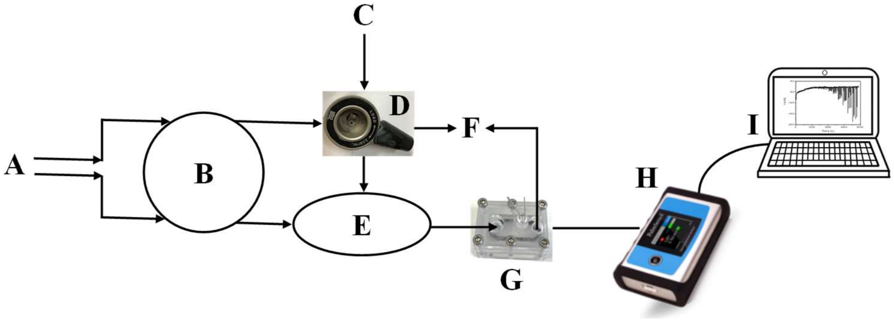

Source: Mendonça *et al*., 2021.

Figure S3.2 - Dependence of the photocurrent response on different loadings of AuNPs on TiO_2 (2.0, 3.0, 3.9 and 4.9 wt.%). The photocurrent was recorded applying a potential of -0.14 V vs Ag quasi-reference electrode (n = 3) and in the presence of 6.0 μM HQ.

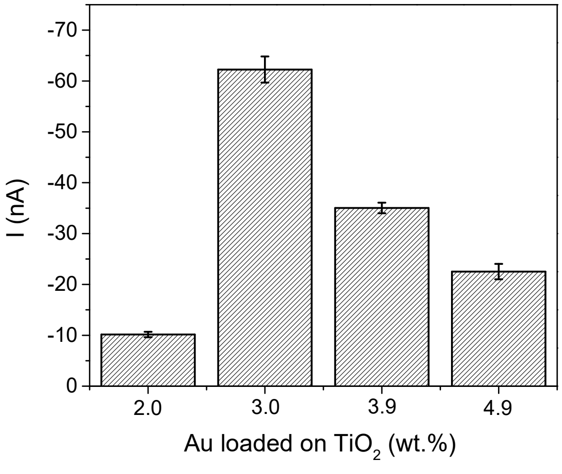

Source: Mendonça *et al*., 2021.

Figure S3.3 - UV-Vis absorbance spectra of colloidal AuNPs solution (1), AuNPs@TiO_2 suspension just after impregnation synthesis (2) and the supernatant of AuNPs@TiO_2 after centrifugation (3).

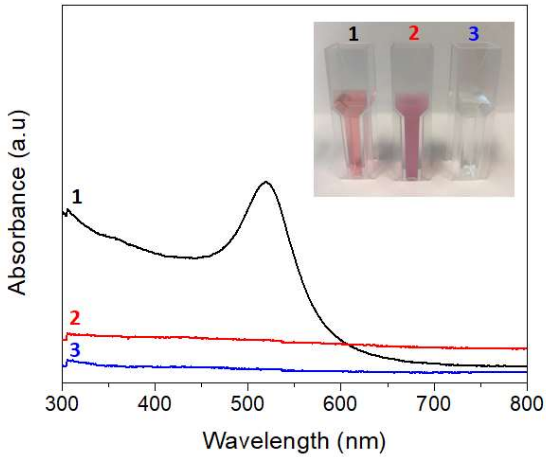

Source: Mendonça *et al.*, 2021.

Figure S3.4 - Calibration curves for 0.0125 – 25 µM HQ at SPE|AuNPs@TiO_2 electrode in 10 mM PBS containing 0.1 M KCl (pH 7.0), applied potential of -0.14 V vs Ag quasi-reference electrode (n = 3). Under green laser illumination (black) and in the absence of a light source (red). Flow rate: 1 mL/min.

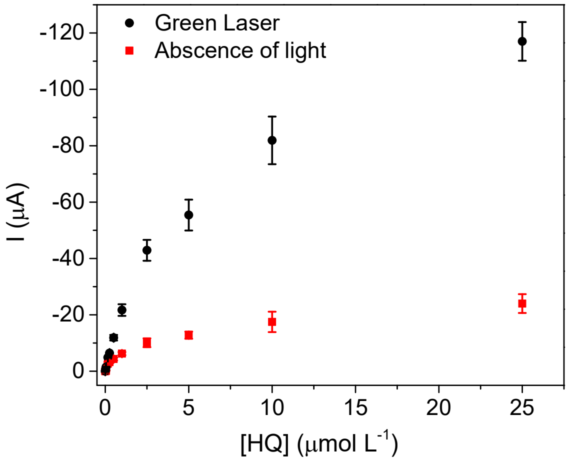

Source: Mendonça *et al.*, 2021.

Figure S3.5 - Calibration curve for 0.0125 – 25 µM HQ at graphite electrode in 10 mM PBS containing 0.1 M KCl (pH 7.0), applied potential of -0.14 V vs Ag quasi-reference electrode under green laser illumination (n = 3). Flow rate: 1 mL/min.

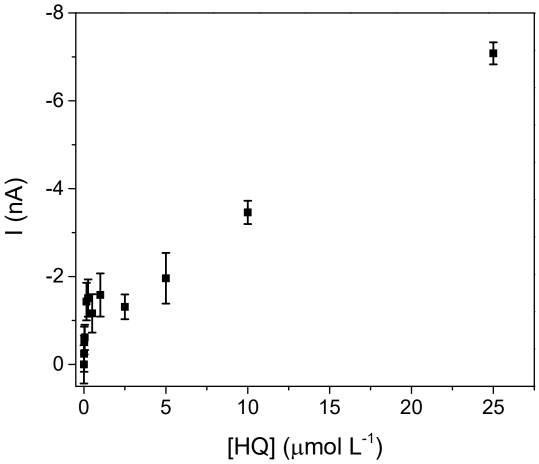

Source: Mendonça *et al*., 2021.

Figure S3.6 - Calibration curves for 0.0125 – 25 µM HQ at SPE|AuNPs@TiO$_2$ electrode in 10 mM PBS containing 0.1 M KCl (pH 7.0), applied potential of -0.14 V vs Ag quasi-reference electrode (n = 3). Under green laser (black) and UV LED (red) illumination. Flow rate: 1 mL/min.

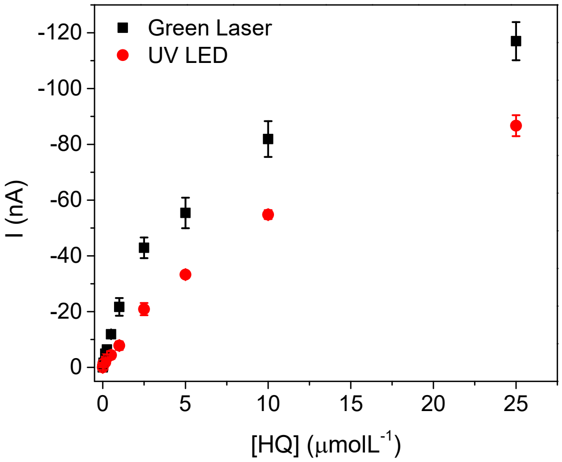

Source: Mendonça *et al*., 2021.

Figure S3.7 - Sensitivity variation during inter-days measurements for one electrode (n = 5) for 0.0125 – 1.0 µM HQ in 10 mM PBS containing 0.1 M KCl (pH 7.0), applied potential -0.14 V vs Ag quasi-reference electrode. Flow rate: 1 mL/min.

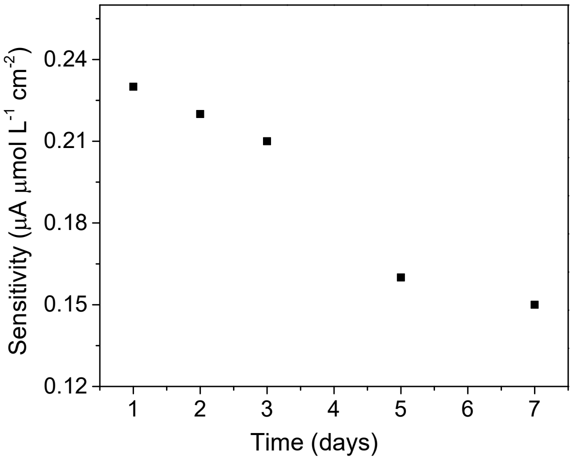

Source: Mendonça *et al.*, 2021.

Figure S3.8 – Flow rate effect on the photocurrent response in the presence of 0.15 µM HQ in 10 mM PBS containing 0.1 M KCl (pH 7.0), applied potential -0.14 V vs Ag quasi-reference electrode (n = 3).

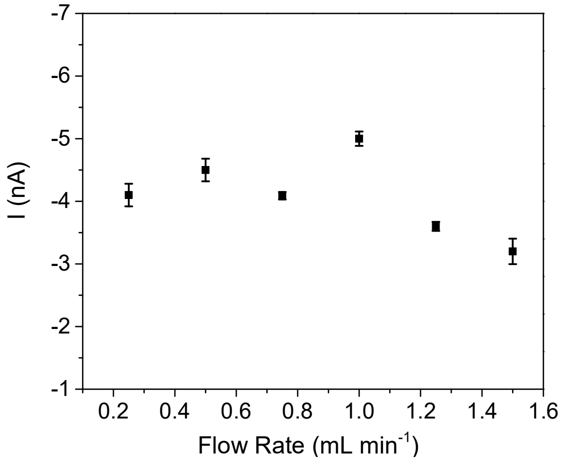

Source: Mendonça *et al.*, 2021.

Figure S3.9 - Amperometric responses of solution containing 1.0 µM of HQ and 10 µM of other phenolic compounds: Ph, 4-NP, BPA, 3-NP, 2-AP, 3-AP, respectively, in 10 mM PBS containing 0.1 M KCl (pH 7.0), using SPE|AuNPs@TiO_2 under green laser illumination and applied potential of -0.14 V vs Ag quasi-reference electrode (n = 3).

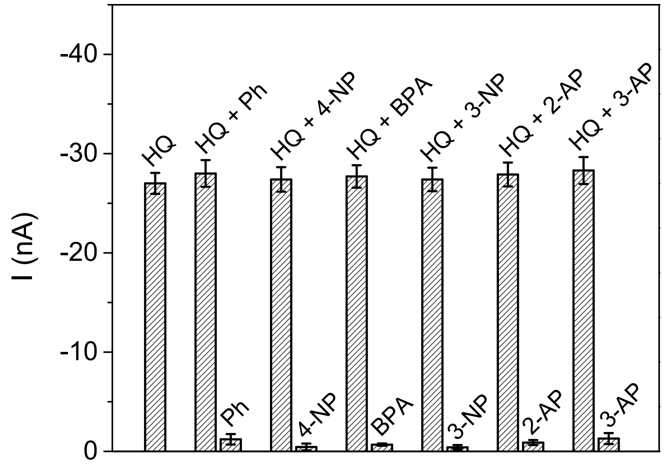

Source: Mendonça *et al.*, 2021.

Table S3.1 – Comparison of the limits of detection of the previously reported electrochemical and photoelectrochemical sensors for hydroquinone.

Working electrode	Method	Limit of detection (nM)	Reference
Nafion-TiO_2/CuCNFs-laccase/GCE	Amperometry	3650	282
AuNPs-MPS/CPE	DPV	920	283
SPE|TiO_2	PEC/FIA	31.2	79
AuNPs/ZnO-Al_2O_3/GO,chit/GCE	DPV	190	284
AuNPs/ITO	PEC	100	168
Pine needle-like nano-$CePO_4$/CPE	DPV	270	285
Gr-SiNWs-Si/Pt	PEC	300	167
LACC/AuNPs/GNPl/SPCE	Amperometry	1500	286
SPE|AuNPs@TiO_2	PEC/FIA	33	This work

Key: CNFs, carbon composite nanofibers; GCE, glassy carbon electrode; AuNPs, gold nanoparticles; MPS, mesoporous silica; CPE, carbon paste electrode; SPE, screen-printed electrode; GO,chit, graphene oxide and chitosan; ITO, indium tin oxide glass; Gr, graphene; SiNWs, silicon nanowires; LACC, laccase; GNPl, graphene nanoplatelets; SPCE, screen-printed carbon electrode; DPV, differential pulse voltammetry; PEC, photoelectrochemical; FIA, flow injection analysis.

Source: Mendonça *et al.*, 2021.

APPENDIX C – SUPPLEMENTARY INFORMATION (CHAPTER 4)

Figure S4.1 - (a) Electrochemical thermostatic cell, (b) quartz window photoelectrochemical cell and (c) its components.

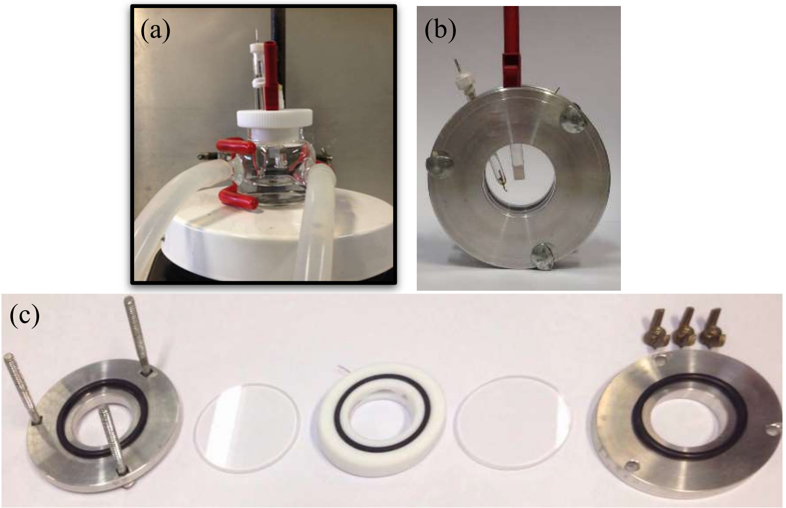

Source: Own authorship.

Figure S4.2 - EDX spectrum for electrodeposited ZnO on FTO substrate, without annealing treatment. Analyzed area: 0.26 mm^2.

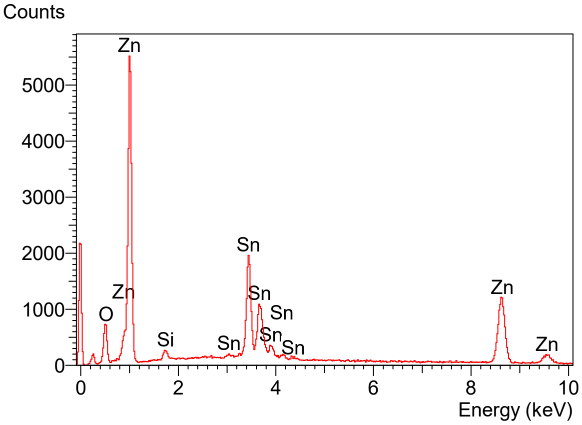

Source: Own authorship.

Table S4.1 - Crystallographic planes and positions of the diffractogram peaks corresponding to the ZnO

Crystallographic plane	**Position (2θ degree)**
(100)	31.66
(002)	34.28
(101)	36.13
(102)	47.39
(110)	56.53
(013)	62.76
(112)	67.81
(021)	69.05

Source: Own authorship.

Table S4.2 - Average photocurrent response and the standard deviation of ZnO nanorod films as grown and annealed at 200 ºC, 300 ºC, 350 ºC, 400 ºC and 500 ºC

Film	**J_M (μA cm^{-2})**	**SD (μA cm^{-2})**
as grown	0.71	0.05
200 ºC	3.35	0.27
300 ºC	53.50	2.89
350 ºC	67.00	2.93
400 ºC	31.11	1.24
500 ºC	7.14	0.20

Note: ZnO nanorod films before and after annealing; J_M: average photocurrent density (n = 3); SD: standard deviation. Source: Own authorship.

APPENDIX D – SUPPLEMENTARY INFORMATION (CHAPTER 5)

Figure S5.1 - Effect of the PTCA concentration on the amperometric response of $ZnO_{350\ °C}$ in the concentration range from 2.3 to 37.4 mM. The measurements were conducted in 10 mM PBS buffer (pH 7.0) using an applied potential of 0.2 V (*vs* Ag/AgCl) and under UV-A illumination (n = 3). Inset: Graph that relates the PTCA concentration with value of photocurrent density obtained and their respective SD.

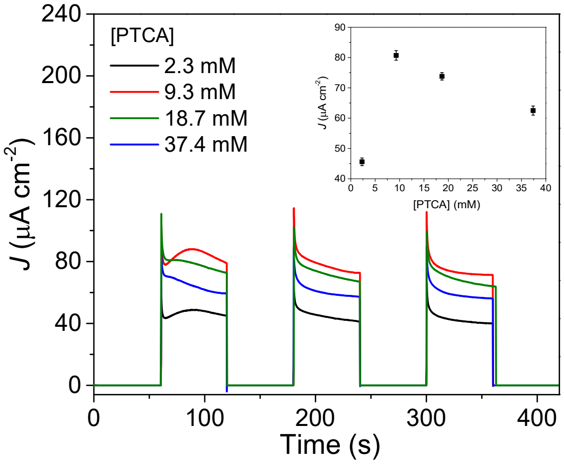

Source: Own authorship.

Figure S5.2 - Chromatographic calibration curves obtained for the detection of 4-NP prepared using ACN, natural water and tap water samples in the concentration range from 0.5 to 50.0 nM. Mobile phase (MP) ACN:phosphoric acid (0.025 M) (60:40, v/v) isocratic mode; flow rate: 1.0 mL/min; λ = 315 nm and injection volume: 20 μL.

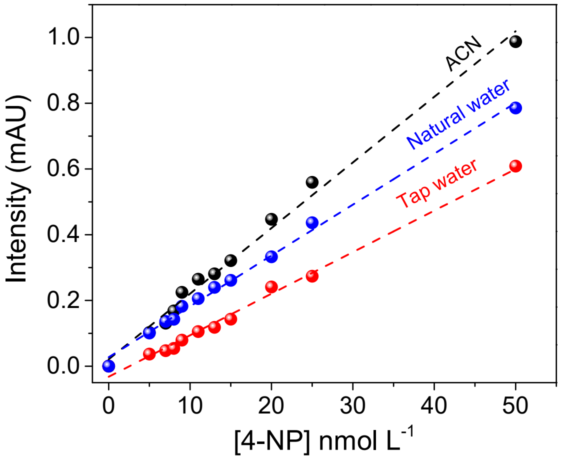

Source: Own authorship.

Table S5.1 – Recovery results for the quantification of 4-NP in water samples using the FTO-ZnO$_{350\,°C}$|PTCA photosensor

Sample	Added (nM)	Detected (nM)	Recovery (%)
Tap water	0.5	0.54	107.6
	4.0	4.20	105.1
	10.0	9.37	93.7
Natural water	1.5	1.61	108.1
	8.0	7.43	92.8
	13.0	12.31	94.6

Source: Own authorship.

ANNEX I

Electrochemistry Communications 117 (2020) 106767

Contents lists available at ScienceDirect

Electrochemistry Communications

journal homepage: www.elsevier.com/locate/elecom

Integration of a photoelectrochemical cell in a flow system for quantification of 4-aminophenol with titanium dioxide

Camila D. Mendonça[a,b,1], Vanoushe Rahemi[a,1], Jonas Hereijgers[c], Tom Breugelmans[c,d], Sergio A.S. Machado[b], Karolien De Wael[a,e,*]

[a] *AXES Research Group, University of Antwerp, Groenenborgerlaan 171, 2020 Antwerp, Belgium*
[b] *Institute of Chemistry of São Carlos, University of São Paulo, IQSC – USP, Av. Trabalhador São-carlense 400, São Carlos, SP, Brazil*
[c] *ELCAT Research Group, University of Antwerp, Universiteitsplein 1, 2610 Wilrijk, Belgium*
[d] *Separation & Conversion Technologies, VITO, Boeretang 200, 2400 Mol, Belgium*
[e] *NANOlab Center of Excellence, University of Antwerp, Groenenborgerlaan 171, 2020 Antwerp, Belgium*

ARTICLE INFO

Keywords:
Flow injection analysis
Reactive oxygen species
Titanium dioxide
Photoelectrochemical detection
UV illumination
4-Aminophenol

ABSTRACT

The photoelectrochemical quantification of phenolic compounds such as hydroquinone (HQ) and 4-aminophenol (4-AP) is accomplished by integrating a photoelectrochemical cell into a flow injection analysis (FIA) setup. It is a well-known fact that during the electroanalysis of phenolic compounds, the electrode surface is susceptible to poisoning. However, electrode fouling can be reduced significantly by using the FIA system with periodic washing of the electrode. Reactive oxygen species (ROS), which are generated on the surface of TiO_2 under UV light, can oxidize phenolic compounds such as 4-AP. The oxidized form of 4-AP is reduced back at the electrode surface, generating a measurable signal proportional to its concentration. The factors influencing the performance of the sensor, such as flow rate, applied potential for back reduction and pH, are investigated in detail. In the concentration range 0.0125–1.0 μM, a linear correlation between the photocurrent and the concentration of 4-AP was observed with a sensitivity of 0.6 A M^{-1} cm^{-2} and a limit of detection of 18 nM. A straightforward analytical methodology for the on-site, highly sensitive and low-cost quantification of phenolic compounds is presented, based on the use of TiO_2 in a photoelectrochemical flow cell.

1. Introduction

Flow injection analysis (FIA) is an approach for the automated chemical analysis of organic contaminants [1–5]. This approach ensures high mass transfer and provides clean electrode surfaces after periodic washing steps [6], improving the robustness of the method and allowing rapid analysis [7]. In order to enhance the sensitivity of detection, FIA has been combined with electrodes modified with carbon nanotubes [6], molecularly imprinted polymers [8], graphene [9] and quantum dots [10]. This combination produces valuable systems with sensitivity and selectivity competitive to their chromatographic alternatives with the advantages of being portable and easy to use [11,12], enabling "in situ" and real-time analysis.

Another recent approach that has attracted considerable attention for the detection of organic compounds is photoelectrochemical analysis [13–17]. Among different photoactive materials, titanium dioxide (TiO_2) is considered one of the most effective photocatalysts due to its high photoactivity and stability. It has been extensively used in water and wastewater treatment studies because it is chemically and biologically inert, cost-effective, non-toxic, and can promote the oxidation of organic compounds under UV illumination [18–21]. The band gap of TiO_2 is ~ 3.2 eV, depending on its crystalline form (anatase, rutile or brookite). Therefore, light with energy values greater than its band gap is required to excite electrons to the conduction band (CB) with the generation of holes in the valence band (VB) [18]. The photogenerated electron-hole pairs may react with adsorbed species available on the surface of TiO_2, such as OH^- and H_2O, producing reactive oxygen species (ROS) which may further oxidize phenolic compounds, allowing their quantification [22].

Inspired by the advantages of FIA and TiO_2-based photoelectrochemical detection, we have designed an analytical photosensing device for the amperometric quantification of 4-AP, an environmentally hazardous and toxic molecule. Commonly, 4-AP is used in the manufacture of pharmaceutical and cosmetic products; furthermore, it is

---

* Corresponding author.
E-mail address: karolien.dewael@uantwerpen.be (K. De Wael).

[1] Camila D. Mendonça and Vanoushe Rahemi contributed equally to this work.

https://doi.org/10.1016/j.elecom.2020.106767
Received 16 April 2020; Received in revised form 7 June 2020; Accepted 10 June 2020
Available online 13 June 2020

ANNEX II

Electrochimica Acta 389 (2021) 138734

Contents lists available at ScienceDirect

Electrochimica Acta

journal homepage: www.elsevier.com/locate/electacta

Surface plasmon resonance-induced visible light photocatalytic TiO_2 modified with AuNPs for the quantification of hydroquinone

Camila D. Mendonça[a,b], Shahid U. Khan[a,c,d], Vanoushe Rahemi[a], Sammy W. Verbruggen[c,d], Sergio A.S. Machado[b], Karolien De Wael[a,d,*]

[a] *AXES research group, University of Antwerp, Groenenborgerlaan 171, 2020 Antwerp, Belgium*
[b] *São Carlos Institute of Chemistry, University of São Paulo, IQSC – USP, Av. Trabalhador São-carlense 400, São Carlos SP, Brazil*
[c] *Sustainable Energy, Air & Water Technology (DuEL), University of Antwerp, Groenenborgerlaan 171, 2020 Antwerp, Belgium*
[d] *NANOlab Center of Excellence, University of Antwerp, Groenenborgerlaan 171, 2020 Antwerp, Belgium*

ARTICLE INFO

Article history:
Received 9 March 2021
Revised 20 May 2021
Accepted 31 May 2021
Available online 4 June 2021

Keywords:
Gold nanoparticles
Titanium dioxide
Surface plasmon resonance
Photoelectrochemical detection
Flow injection analysis
Reactive oxygen species
Hydroquinone

ABSTRACT

The impregnation of size-controlled gold nanoparticles (AuNPs) on an anatase TiO_2 structure (AuNPs@TiO_2) was studied for the photoelectrochemical detection of hydroquinone (HQ) under visible light illumination integrated into a flow injection analysis (FIA) setup. The crystalline form of TiO_2 was preserved during synthesis and the homogeneous distribution of AuNPs over the TiO_2 structure was confirmed. Its photoelectrocatalytic activity was improved due to the presence of AuNPs, preventing charge recombination in TiO_2 and improving its light absorption ability by the surface plasmon resonance effect (SPR). The FIA system was used in order to significantly reduce the electrode fouling during electroanalysis through periodic washing steps of the electrode surface. During the amperometric detection process, reactive oxygen species (ROS), generated by visible light illumination of AuNPs@TiO_2, participate in the oxidation process of HQ. The reduction of the oxidized form of HQ, *i.e.* benzoquinone (BQ) occurs by applying a negative potential and the measurable amperometric response will be proportional to the initial HQ concentration. The influencing parameters on the response of the amperometric photocurrent such as applied potential, flow rate and pH were investigated. The linear correlation between the amperometric response and the concentration of HQ was recorded (range 0.0125 – 1.0 µM) with a limit of detection (LOD) of 33.8 nM and sensitivity of 0.22 A M^{-1} cm^{-2}. In this study, we illustrated for the first time that the impregnation of AuNPs in TiO_2 allows the sensitive detection of phenolic substances under green laser illumination by using a photoelectrochemical flow system.

1. Introduction

Semiconductors-based photocatalysts have been widely used over the years in the fields of environmental applications and energy production [1–3]. Among a diversity of photocatalysts, titanium dioxide (TiO_2) is one of the best known and applied in several studies, such as in water and wastewater treatment, mainly due to its stability and cost effectiveness [1,4,5]. Furthermore, the numerous advantages of TiO_2 make it an attractive material for photocatalytic studies. Indeed, the material is biologically and chemically inert, non-toxic and commercially available, and it has excellent optical properties and efficient photocatalytic activity, being able to easily promote the oxidation of organic molecules [1,6–9]. However, the band gap of TiO_2 is approximately 3.2 eV (anatase, rutile or brookite crystalline form), allowing it to only absorb about 3 to 5% of the solar spectrum radiation on earth [10]. Therefore, in order to promote electrons from the valency band of TiO_2 to its conduction band and, consequently, generating holes in the valence band, it is required to employ a light source with an energy potential superior to TiO_2 band gap (*i.e.* $\lambda \leq 387$ nm) [6].

Photocatalyst-based photoelectrochemical platforms are promising sensing devices, because of their low cost, easy-to-use, portability potential, with low background signal, high sensitivity and stability [9,11]. One of the most striking advantages of the photoelectrochemical analysis technique is related to the separation of excitation and detection sources, leading to a reduced background signal with a potentially greater sensitivity in comparison to the traditional electrochemical techniques [12–14]. However, the semiconductors-based photocatalysts, such as TiO_2, are affected by the high electrons/holes recombination rate, which may result in a low photocatalytic yield [15,16]. Concerning about this, in an attempt to build an efficient, stable and powerful photocatalytic material, modifying the semiconductor-based pho-

---

[*] Corresponding author.
E-mail address: karolien.dewael@uantwerpen.be (K. De Wael).

https://doi.org/10.1016/j.electacta.2021.138734

SCIENTIFIC CONTRIBUTIONS DURING PhD

1. Photoelectrochemical sensing of 4-NP based on nanostructured ZnO sensitized by carboxylated perylene. *In preparation*.

2. Study of the annealing effect on the crystallinity of ZnO nanorods synthesized by a straightforward electrodeposition method. *Submitted*.

3. GOMES, N. O.; **MENDONÇA, C. D.**; MACHADO, S. A. S.; OLIVEIRA JR, O. N.; RAYMUNDO-PEREIRA, P. A. Flexible and integrated dual carbon sensor for multiplexed detection of nonylphenol and paroxetine in tap water samples. *Microchimica Acta*, 188: 359, 2021.

4. **MENDONÇA, C. D.**; KHAN, S. U.; RAHEMI, V.; VERBRUGGEN, S. W.; MACHADO, S. A. S.; DE WAEL, K. Surface plasmon resonance-induced visible light photocatalytic TiO_2 modified with AuNPs for the quantification of hydroquinone (in press). *Electrochimica Acta*, 138734, 2021.

5. MORO, G.; BARICH, H.; DRIESEN, K.; MONTIEL, N. F.; NEVEN, L.; **MENDONÇA, C. D.**; SHANMUGAN, S. T.; DAEMS, E.; DE WAEL, K. Unlocking the full power of electrochemical fingerprinting for on-site sensing applications. *Analytical and Bioanalytical Chemistry*, v. 412, p. 5955-5968, 2020.

6. **MENDONÇA, C. D.**; RAHEMI, V.; HEREIJGERS, J.; BREUGELMANS, T.; MACHADO, S. A. S.; DE WAEL, K. Integration of a photoelectrochemical cell in a flow system for quantification of 4-aminophenol with titanium dioxide. *Electrochemistry Communications*, v. 106767, p. 106767, 2020.

7. CAMPOS, A. M.; RAYMUNDO-PEREIRA, P. A.; **MENDONÇA, C. D.**; CALEGARO, M. L.; MACHADO, S. A. S.; OLIVEIRA JR, O. N. Size control of carbon spherical shells for sensitive detection of paracetamol in sweat, saliva and urine. *ACS Applied Nano Materials*, v. 1, p. 654-661, 2018.

8. **MENDONÇA, C. D.**; PRADO, T. M.; CINCOTTO, F. H.; VERBINNEN, R. T.; MACHADO, S. A. S. Methylparaben quantification via electrochemical sensor based on reduced graphene oxide decorated with ruthenium nanoparticles. *Sensors and Actuators B-Chemical*, v. 251, p. 739-745, 2017.

9. RAYMUNDO-PEREIRA, P. A.; CAMPOS, A. M.; **MENDONÇA, C. D.**; CALEGARO, M. L.; MACHADO, S. A. S.; OLIVEIRA JR, O. N. Printex 6L carbon nanoballs used in electrochemical sensors for simultaneous detection of emerging pollutants hydroquinone and paracetamol. *Sensors and Actuators B-Chemical*, v. 252, p. 165-174, 2017.

10. RAYMUNDO-PEREIRA, P. A.; CAMPOS, A. M.; VICENTINI, F. C.; JANEGITZ, B. C.; **MENDONÇA, C. D.**; FURINI, L. N.; BOAS, N. V.; CALEGARO, M. L.; CONSTANTINO, C. J. L.; MACHADO, S. A. S.; OLIVEIRA JR, O. N. Sensitive detection of estriol hormone in creek water using a sensor platform based on carbon black and silver nanoparticles. *Talanta*, v. 174, p. 652-659, 2017.